1-1-2007

Effects of temperature, strain rate and silicon content on dynamic strain ageing of modified chromium-molybdenum steel

Pankaj Kumar
University of Nevada, Las Vegas

EFFECTS OF TEMPERATURE, STRAIN RATE AND Si CONTENT ON DYNAMIC STRAIN AGEING OF MODIFIED 9Cr-1Mo STEEL

by

Pankaj Kumar

Bachelor of Technology in Metallurgy and Materials Engineering
National Institute of Foundry and Forge Technology, Ranchi, India
May 2002

Master of Technology in Materials and Metallurgical Engineering
Indian Institute of Technology Kanpur, India
July 2004

A dissertation submitted in partial fulfillment
of the requirements for the

Doctor of Philosophy Degree in Mechanical Engineering
Department of Mechanical Engineering
Howard R. Hughes College of Engineering

Graduate College
University of Nevada, Las Vegas
December 2007

UNLV
UNIVERSITY OF NEVADA LAS VEGAS

Dissertation Approval

The Graduate College
University of Nevada, Las Vegas

November 13, 20 07

The Dissertation prepared by

Pankaj Kumar

Entitled

Effects of Temperature, Strain Rate and Si Content on Dynamic Strain Ageing of Modified 9Cr-1Mo Steel

is approved in partial fulfillment of the requirements for the degree of

Doctor of Philosophy in Mechanical Engineering

Cigdem K. Roy
Examination Committee Chair

Dean of the Graduate College

Examination Committee Member

Examination Committee Member

Examination Committee Member

Graduate College Faculty Representative

ABSTRACT

Effects of Temperature, Strain Rate and Si Content on Dynamic Strain Ageing of Modified 9Cr-1Mo Steel

by

Pankaj Kumar

Dr. Ajit K. Roy, Examination Committee chair
Professor of Mechanical Engineering
University of Nevada, Las Vegas

Martensitic T91 grade steels exhibited a susceptibility to dynamic strain ageing (DSA) by virtue of gradually reduced failure strain (e_f) and formation of serrations within a susceptible temperature range, irrespective of the silicon (Si) content. Since DSA is a thermally-activated process involving diffusion of solute elements, the effects of temperature and strain rate have been investigated. The activation energy associated with the diffusion process was gradually enhanced with increasing Si content at comparable temperatures. A maximum dislocation density was determined at 400°C at which lowest e_f was observed in the engineering stress versus engineering strain diagram. The resistance to plastic deformation in terms of work-hardening index was gradually enhanced with an increase in temperature up to 400°C, independent of the Si content. The presence of higher Si content in the T91 grade steels resulted in reduced impact resistance and fracture toughness. Steel containing 2.0 weight percent Si exhibited predominantly ductile failures under tensile loading at all tested temperatures. However, the other materials showed a combination of brittle and ductile failures.

TABLE OF CONTENTS

LIST OF TABLES

LIST OF FIGURES

ACKNOWLEDGEMENTS

This work would not have been possible without the never-ending, untiring support of Professor Ajit K. Roy. During my last three years of stay at UNLV, Dr. Roy's indefatigable enthusiasm and passion for research have been a great inspiration to me. His unswerving support and guidance throughout the course of this research is gratefully acknowledged.

I would also like to thank my committee members, Dr. Anthony Hechanova, Dr. Daniel Cook, Dr. Brendan O'Toole and Dr. Edward Neumann, for their direct and indirect contribution throughout this investigation. Special thanks goes to my friends Debajyoti, Joydeep, Lalit, Ratnabali, Saswati and all my colleagues at MPL, for their consistent help throughout my doctorate.

Without the long-distance love of my family – my father Mr. Arun Kumar, my mother Mrs. Neelam Devi, my wife Jyoti, brother-in-law Santosh, and sister Kanchan, I would not have been able to attend or complete Grad School. I offer them this Dissertation in return for their sacrifices, and for sustaining me through the peaks and troughs of this process.

Finally I would like to acknowledge the financial support of the United States Department of Energy (USDOE).

CHAPTER 1

INTRODUCTION

The environmental concern over nuclear waste management presents a formidable barrier to increased use of nuclear energy for various applications in the United States at a time when there is global climatic change and an increased need for energy independence. At present, the waste that results from nuclear-power reactors will take more than 10,000 years to decay to the natural radioactive levels of uranium ore. The nuclear reactors currently operating in the United States are expected to produce more than 90,000 metric tons of nuclear waste, thereby exceeding the current statutory disposal limit at the proposed Yucca Mountain repository. Thus, considering a modest growth in the generation of electricity using the nuclear heat, the nation needs to construct and license additional repositories in the near future [1]. Hence, alternate avenues must actively be pursued for disposal of spent nuclear fuels (SNF) resulting from the next generation nuclear reactors in a safe but economic manner.

One way of enhancing the efficiency of the proposed geologic repository is to reduce the radioactivity of SNF resulting from ongoing utilization of the existing nuclear power plants [2]. This approach, known as transmutation, has successfully been implemented in many countries in Europe. More recently, the United States Department of Energy (USDOE) has taken a bold step to utilize the concept of transmutation so that larger volume of less radioactive SNF could be accommodated inside the proposed

repository [3] for shorter durations. The process of transmutation involves transformation of highly radioactive SNF to species with shorter half-lives by changes in the nucleus of radioactive elements resulting from natural radioactive decay, nuclear fission, neutron capture and other related processes.

The transmutation process, envisioned by USDOE, will enable generation and subsequent separation of minor actinides and fission products by projecting proton-generated neutrons onto SNF at a very high speed. The principle of transmutation is illustrated in Figure 1. These neutrons will be generated by a process known as spallation, which involves bombarding of a target material with protons from an accelerator. Target materials, such as tungsten and molten lead-bismuth-eutectic (LBE), have been extensively used in many European countries. Therefore, at the onset of the present investigation, molten LBE was proposed by Los Alamos National Laboratory to be the primary target material in transmutation. During the spallation process involving molten LBE, significantly high temperatures ranging from 420-550 °C may be developed [4]. Thus, molten LBE can also act as a coolant during this process. Obviously, the molten LBE has to be contained inside a vessel made of a suitable structural material. Thus, the containment material has to sustain such elevated temperatures in the presence of molten LBE, which may also cause environment-assisted degradations of this material.

Even though the molten LBE was considered by USDOE to be the primary target material for transmutation of SNF, corrosion studies involving candidate structural materials could not be performed at the University of Nevada Las Vegas (UNLV) in the presence of molten LBE due to the lack of proper infrastructures. Therefore, the characterization of different types of environmental degradations of these alloys was

performed at the Materials Performance Laboratory (MPL) of UNLV in an acidic solution at ambient and elevated temperatures. The results of corrosion studies in this environment have already been presented in a recent dissertation [5], involving iron-chromium-molybdenum (Fe-Cr-Mo) alloys containing different levels of silicon (Si). The present investigation is primarily focused on the evaluation of the tensile properties of identical structural materials at temperatures ranging from ambient to 550°C, and developing a basic understanding of plastic deformation as functions of different metallurgical and experimental variables.

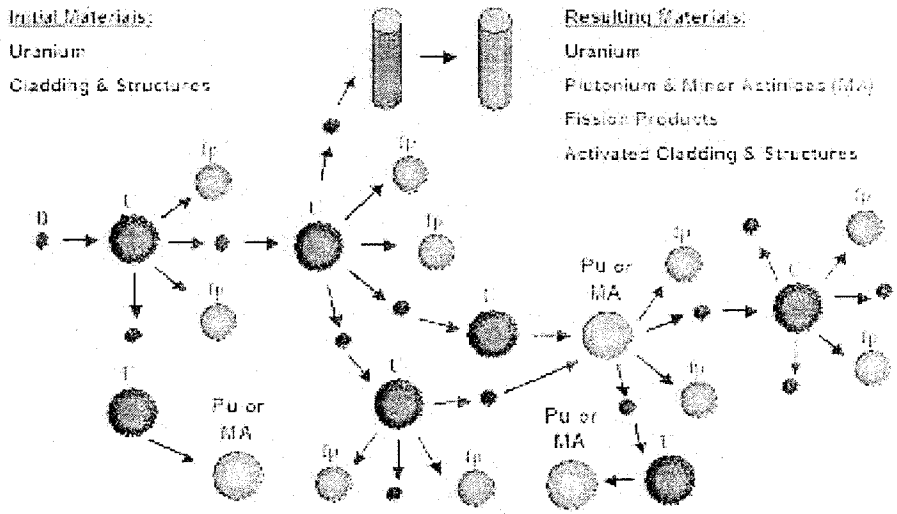

Figure 1-1. Seperation of Fission Products and Minor Actinides

Martensitic steels containing Cr and Mo, such as 9Cr-1Mo steels have long been used in many industrial applications, requiring superior corrosion resistance while maintaining adequate structural strength [6-9]. 9Cr-1Mo steels were later modified by additions of niobium (Nb) and vanadium (V) [10] to enhance their tensile strength at elevated

temperatures in the presence a of molten metal for specific applications such as liquid-metal-fast-breeder-reactors. These materials, also known as T91 grade steels, have proved their usefulness in many nuclear applications due to their excellent neutron absorption capability. Simultaneously, the presence of high Si content in Fe-Cr-Mo steels has already exhibited enhanced corrosion resistance in the presence of acidic solutions in several investigations [11-13], recently performed at UNLV [5]. Based on these observations, it was thought that T91 grade steels having different levels of Si content could provide the desired combination of excellent corrosion resistance and superior tensile strength for their efficient utilization in the transmutation process. In view of this rationale, T91 grade steels with variable Si content were considered to be the suitable candidate materials for evaluation of both corrosion resistance and tensile properties under conditions relevant to the transmutation process.

T91 grade steels having high Cr levels have also been used in many nuclear applications such as fusion reactors and fast breeder reactors due to their high stability in physical and mechanical properties under irradiation and thermal ageing. The presence of high Cr content in these alloys can significantly enhance their structural strength at elevated temperatures, and can result in lower thermal stresses and corrosion rates even in the presence of a liquid metal. These alloys are commonly used in quenched and tempered conditions, which can lead to the formation of fine-grained tempered martensitic microstructures that may provide a combination of excellent tensile strength and ductility. In general, steels containing high Cr levels can provide excellent hardenability, which is beneficial for operations in the temperature range of 400-600°C

that is also similar to the operating temperature range associated with the proposed transmutation process involving molten LBE as the target material.

The presence of Si in Fe-Cr-Mo steels is known to provide superior corrosion resistance due to the formation of protective silicon dioxide (SiO_2) films on their surface [11]. The beneficial effects of Si ranging from 0.5 to 1.5 weight percent (wt %) on both the room-temperature tensile properties, and the resistance to environmental degradations have been demonstrated in a recent investigation conducted by a researcher from MPL [5]. However, no efforts have yet been made to study the role of Si content on the tensile deformation of T91 grade steels at temperatures relevant to the transmutation process. This investigation, therefore, is aimed at evaluating the role of Si content, within a comparable composition range, on the tensile properties of T91 grade steels at temperatures up to 550°C. It should, however, be noted that the presence of unusually high Si content may impair the ductility of the T91 grade steels. Therefore, additions of Si content ranging from 0.5 to 2.0 wt% to these steels were considered to provide the optimum tensile properties for their efficient utilization in the transmutation process.

It is well known that plastic deformation of engineering metals and alloys under tensile loading is associated with the development of linear defects such as dislocations. For successive deformation under continued loading, these dislocations have to move within the matrix as well as past the grain boundaries. Thus, for gradual plastic deformation, which is commonly characterized by ductility in terms of percent elongation (%El) and percent reduction in area (%RA), the movement of dislocation has to be continued until the material reaches the point of instability, where failure starts with necking, primarily in ductile materials. However, at elevated temperatures, such as the

operating temperature range associated with the spallation process, it is likely that solute elements (interstitial/substitutional) may diffuse into the matrix of the material, causing their eventual precipitation in the vicinity of the dislocations and grain boundaries. Such incidences can impede the movement of dislocations, leading to a gradual reduction in plastic strain within a susceptible temperature regime, beyond which the dislocations, once again, become free to move past the grain boundaries due to greater driving forces associated with the enhanced diffusivity of solute elements.

The reduced plastic strain is usually observed in the stress versus strain diagram obtained in tensile testing involving a metallic material of interest. The stress-strain diagrams may often be characterized by the development of serrations at certain temperatures, which may also be related to the diffusion of solute elements at those temperatures. The reduced plastic strain and the formation of serrations in the stress-strain diagrams are the result of a metallurgical phenomenon, known as dynamic strain ageing (DSA). It is appropriate to mention at this point that the candidate T91 grade steels with variable Si contents exhibited a similar phenomenon of DSA within a susceptible temperature range, showing both a gradual reduction in failure strain and the formation of serrations. Therefore, extensive efforts have been made in this investigation to develop a fundamental understanding of DSA of candidate target containment materials as functions of the Si content and other metallurgical variables.

DSA of structural materials is often influenced by both temperature and strain rate used in tensile testing. Even though the candidate structural materials, namely Si-containing T91 grade steels, were initially tested at temperatures ranging from ambient to 550°C under a strain rate of 5 X 10^{-4} sec^{-1}, additional testing was later performed

involving all four alloys both at faster and slower strain rates at selected temperatures. The selection of these testing temperatures was based on the results of initial tensile testing, where the concept of DSA was observed in terms of reduced failure strain and formation of serrations. The performance of these additional testing was aimed at evaluating the activation energy needed for the diffusion of solute elements that could significantly influence the occurrence of DSA phenomenon in the tested materials. Simultaneously, the magnitudes of work-hardening index and dislocation density of all four alloys were calculated as functions of the testing temperature and the Si content. The resultant data on the activation energy, work-hardening index and dislocation density have subsequently been analyzed in a systematic manner so that their synergistic effects could be incorporated in the development of a plausible mechanism of tensile deformation as functions of different metallurgical variables.

The toughness of structural materials can also play an important role in the identification and selection of suitable materials for high temperature applications such as transmutation of SNF. Thus, the determination of both plane-strain fracture toughness (K_{IC}) and impact toughness (CVN) are essential to evaluate the resistance of T91 grade steels to failure under tensile and impact loading in the presence of a notch. Further, both types of testing are capable of evaluating the effect of Si content on the fracture characteristics of martensitic alloys tested in this investigation. In view of this rationale, the determinations of K_{IC} and CVN have also been pursued in this investigation.

Metallography and fractography of the tested specimens can both play important roles to reinforce the fundamental understanding of the deformation mechanism. Therefore, analytical tools including optical microscopy, scanning electron microscopy and

transmission electron microscopy have been extensively used to develop a comprehensive deformation mechanism of T91 grade steels as functions of metallurgical and experimental variables. It is anticipated that the overall data generated from this investigation, and their systematic analyses will provide significant insight into the mechanistic understanding of tensile deformation including failure of martensitic alloys such as Fe-Cr-Mo-Nb-V steels as a function of Si content at ambient and elevated temperatures.

CHAPTER 2

TEST MATERIALS AND SPECIMENS

2.1 Materials

As mentioned in the previous chapter, modified 9Cr-1Mo steels, also known as T91 grade steels, were identified to be the primary structural materials to contain target for generation of neutrons that could eventually be utilized to activate the transmutation process of SNF. Since these containment materials should be capable of providing adequate corrosion resistance and superior tensile properties at elevated temperatures, the evaluations of the T91 grade steels were divided into two major research areas. One area was focused on the evaluation of the corrosion behavior of Si-containing T91 grade steels at ambient and elevated temperatures. The resultant experimental data have recently been presented in a dissertation defended by Maitra [5]. Simultaneously, extensive efforts have been ongoing to perform metallurgical characterization of T91 grade steels containing Si ranging from 0.5 to 2.0 wt.% under conditions relevant to the transmutation process. Si was added to T91 grade steels due to its beneficial effects with respect to both corrosion resistance and tensile properties, observed in several recent investigations [14-16] conducted at MPL of UNLV.

As opposed to regular 9Cr-1Mo martensitic steels, the T91 grade steels contain Nb and V to enhance their tensile properties and creep-rupture strength at elevated temperatures. In essence, martensitic stainless steels are the first stainless steel grades that

were commercially developed containing a relatively high carbon (0.1-1.2 wt.%) compared to that of other types of stainless steels. These materials are alloys of C and Cr having a body-centred-tetragonal (BCT) crystal structures in a hardened state. Due to their superior magnetic properties and high hardenability, these steels have found numerous applications including aerospace, general engineering and nuclear power generating reactors applications. Thus, austenitic stainless steels have been substituted by martensitic alloys. In view of the superior swelling resistance and excellent thermal properties of martensitic alloys, demonstrated twenty five years ago in the fast reactor research programs, conventional Cr-Mo steels having 9-12 wt.% Cr were later added to the fusion materials program in more recent years. The superior performance of martensitic Cr-Mo steels, compared to that of austenitic materials, can be attributed to their stable microstructures, high oxidation and sulphidation resistance, improved thermal conductivity, and low thermal expansion. The ambient temperature mechanical and physical properties of T91 grade steels are given in Tables 2-1 [17] and 2-2 [18], respectively.

Table 2-1 Tensile Properties of Modified 9Cr-1Mo Steel

Ultimate Tensile Strength (UTS)	85 ksi (586 MPa), minimum
Yield Strength (YS)	60 ksi (414 MPa), minimum
% Elongation (%El)	20, minimum
% Reduction in Area (%RA)	40, minimum
Hardness	248 H_B, minimum

Table 2-2 Physical Properties of Modified 9Cr-1Mo Steel

Density	7.6 gm/cc
Thermal Conductivity (λ)	27 $W.m^{-1}.K^{-1}$
Electrical Resistivity (ρ)	$55x10^{-8}$ $\Omega.m$

Modified 9Cr-1Mo steels (T91 grades) are generally available from prospective vendors in the United States. However, the availability of Si-containing T91 grade steels is almost scarce. In view of this scenario, four experimental heats of T91 grade martensitic steels containing four levels of Si (0.5, 1.0, 1.5, 2.0 wt.%) were custom-melted at the Timken Research Laboratory, Canton, Ohio, using a vacuum-induction-melting (VIM) practice. These VIM heats were subsequently processed into rectangular bars of desired dimensions using forging and hot-rolling. The hot-rolled products were then subjected to cold-rolling to reduce their thicknesses. These cold-worked materials had significant amount of residual stresses, which could usually be relieved by solutionizing them at relatively high temperatures for specific time periods.

For martensitic materials, such as Si-containing T91 grade steels, such thermal treatment is called austenitizing that was carried out at 1850°F (1110°C) for 1 hour and oil quenched. The purpose of quenching was to produce hard but brittle martensitic phase to achieve the desired strength. However, these materials are not workable to fabricate the desired testing specimens. Therefore, tempering treatment was performed to relieve these internal stresses and homogenize the resultant microstructures by heating them at 1150°F (621°C) for 1 hour, followed by air-cooling. A combination of quenching and tempering was necessary to produce fully tempered and fine-grained martensitic

microstructure throughout the matrix of the test materials without the formation of retained austenite. The chemical compositions of the Si-containing T91 grade steels, incorporated in this investigation, are given in Table 2-3.

Table 2-3 Chemical Compositions of T91 Grade Steels

Heat No.	Elements (wt %)												
	C	Mn	P	S	Si	Ni	Cr	Mo	Al	V	Cb	N(ppm)	Fe
2403	.12	.44	.004	.003	.48	.30	9.38	1.03	.024	.23	.91	57	Bal
2404	.12	.45	.004	.003	1.02	.30	9.61	1.03	.025	.24	.89	53	Bal
2405	.11	.45	.004	.004	1.55	.31	9.66	1.02	.024	.24	.085	49	Bal
2406	.11	.45	.004	.004	1.88	.31	9.57	1.01	.029	.24	.087	30	Bal

Bal: Balance

2.2 Test Specimens

2.2.1 Tensile Specimen

Smooth cylindrical specimens having 4-inch (101.4 mm) overall length, 1-inch (25.4 mm) gage length and 0.25-inch (6.35 mm) gage diameter were machined from four heats of heat-treated T91 grade steel bars in such a way that the gage section was parallel to the longitudinal rolling direction. A gage length (l) to gage diameter (d) ratio (l/d) of 4 was maintained for these specimens to comply with the size requirements of the ASTM Designation E 8 [19]. A pictorial view, and the detailed dimensions of the cylindrical specimens used in tensile testing (ambient and elevated temperatures) are shown in Figure 2-1. These specimens were also used to develop a basic understanding of tensile deformation as functions of temperature and strain rate, which usually manifests as a phenomenon of dynamic strain ageing (DSA).

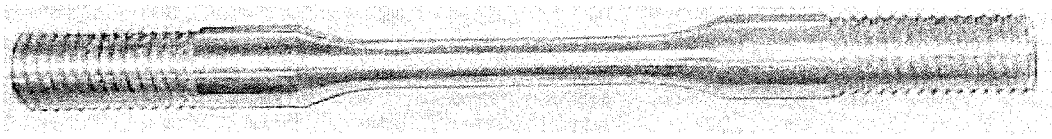

(a) Pictorial View

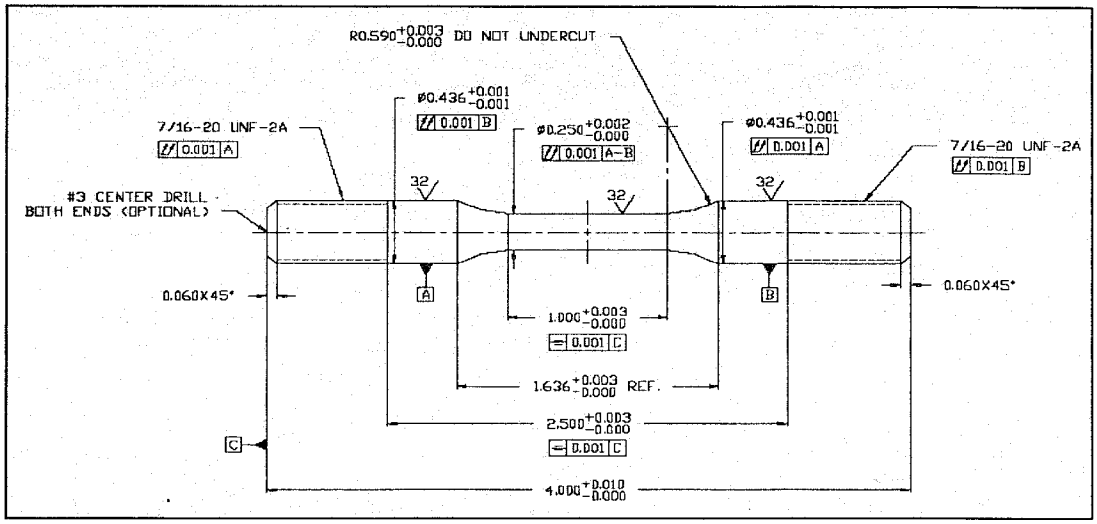

(b) Diagram showing Dimensions

Figure 2-1 Configuration of Smooth Cylindrical Specimen

2.2.2 Compact-Tension Specimen

The structural materials to contain target during the generation of neutrons contain sub-critical flaws including cracks, which may slowly propagate under the conditions relevant to the transmutation process. Therefore, significant efforts have been made to determine the fracture toughness (K_{IC}) of all four heats of T91 grade steels using pre-cracked compact-tension (CT) specimens at ambient and elevated temperatures. For evaluation of K_{IC} values, pre-cracked CT specimens having 1.25-inches (31.75 mm) length, 1.2-inches (30.48 mm) width and 0.5-inch (12.7 mm) thickness (Figure 2-2) were used. The machining of these specimens was performed to comply with the size requirements as prescribed by the ASTM Designation E 399-1990 [20] and E 1820-2001.

[21] The intersection of the crack starter notch tips with the top and bottom surfaces of these specimens were made equidistant within 0.005W, where W is the width of the specimen. A root radius of 0.003-inch (0.25 mm) was provided for the straight-through slot terminating in the V-notch of the specimen to facilitate fatigue pre-cracking at low stress intensity levels prior to the determination of K_{IC}. A width to thickness (B) ratio (W/B) of 4 was maintained during machining of the CT specimens [21].

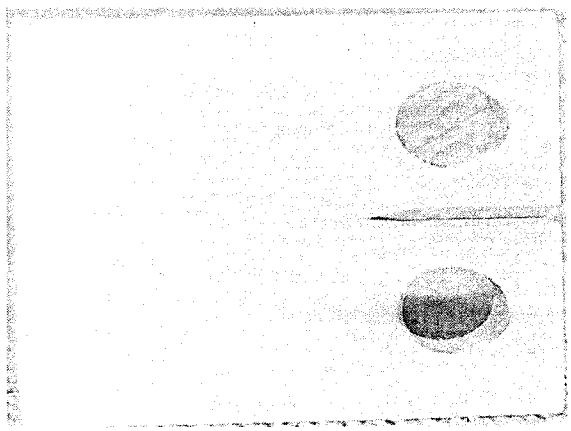

(a) Pictorial View

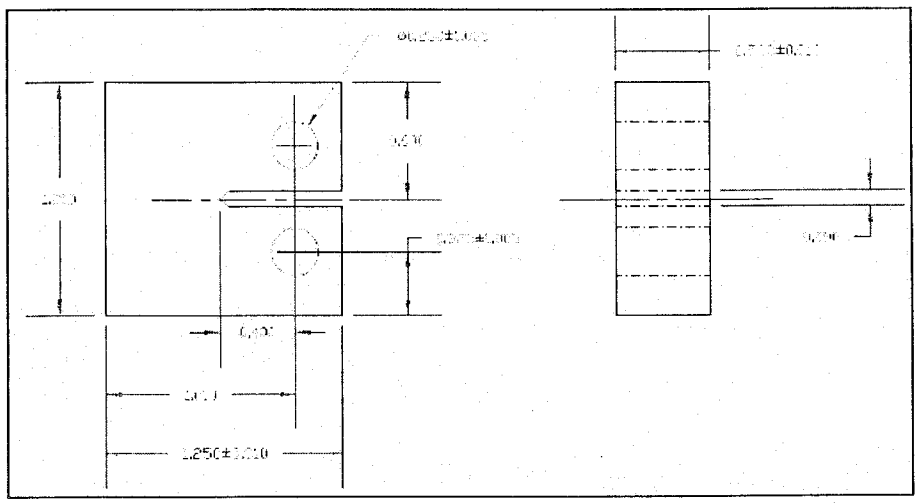

(b) Diagram showing Dimensions

Figure 2-2 Configuration of CT Specimen

2.2.3 Charpy V-notch Specimen

The structural materials to contain the target during the spallation process may also be subjected to impact loading. Thus, it is customary to evaluate the impact resistance of the containment material at different temperatures to estimate the impact energy and a ductile-to-brittle-transition-temperature (DBTT). A conventional method to determine impact energy and DBTT is to use notched rectangular specimen having configuration shown in Figure 2-3. These specimens, also known as the Charpy V-notch (CVN) specimens, were subjected to impact loading by striking them with a pendulum at a central location opposite to the notched region. CVN specimens of T91 grade steels having 2.164-inches (54.965 mm) length, 0.394-inch (10 mm) width, 0.315-inch (8 mm) thickness and a notch angle of 45° were machined in such a way that the length of these specimens was parallel to the longitudinal rolling direction. The dimensions, shown in Figure 2-3, comply with the size requirements prescribed by the ASTM Designation E 23 [22].

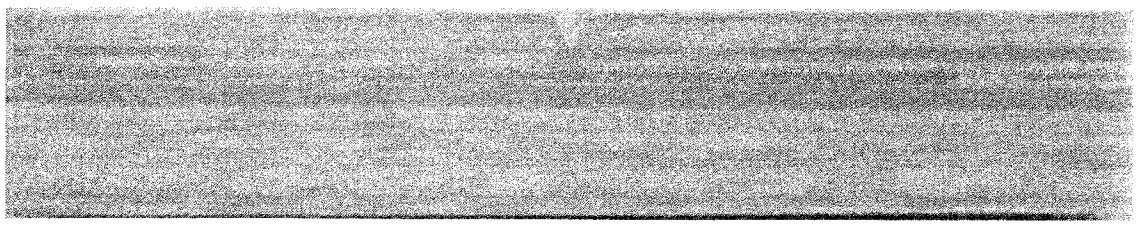

(a) Pictorial View

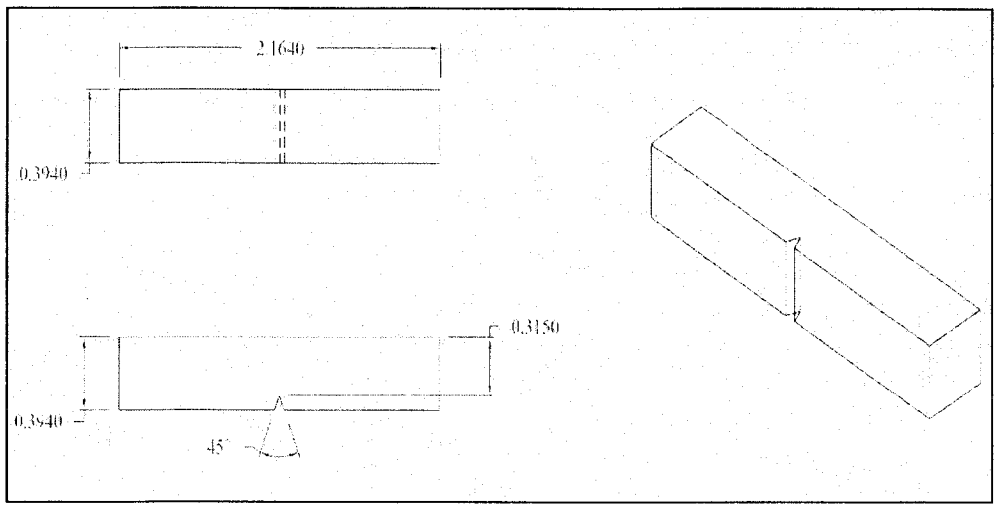

(b) Diagram showing Dimensions

Figure 2-3 Configuration of CVN Specimen

CHAPTER 3

EXPERIMENTAL PROCEDURES

This investigation is focused on the evaluation of high temperature mechanical and metallurgical properties of four heats of T91 grade martensitic steels containing different levels of Si. The tensile properties of these steels have been determined at temperatures ranging from ambient to 550°C by using an Instron mechanical testing system. The evaluation of fracture toughness (K_{IC}) using pre-cracked compact tension (CT) specimens was also performed using this equipment at ambient temperature and 300°C. Charpy V-notch (CVN) specimens were used to evaluate the impact toughness of all four heats of T91 grade steels at temperatures ranging from -40°C to 440°C. The metallographic and fractographic evaluations of all tested specimens were performed by using optical microscopy and SEM, respectively. The characterization of defects due to plastic deformation, diffusion of impurity elements and precipitates resulting from the transformation of phases at elevated temperatures have been performed by TEM. The detailed experimental procedures are described in the following subsections.

3.1 Tensile Testing

The tensile properties including the yield strength (YS), ultimate tensile strength (UTS), and the ductility in terms of percent elongation (%El) and percent reduction in

area (%RA) were evaluated using an Instron model 8862 equipment. Smooth cylindrical specimens were initially loaded in tension at a strain rate of 5×10^{-4} sec^{-1} according to the ASTM Designation E 8-2004. [19] The experimental data including the load, time, extensometer reading, engineering stress and engineering strain were recorded in the data file. Three specimens were tested under each experimental condition, and the average values of the measured parameters were recorded. The engineering stress versus engineering strain (s-e) diagrams were automatically generated using the Bluehill 2 software program [23] that enabled the data acquisition during tensile testing. The magnitudes of YS, UTS, and %El based on the linear variable displacement transducers (LVDT) measurements at each temperature, were also evaluated using this software. YS was determined by the point of intersection of a line drawn parallel to the linear portion of the s-e diagram at a strain offset value equivalent to 0.2% of the strain. Upon completion of testing, the magnitudes of %El and %RA were calculated using Equations 3-1 through 3-4.

$$\%\ El = \left(\frac{L_f - L_o}{L_g} \right) \times 100 \quad ; \quad L_f > L_o \qquad \text{Equation 3-1}$$

$$\%RA = \left(\frac{A_o - A_f}{A_o} \right) \times 100 \; ; \quad A_o > A_f \qquad \text{Equation 3-2}$$

$$A_o = \frac{\pi \times D_o^{\,2}}{4} \qquad \text{Equation 3-3}$$

$$A_f = \frac{\pi \times D_f^{\,2}}{4} \qquad \text{Equation 3-4}$$

Where, A_0 = Initial cross sectional area ($inch^2$)

A_f= Cross sectional area at failure (inch^2)

L_o= Initial overall length (inch.)

L_f= Final overall length (inch.)

L_g = Initial gage length (inch.)

D_o= Initial gage diameter (inch.)

D_f= Final gage diameter (inch.)

The Instron testing machine, shown in Figure 3-1, had an axial load transducer capacity of 22.5 kip (100 kN). It had a single screw electromechanical top actuator that was developed for static and quasi-dynamic cyclic testing at slow speed. This equipment consisted of a large heavy-duty load frame with an adjustable crosshead attached to the top grip, and a movable actuator with another grip at the bottom to enable loading and unloading of the test specimen. The axial motion was controlled by force, displacement, or an external signal from the strain gage. The specimen was mounted between the two grips and pulled by the movable actuator. The load cell measured the applied force on the tensile specimen. The movement of the upper crosshead relative to the lower one measured the strain within the specimen. The key specifications of the Instron equipment are given in Table 3-1. [24]

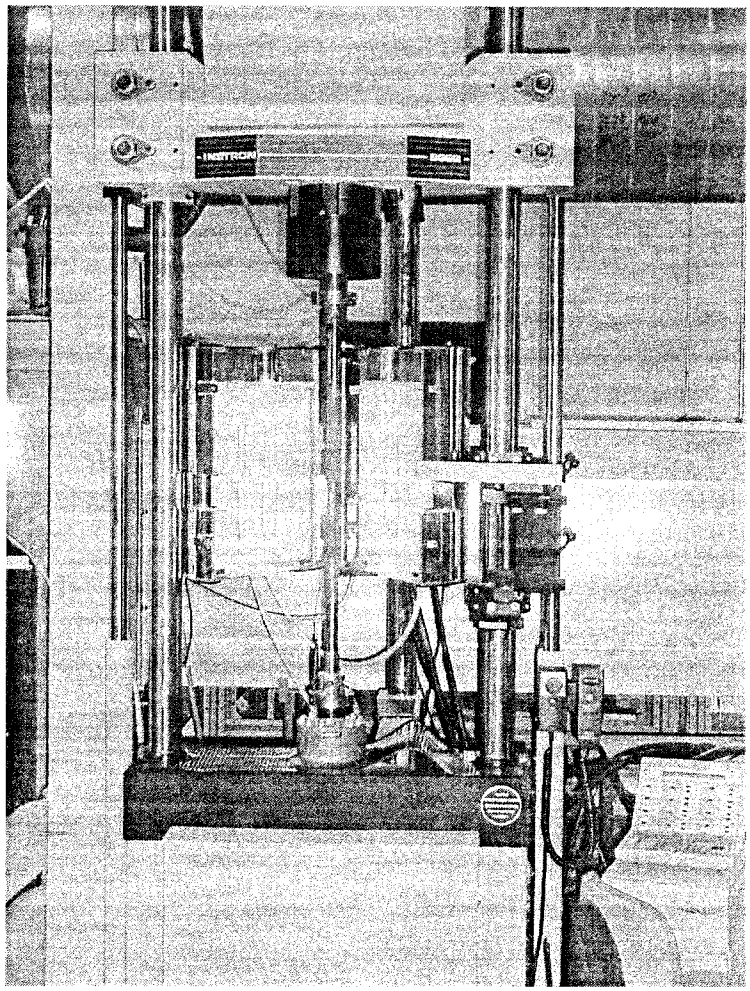

Figure 3-1 Instron Testing Machine

Table 3-1 Specifications of Instron Model 8862 System

Load Capacity, kN	Total Actuator Stroke, mm	Maximum Ramp Rate, mm/min	Actuator Attachment Threads	Load Cell Attachment Threads
100	100	350	M30 × 2	M30 × 2

A split furnace (model MDS1735A) was attached to the Instron unit for heating the cylindrical test specimens at the desired temperatures in the presence of nitrogen. This furnace was capable of sustaining a maximum temperature of 1500°C, and consisted of two water-cooled stainless steel jackets that provided a safe ergonomic outer surface for operation. Two layers of micro-pores and ceramic fibers were placed inside this furnace. Six U-shaped molybdenum disilicide heating elements were used for attaining the desired testing temperature. The desired temperature during straining was monitored by three B-type thermocouples contained inside the test chamber. A separate control panel (model CU666F) was used to perform the overall monitoring of temperature during tensile loading. A maximum heating rate of 10°C per minute could be achieved by this control panel. However, a slow heating rate of 4°C per minute was used during testing to prevent any thermal shock of the pull rods and the fixtures inside the furnace. Since the grip material could undergo plastic deformation and phase transformation at elevated temperatures during straining of the specimen, a pair of custom-made grips made of high strength and temperature resistant MarM 246 alloy was used to hold the tensile specimen in an aligned position. A positive pressure was maintained inside the heating chamber by continuously purging nitrogen through it, which also ensured the elimination of oxygen from the test chamber, thereby preventing surface contamination of the specimen.

3.1.1 Dislocation Density Calculation

Dislocation density (ρ) was computed from the TEM micrographs of the tested tensile specimens to evaluate the DSA effect at four different temperatures (RT, 300, 400 and 550°C) at a strain rate of 5×10^{-4} sec^{-1}. The magnitude of ρ was determined by the line intersection method based on the superimposition of a grid of horizontal and vertical test

lines on the TEM micrographs containing dislocations, as shown in Figure 3-2. [25-28] The grid was placed in multiple locations so as to determine the average value of ρ based on a large value of intersection with TEM micrographs. The ρ value was calculated using Equation 3-5. [28] The average thickness (t) of the sample was measured using electron energy loss spectroscopy (EELS) technique available in the TEM. EELS was used to measure the thickness of the samples at different locations using Equation 3-6. [29] An example of the local thickness calculation using EELS is illustrated in Figure 3-3, showing thickness calculations at six different locations of a tested specimen.

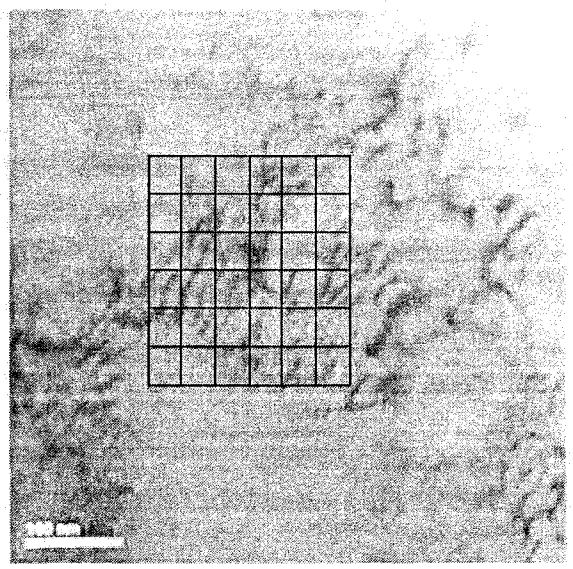

Figure 3-2 Dislocation Density Calculation by Line Intersection Method

$$\rho = \frac{1}{t}\left(\frac{\sum n_v}{\sum L_v} + \frac{\sum n_h}{\sum L_h}\right) \qquad \text{Equation 3-5}$$

$$t = \lambda \ln(I_t/I_o) \qquad \text{Equation 3-6}$$

Where, $\sum n_v$ = Number of intersections of vertical test lines with dislocations

$\sum n_h$ = Number of intersections of horizontal test lines with dislocations

$\sum L_v$ = Total length of vertical test lines (meters)

$\sum L_h$ = Total length of horizontal test lines (meters)

λ = mean free path (calculated using an online software [30]

I_t = total intensity reaching the spectrometer

I_o = zero-loss intensity reaching the spectrometer

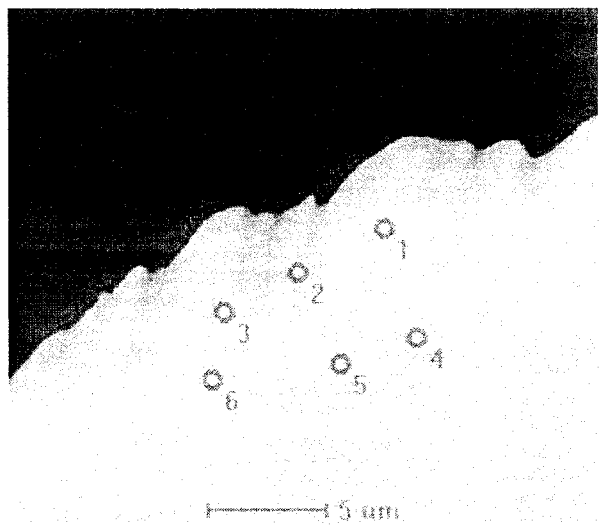

Figure 3-3 EELS Measurement to Compute Average Thickness

3.1.2 Activation Energy Calculation

As mentioned in Chapter 1, the phenomenon of dynamic strain ageing (DSA) showing reduced failure strain and serrations within certain temperature regimes, is a function of both temperature and strain rate. The gradual reduction in failure strain (e_f) was observed at the initially applied strain rate of 5×10^{-4} sec^{-1}. In order to study the effect of strain rate on the DSA behavior of all four heats of Si-containing T91 grade

steel, testing was performed at three additional strain rates of 10^{-2}, 10^{-3} and 10^{-4} sec^{-1} at selected temperatures of 200, 300 and 400°C that fell within the susceptible temperature range, where the DSA phenomenon was observed. Even though the magnitude of e_f was minimum at 400°C, serration in the s-e diagram was most prominent at 300°C. At least duplicate testing was performed at each of these strain rates.

It is well-known that the occurrence of DSA [31-38] is the result of the diffusion of interstitial and substitutional solute elements into the matrix of a susceptible material. Since diffusion is a thermally-activated process, the determination of the activation energy (Q) based on the testing temperatures seems appropriate to develop a fundamental understanding of the mechanism of plastic deformation of alloys of interest. Further, it is well established [35-37, 39,40] that the critical true plastic strain (ε_c) to initiate the formation of serrations is a function of both the temperature and true strain rate ($\dot{\varepsilon}$) according to the Equation 3-7. [39,40]

$$\varepsilon_c^{(m+\beta)} = K\dot{\varepsilon}\exp\left(\frac{Q}{RT}\right) \qquad \text{Equation 3-7}$$

Where, Q = Activation energy at the onset of serrations (KJ/mole)

R = Universal gas constant (8.3144 J/mole K)

T = Absolute temperature (K)

m, β = Exponents related to the variation of vacancy concentration (C_v) and mobile dislocation density (ρ_m)

K = Constant

It has been postulated [35,36] that C_v and ρ_m can be related to the true strain (ε) according to the empirical relationships, given by Equations 3-8 and 3-9. The magnitude of Q can be determined by a method [35,36] based on the application of Equation 3-7, in which the natural logarithm of ε_c is plotted as a function of 1/T at a constant $\dot{\varepsilon}$, thus giving a straight line having a slope of [Q/R(m+β)], as shown in the modified expression given by Equation 3-8.

$$C_v \propto \varepsilon^m \qquad \text{Equation 3-8}$$

$$\rho_m \propto \varepsilon^\beta \qquad \text{Equation 3-9}$$

Taking natural logarithm (ln) on both sides of Equation 3-7, Equation 3-10 can be developed that represents a straight line in the form of y = Ax + B, where A is the slope of the straight line given by [Q/R(m+β)]. Equation 3-7 can be rearranged as Equation 3-11, which also represents a straight line with a slope of (m+β) when $\ln \dot{\varepsilon}$ is plotted as a function of $\ln \varepsilon_c$ at a constant T. Taking the value of $(m+\beta)$, the magnitude of Q can be determined from the slope [Q/R(m+β)] of the straight line represented by Equation 3-10.

$$\ln \varepsilon_c^{(m+\beta)} = \ln\left[K \dot{\varepsilon} \exp\left(\frac{Q}{RT}\right)\right]$$

$$\text{or, } (m+\beta)\ln \varepsilon_c = \ln K + \ln \dot{\varepsilon} + \left(\frac{Q}{RT}\right)$$

$$\text{or, } \ln \varepsilon_c = \frac{Q}{R(m+\beta)} \times \frac{1}{T} + \frac{\left(\ln K + \ln \dot{\varepsilon}\right)}{(m+\beta)} \qquad \text{Equation 3-10}$$

$$\ln \dot{\varepsilon} = (m+\beta) \ln \varepsilon_c - \left[\ln K + \frac{Q}{RT}\right] \qquad \text{Equation 3-11}$$

3.1.3 Computation of Strain-Hardening Exponent

Metallic materials can experience work hardening resulting from dynamic loading beyond the elastic limit. [41] The extent of work hardening, commonly expressed as strain hardening exponent (n), is known to be related to both the true stress and true strain by Equation 3-12. [41, 42] This equation is also known as the Hollomon relationship. [43,44] Under an ideal condition, the magnitude of n can be determined from the slope of a straight line obtained by plotting $\log\sigma$ vs. $\log\varepsilon$ at a constant temperature, as given by Equation 3-13.

$$\sigma = K\varepsilon^n \qquad \text{Equation 3-12}$$

$$\log\sigma = \log K + n \log\varepsilon \qquad \text{Equation 3-13}$$

Where, σ = True stress, ksi or MPa

ε = True strain

K = Constant, known as strain hardening (strength) coefficient

3.2 Fracture Toughness Evaluation

The plane-strain fracture toughness (K_{IC}) of T91 grade steels was determined by loading CT specimens under tension in the Instron model 8862 testing unit according to ASTM Standard E 399-1990. [20] The CT specimens were pre-cracked up to a maximum length of 2 mm at a stress ratio ($R = \sigma_{min}/\sigma_{max}$) of 0.1 at applied loads below the material's yield point using a frequency of 1 Hz. K_{IC} measurements were performed using a fracture toughness software program provided by the Instron Corporation. An extensometer was attached to the CT specimen during straining of the CT specimen at a rate of 2 mm per minute to determine the conditional stress intensity factor (K_Q) value. Depending on the type of the test material, three different types of load versus displacement (P-v) curves can be generated, as shown in Figure 3-4. [20,21]

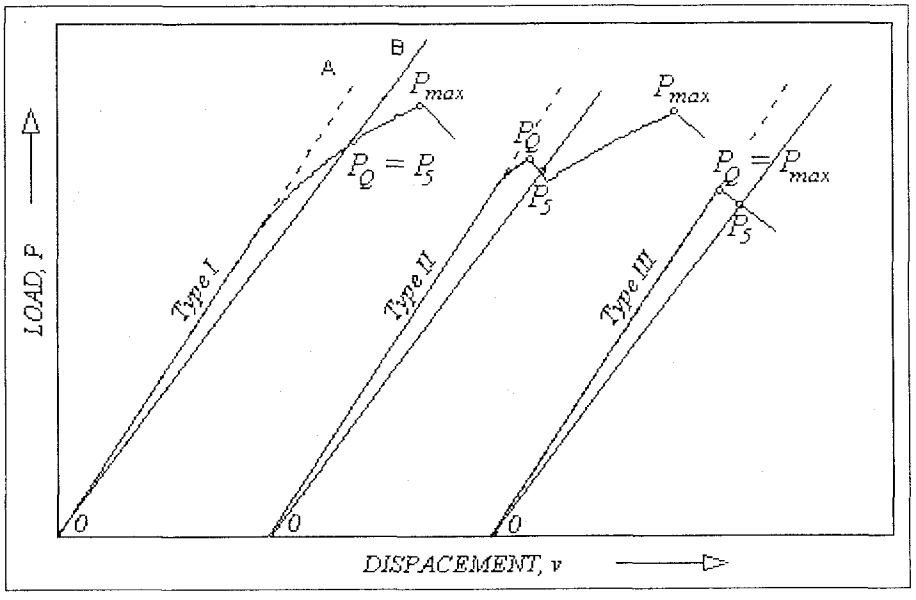

Figure 3-4 Conventional Types of P-v Curves [20]

Type I represents a classical P-v plot for common ductile materials. Metallurgically speaking, T91 grade steels can usually be classified as intermediate ductile materials. A line OA was drawn tangent to the initial linear portion of the resultant P-v curves corresponding to all four heats of materials. A second line OB, known as the 5% secant line, with a slope equivalent to 95% of the initial load line, was subsequently drawn. The point, at which the load-displacement curve intersected the 5% secant line was identified as P_5 in this curve. P_5 was taken as the critical or conditional load (P_Q), which was then used to calculate K_Q using Equation 3-14 [20]. The magnitude of K_Q, determined by this method, is commonly taken to be a valid K_{IC} if the relationships [20,21] given by Equations 3-16, 3-17 and 3-18 are satisfied.

$$K_Q = \frac{P_Q}{B\sqrt{W}} f\left(\frac{a}{W}\right) \qquad \text{Equation 3-14}$$

$$f\left(\frac{a}{W}\right) = \frac{\left[2+\frac{a}{W}\right]\left[0.886+4.64\frac{a}{W}-13.32\left(\frac{a}{W}\right)^2+14.72\left(\frac{a}{W}\right)^3-5.6\left(\frac{a}{W}\right)^4\right]}{\left(1-\frac{a}{W}\right)^{\frac{3}{2}}}$$

Equation 3-15

$$0.45 \le \frac{a}{W} \le 0.55 \qquad \text{Equation 3-16}$$

$$P_{\max} \le 1.1 P_Q \qquad \text{Equation 3-17}$$

$$a, b, (W-a) \ge 2.5\left(\frac{K_Q}{\sigma_{YS}}\right)^2 \qquad \text{Equation 3-18}$$

Where, B = Specimen thickness (mm)

a = Crack length (mm)

W = Specimen width (mm)

$f\left(\frac{a}{W}\right)$ = A dimensionless function of a/W, also known as geometric factor, determined using Equation 3-17. [20,21]

P_{max} = Maximum load

σ_{YS} = Yield strength of the test material

3.3 Impact Toughness Evaluation

The resistance of a material to plastic deformation can be significantly influenced by the presence of imperfections such as cracks or notches. The presence of such imperfections in a structural material can impair the load bearing capabilities due to the generation of triaxial stresses in the vicinity of either cracks or notches. One way of evaluating the fracture toughness of a notched material is to strike it from the opposite end with an impact loading so as to cause its failure in a pre-mature manner. A notched rectangular specimen, shown in previous chapter is commonly used to determine the impact toughness in terms of energy absorbed prior to fracture due to the application of an impact load at a very high strain rate using a pendulum. In general, medium and low strength fcc materials and most hcp metals and alloys posses superior impact toughness even in the presence of a notch. On the contrary, high strength materials are very susceptible to brittle failure due to impact loading at all operating temperatures. However, the extent of failure with all engineering materials is more pronounced at lower temperatures, approaching cryogenic conditions. Thus, engineering materials can exhibit notch tough to notch brittle behavior with reducing temperature beyond a critical value known as the ductile-to-brittle-transition-temperature (DBTT).

The lower the magnitude of DBTT, the greater is the impact toughness of a material of interest. The precise determination of DBTT is very difficult. Usually, the impact energy of a material is determined as a function of temperature ranging from very low to appreciably high temperature. A typical impact energy versus temperature plot is illustrated in Figure 3-5, from which the magnitude of transition temperature based on different criteria can be established. Lower values of impact energy signify brittleness of a material. On the other hand, the lowest possible critical temperature is an indication of greater toughness.

The shape of the typical energy absorbed (C_v) versus temperature curve [45] (Figure 3-5) shows that there are various criteria for defining the transition temperature. The most conservative one is to select T_1, corresponding to the upper shelf in fracture energy and the temperature above which the fracture is 100 percent fibrous. This transition temperature criterion is called the fracture transition plastic (FTP). The FTP is the temperature at which the fracture changes from totally ductile to substantially brittle. The probability of brittle failure is negligible above the FTP. The use of the FTP is very conservative and in many applications it may be impractical. An arbitrary, but less conservative criterion is to base the transition temperature on 50 percent cleavage-50 percent shear, T_2. This is called a fracture-appearance transition temperature (FATT). Another criterion is to define the transition temperature as the average of the upper and lower shelf values, T_3. A common criterion is to define the transition temperature T_4 on the basis of an arbitrary low value of energy absorbed C_v. This is often called the ductility transition temperature. A well defined criterion is to base the transition temperature on

the temperature at which the fracture becomes 100 percent cleavage, T_5. This point is known as nil ductility temperature (NDT).

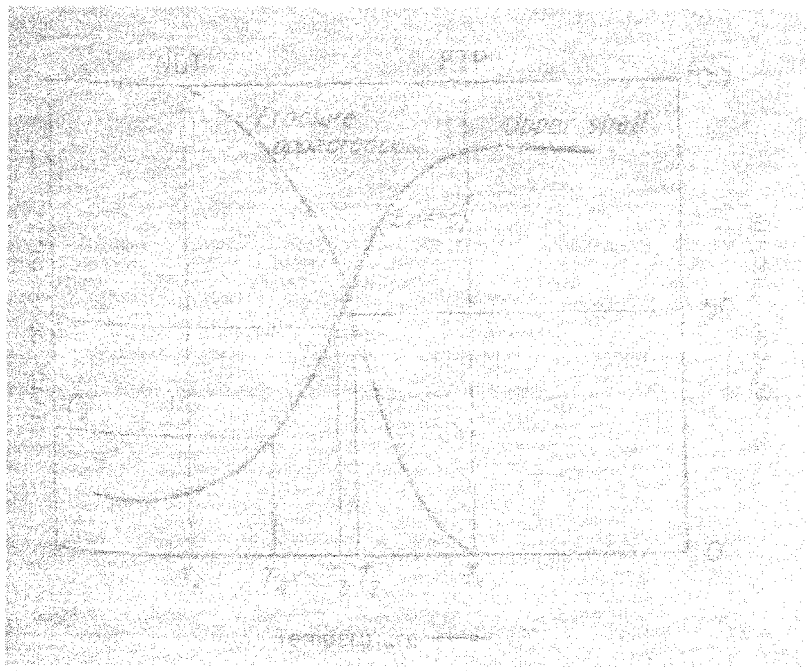

Figure 3-5 Various Criteria of Transition Temperature [45]

The impact toughness of Si-containing T91 grade steels was determined in this investigation by using an Instron Pendulum Impact Tester (SI-1K3 model) as shown in Figure 3-6. This equipment consisted of a heavy duty steel base on which the specimen holder (vise) and a heavy pendulum was mounted from a vertical shaft. This shaft was supported by precision ball bearings. A single lever located on top of this head assembly performed three functions of applying brake, releasing the break and placing a latch. Prior to impact loading, the hammer was placed at a fixed position followed by releasing the latch, causing the rupture of the specimens. An indicator dial attached to this equipment recorded the absorbed energy in terms of either joules or feet-pounds. The

specimens in the present investigation were tested at various temperatures ranging from cryogenic (-40°C) up to 440°C. A cryogenic temperature was attained by immersing CVN specimens inside an insulated styrofoam box containing dry ice and denatured alcohol.

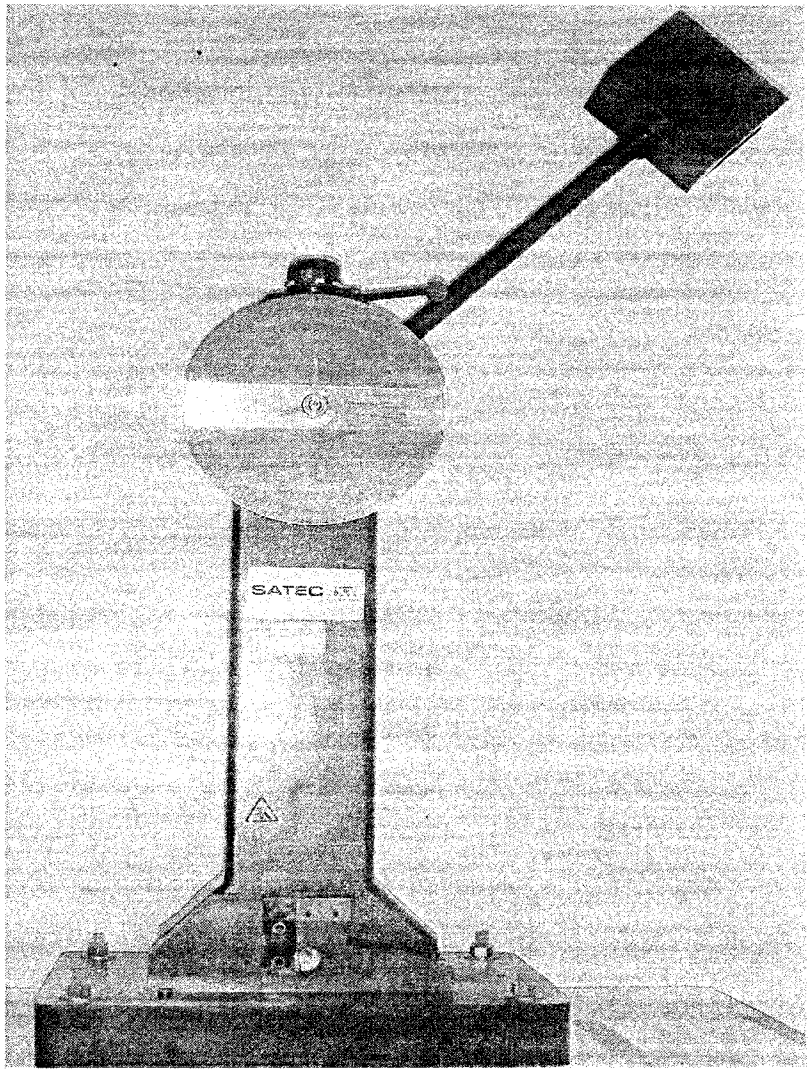

Figure 3-6 Charpy Impact Tester

3.4 Metallographic Evaluations

The microstructure plays an important role in differentiating properties of one alloy versus other. Thus, the evaluation of the metallurgical microstructure constitutes a significant step in characterizing the performance of a material of interest. The metallographic techniques using an optical microscope enable the characterization of phases present, their distributions within grains, and their sizes that depend on the chemical composition of the material, and the thermal treatments imparted to it. The principle of an optical microscope is based on the impingement of a light source perpendicular to the test specimen. The light rays pass through the system of condensing lenses and the shutters up to the half-penetrating mirror. This brings the light rays through the objective to the surface of the specimen. Light rays are reflected off the surface of the sample, which then return to the objective, where they are gathered and focused to form the primary image. This image is then projected to the magnifying system of the eyepiece. The contrast observed under the microscope results from either an inherent difference in intensity or wavelength of the light absorption characteristics of the phases present. It may also be induced by preferential staining or attack of the surface by etching with a chemical reagent.

The test specimens of T91 grade steels were sectioned and subsequently mounted using the standard metallographic techniques, followed by polishing and etching to reveal the microstructures. The etchant used was "Beraha's Reagent" that consisted of 3 grams of $K_2S_2O_3$ and 10 grams of $Na_2S_2O_3$ in 100 ml of H_2O. [46] The polished and etched specimens were then subjected to their microstructural evaluation using a Leica optical microscope, shown in Figure 3-7. This microscope had a maximum magnification of

1000X. A digital camera with a resolution of 1 mega pixel enabled image capture on a computer screen utilizing a Leica software.

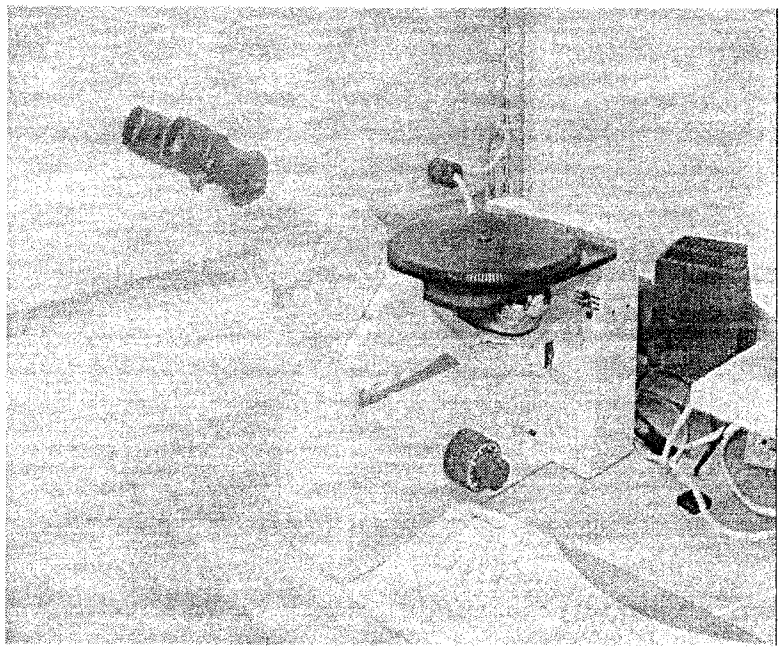

Figure 3-7 Leica Optical Microscope

3.5 Fractographic Evaluations

The extent and morphology of failure of the tested specimens were determined using Jeol-5600 scanning electron microscope (SEM). Analyses of failures in metals and alloys involve identification of the type of failure. The test specimens were sectioned into 1/2 to 3/4 of an inch in length to accommodate them in a vacuum chamber of the SEM. Failures can usually be classified into two types including ductile and brittle. [47] Dimpled microstructure is a characteristic of ductile failure. Brittle failure can be of two types, intergranular and transgranular. An intergranular brittle failure is characterized by crack

propagation along the grain boundaries while a transgranular failure is characterized by crack propagation across the grains.

In SEM evaluations, electrons from a metal filament are collected and focused similar to light waves into a narrow beam. The beam scans across the subject, which is synchronized with a spot on a computer screen. Electrons scattered from the subject are detected and can create a current, the strength of which makes the spot on the computer brighter or darker. This current can create a photograph-like image with an exceptional depth of field. Magnifications of several thousands could be achieved by use of this SEM. This SEM was also capable of distinguishing different features located at distances greater than 50 nm. The sample holder could accommodate multiple sizes of specimens ranging from 1 to 3.2 cm. However, the number of specimens was limited by their sizes. The morphology at the primary fracture surface of the tested tensile specimens, and at the ruptured surfaces of the CVN specimens were both analyzed by this SEM.

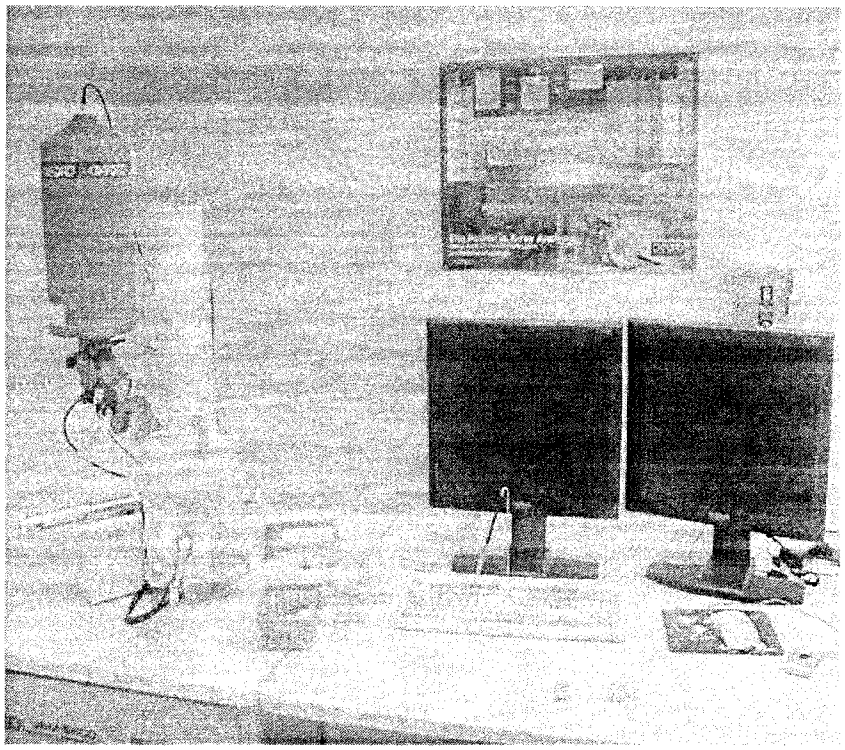

Figure 3-8 Scanning Electron Microscope

3.6 Transmission Electron Microscopy

TEM studies were conducted to characterize defects including dislocations in the tested tensile specimens using a Tecnai G^2 F30 S-TWIN Transmission Electron Microscope (Figure 3-9). This equipment operates with as high as 300kV acceleration voltage that allows a point-to-point resolution of 0.2 nanometer. Magnifications up to 1,000,000 times can be achieved with this TEM. This system is fully loaded including HAADF (high angle annular dark field) detector, EDX (X-ray energy disperse spectrometry), and GIF (Gatan Image Filter). Multiple samples were prepared from each tested specimen condition to obtain TEM micrographs. The sample preparation technique is described in details in the next subsection.

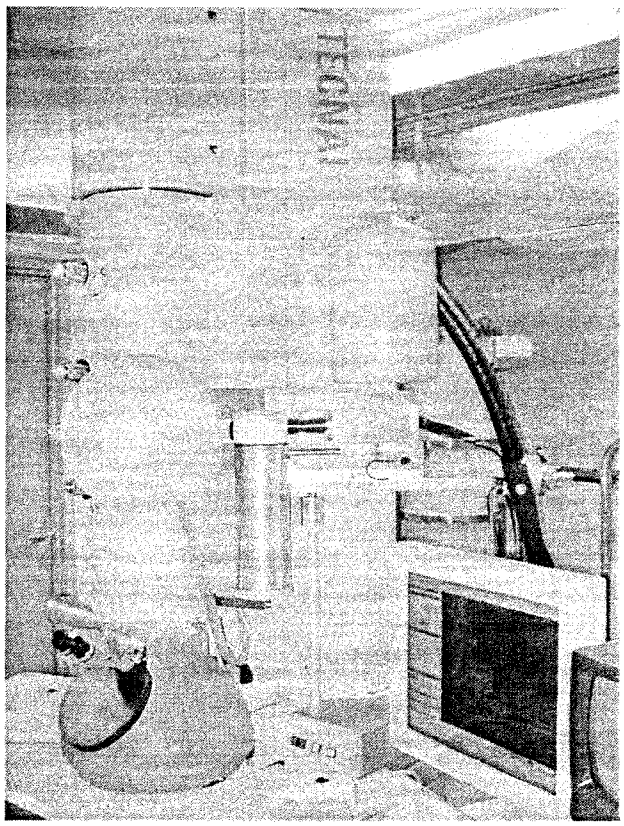

Figure 3-9 Transmission Electron Microscope

3.6.1 TEM Sample Preparation

Sample preparation for the TEM study involves a state-of-art technique. To ensure electron transparency of the sample by the TEM method, the specimen thickness was maintained between 50-100 nanometers. This was achieved through a series of operations, as described below. [25, 48-49]

- Initially, multiple circular disc-shaped samples were cut from the gage length of the failed tensile specimens up to a thickness of 500–700μm, using a precision cutter in the Materials Performance Laboratory (MPL).
- Samples were then mechanically ground (Figure 3-10) to about 100–150 μm using a grinder in the TEM Sample Preparation Laboratory. This process involved

two steps; rough-grinding and fine-polishing. Specimen thickness was monitored periodically during this process.

- The samples were then punched into 3mm diameter discs, using a disc puncher (Figure 3-11).
- Finally, electro-polishing was done to achieve the desired specimen thickness. A twin-jet TenuPol-5 electro polisher (Figure 3-12) was used for this purpose. This process involved removal of material from the sample surface as well as surface finish prior to TEM observation. The thinnest area was obtained around the perforation area. The composition of the electrolyte used for the process was 5% perchloric acid ($HClO_4$) in methanol (CH_3OH) with an applied potential of 50V, a pump flow rate of 12 and a temperature of -6°C. [50] Care was taken to control the flow of electrolyte to prevent the formation of anodic film that could cause etching of the specimen rather than polishing. [25, 51]

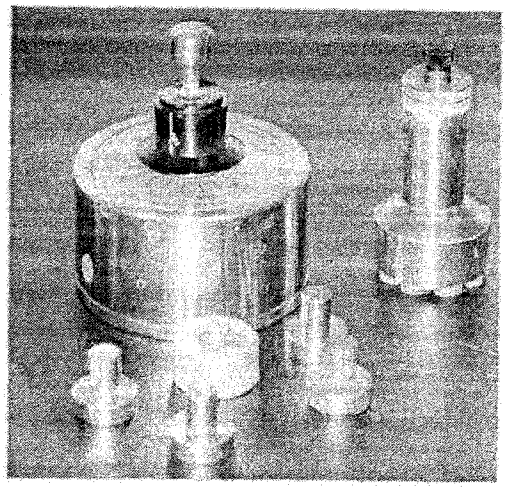

Figure 3-10 Grinding Accessories

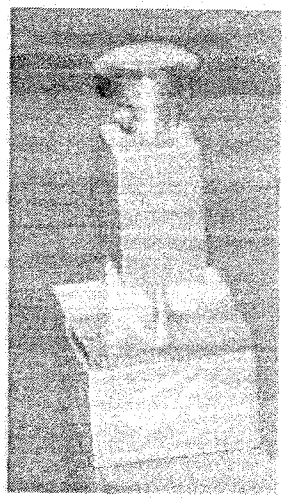

Figure 3-11 Disc Puncher

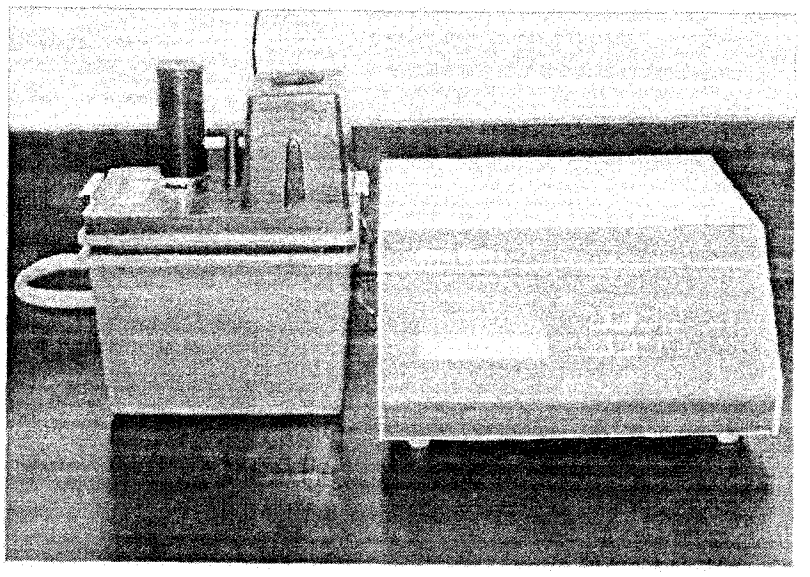

Figure 3-12 TenuPol-5 Electro-polisher

CHAPTER 4

RESULTS

The plastic deformation of structural materials such as martensitic T91 grade steels can be significantly influenced by the type of loading, temperature and strain rate. Different types of loading including tensile, impact and cyclic have been applied in this investigation to T91 grade steels having four levels of Si content for their prospective applications as target structural material in the transmutation of SNF and HLW. The role of temperature and strain rate on plastic deformation of these alloys under tensile testing has also been investigated. This section presents the results of tensile testing, impact testing, and fracture toughness evaluations of T91 grade steels as functions of different metallurgical and mechanical variables. Further, an in-depth analysis of metallographic and fractographic characteristics has been performed to develop plausible mechanisms of deformation of these alloys under different loading conditions.

4.1 Microstructural Evaluation

The optical micrographs of all four heats of T91 grade steels are shown in Figures 4-1 through 4-4 using two types of etchants, namely 5 volume percent nital and Beraha's reagent. The purpose of using Beraha's reagent was to reveal prior austenitic grain boundaries more prominently, and to expose the ferrite phases resulting from thermal treatments imparted to these alloys. An evaluation of these micrographs exhibits larger

austenitic grain boundaries containing finely-dispersed tempered martensitic phases, and ferrites that are identified by dark globular spots. For materials, where no microstructural distinctions could be made using these etchants, optical micrographs based on Beraha's reagent are included in these figures. It should be noted that streaks of martensitic laths [52], oriented in different directions, are also visible within finely-dispersed tempered martensitic structures (Figure 4-2 through 4-4), possibly due to the positioning of the metallographic mounts in directions that were different from original rolling direction.

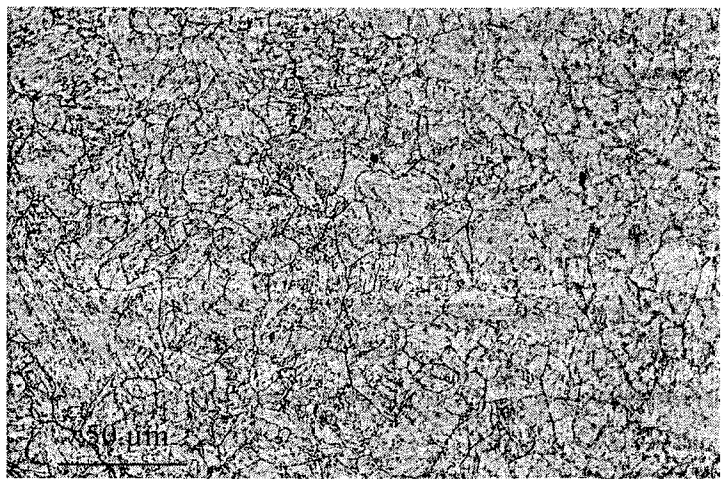

(a) Etchant: 5 volume % Nital, 500X

(b) Etchant: Beraha's Reagent, 500X

Figure 4-1 Optical Micrographs of Steel with 0.5 wt% Si

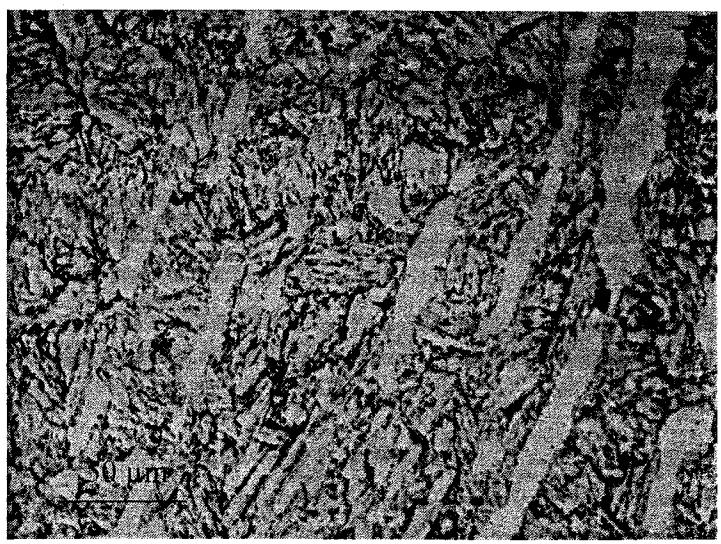

Figure 4-2 Optical Micrograph of Steel with 1.0 wt% Si, Beraha's Reagent, 500X

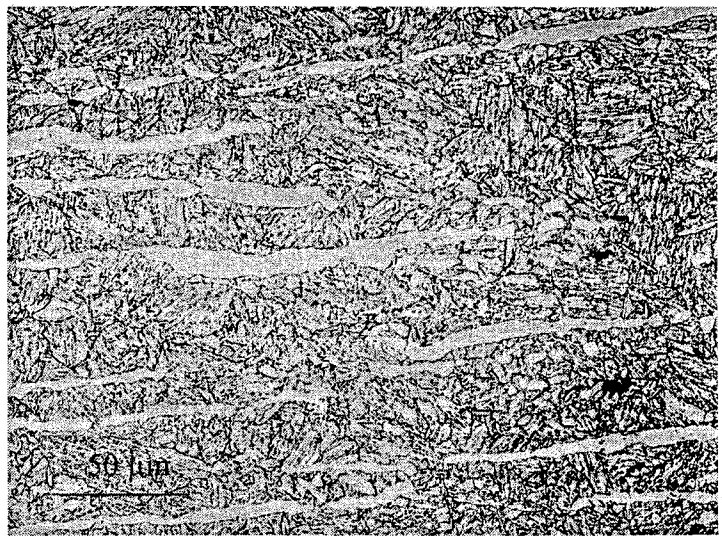

(a) Etchant: 5 volume % Nital, 500X

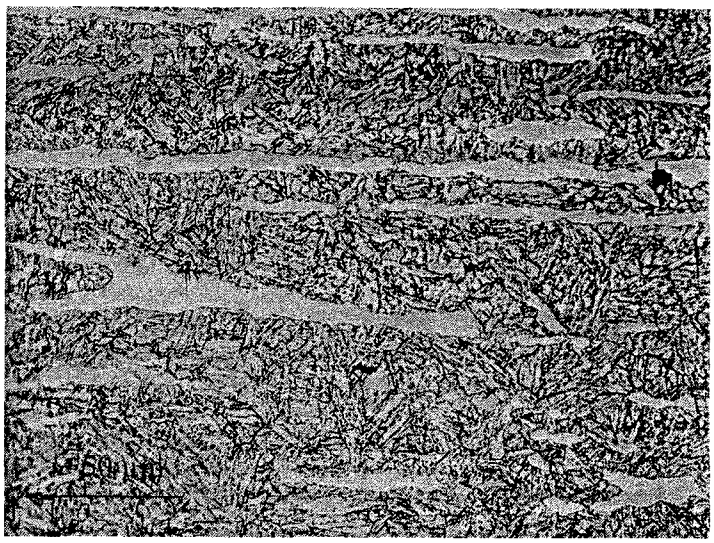

(b) Etchant: Beraha's Reagent, 500X

Figure 4-3 Optical Micrographs of Steel with 1.5 wt% Si

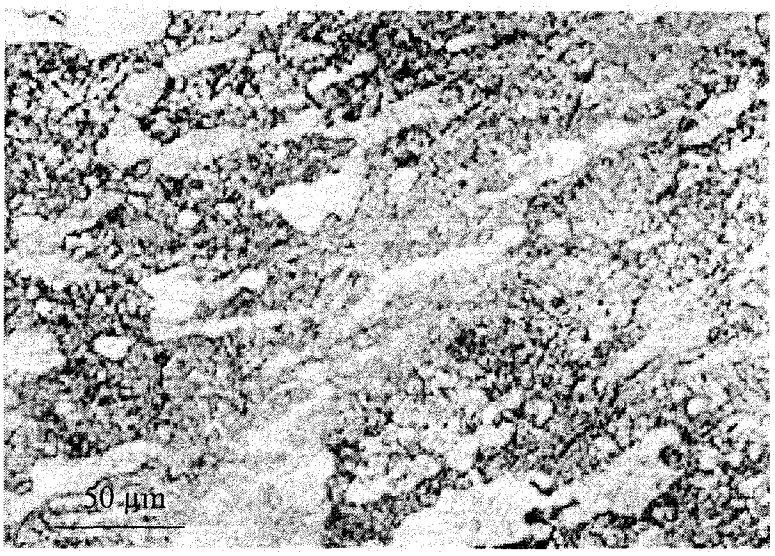

Figure 4-4 Optical Micrograph of Steel with 2.0 wt% Si, Beraha's Reagent, 500X

4.2 Tensile Properties Evaluation

The results of tensile testing involving all four Si-containing T91 grade steels, performed at an engineering strain rate of $5x10^{-4}$ sec^{-1}, are illustrated in Figures 4-5

through 4-8 in the form of superimposed engineering stress versus engineering strain (s-e) diagrams at temperatures up to 550°C. Even though a maximum operating temperature of 550°C had been recommended for efficient generation of neutrons using the spallation process, the effect of other temperatures including room temperature, 150, 300, and 400°C on the tensile deformation of T91 grade steels has also been investigated. A cursory examination of these s-e diagrams clearly reveals that, in general, the failure strain (e_f) was gradually reduced with an increase in temperature from ambient to 400°C. Simultaneously, a tendency to form serrations was also observed at some elevated temperatures, exhibiting its maximum propensity at 300°C.

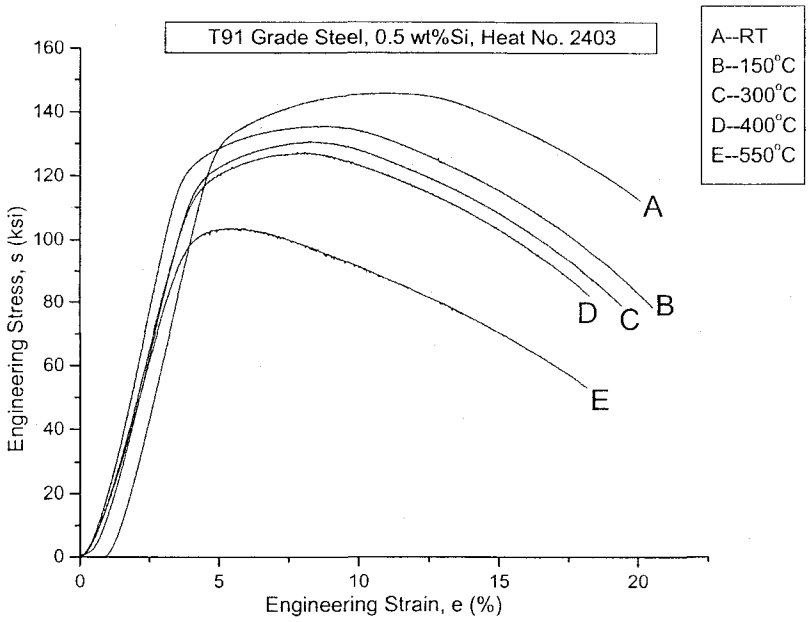

Figure 4-5 s-e Diagram vs. Temperature for 0.5 wt.% Si Steel

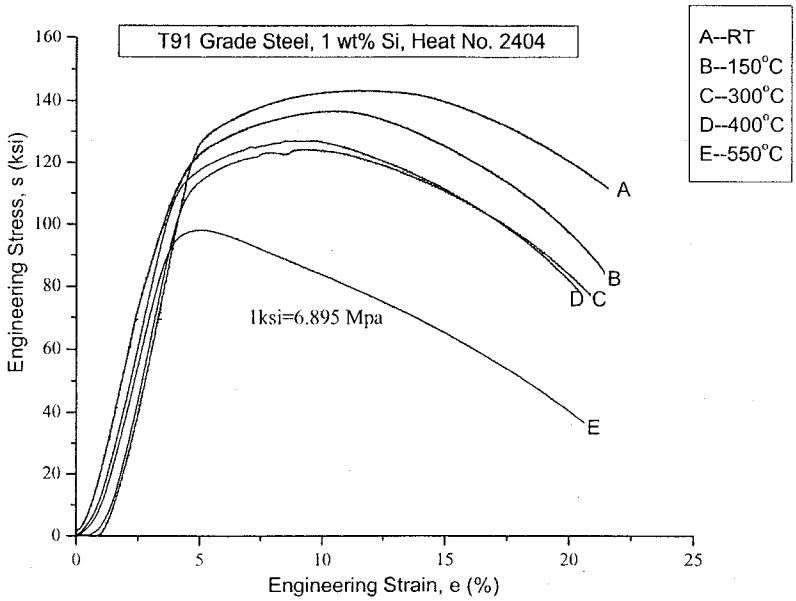

Figure 4-6 s-e Diagram vs. Temperature for 1.0 wt.% Si Steel

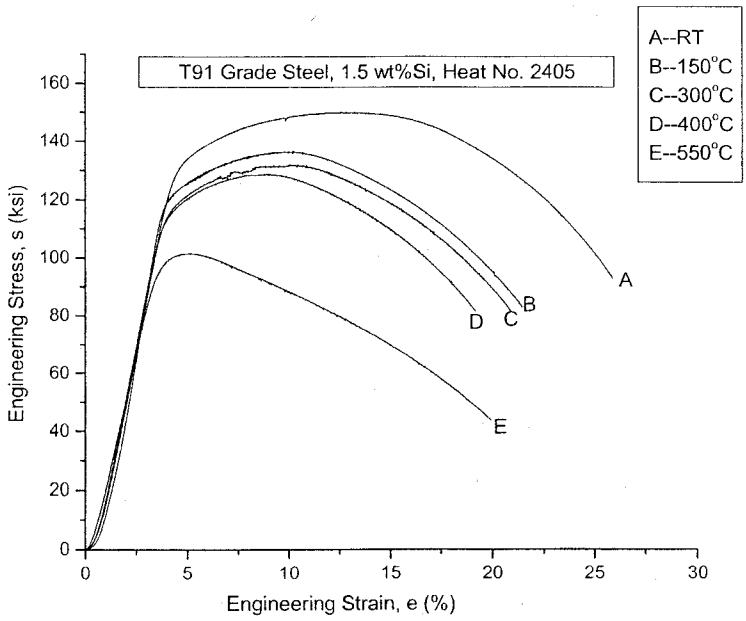

Figure 4-7 s-e Diagram vs. Temperature for 1.5 wt.% Si Steel

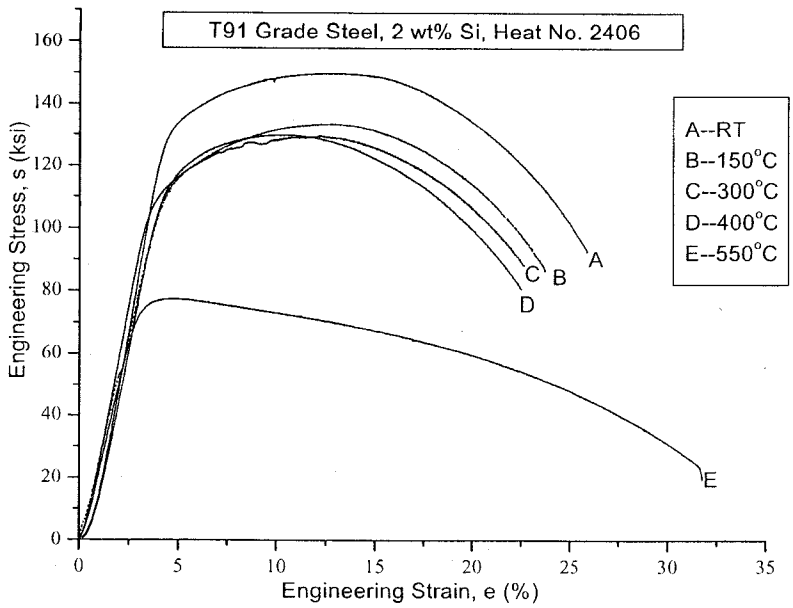

Figure 4-8 s-e Diagram vs. Temperature for 2.0 wt.% Si Steel

The occurrence of gradually-reduced failure strain (e_f) and the formation of serrations, observed in the s-e diagrams resulting from tensile loading within specific temperature regimes, are known [33-40] to be associated with an interesting metallurgical phenomenon, known as dynamic strain ageing (DSA). Since DSA is a thermally-activated process, the diffusion of solute elements within these temperature regimes can play an important role. For instance, the diffusion of either solute or solvent elements into the matrix of metallic materials and alloys during their tensile deformation at a susceptible temperature can hinder the movement of dislocations. The generation of dislocations under tensile loading is a general consequence of plastic deformation, which are often classified as linear defects in metallic materials. However, these defects have to undergo movements through different grains as well as the grain boundaries for plastic deformation to continue until failure occurs.

Since diffusion is a thermally-activated process, the precipitates will continue growing larger until they reach a critical size at a specific temperature, beyond which these precipitates will undergo dissolution into the metal-matrix due to their enhanced solubility at higher temperatures. The formation of critically-sized precipitate particles can impede the movement of dislocations in and around the metallic grains and their boundaries. Beyond this critical temperature, the plasticity of a metal can be enhanced due to reduced resistance to dislocation motion past the grain boundaries, causing enhanced failure strain. Such an explanation can justify the resultant minimum e_f value at 400°C, irrespective of the Si content. The relatively higher e_f value at 550°C can also be rationalized in a similar manner.

In addition to the deformation temperatures, the strain rates used during tensile deformation can influence the movement of dislocations in materials susceptible to the DSA phenomenon. Thus, in order to better understand the deformation mechanism of martensitic alloys tested in this investigation that exhibited both reduced e_f values and serrations within specific temperature regimes, an evaluation of the driving force for such incidences is also warranted. Metallurgically speaking, this driving force is commonly expressed as the activation energy (Q), which is influenced by both temperature and strain rate. Additionally, the ease of plastic deformation under tensile loading is often characterized by the work-hardening index (n) of the tested material. In view of these rationales, significant efforts have been made in this investigation to determine the magnitudes of dislocation density (ρ), Q and n as functions of different metallurgical variables that are subsequently presented in several sub-sections of this chapter.

The different tensile properties including YS, UTS, %El and %RA, determined from the s-e diagrams and the specimen dimensions, before and after testing, are given in Table 4-1. The variations of YS and UTS with temperature are illustrated in Figures 4-9 and 4-10 as a function of Si content. A cursory examination of the data, shown in Figure 4-9, reveals that the magnitude of YS was gradually reduced with increasing temperature, showing an insignificant variation in its value due to the difference in Si content (0.5 and 1.0 wt%). However, there were significant drops in the YS value for steels containing 1.5 and 2.0 wt.% Si at temperatures of 400 and 550°C. As to the UTS values, even though a gradual drop was observed at temperatures up to 400°C, a drastic drop in its value was observed at 550°C, irrespective of the Si content. Nevertheless, the extent of reduction in UTS was more pronounced with steels containing 1.5 and 2.0 wt.% Si.

Table 4-1 Tensile Properties at Different Temperatures

Heat no./Si Content	Testing Temp. (°C)	UTS (ksi)	YS (ksi)	%El	%RA
2403 (0.5%)	RT	147	127	23	67.4
	150	134	118	20.8	65.2
	300	130	113	20	64
	400	125	107	18.2	62.1
	550	102	94	21.5	81.8
2404 (1.0%)	RT	143	125	21	65.7
	150	134	118	21	66.1
	300	127	107	20	66.4
	400	124	105	21	66.1
	550	98	94	21	67.6
2405 (1.5%)	RT	148	131	24	68.1
	150	136	118	22.9	67.4
	300	131	113	21.2	66.7
	400	125	107	20.3	65.2
	550	83	78	26.4	79
2406 (2.0%)	RT	149	131	26	76.2
	150	133	119	24	72.8
	300	130	107	23	71.5
	400	129	92	22	71.7
	550	77	70	32	83

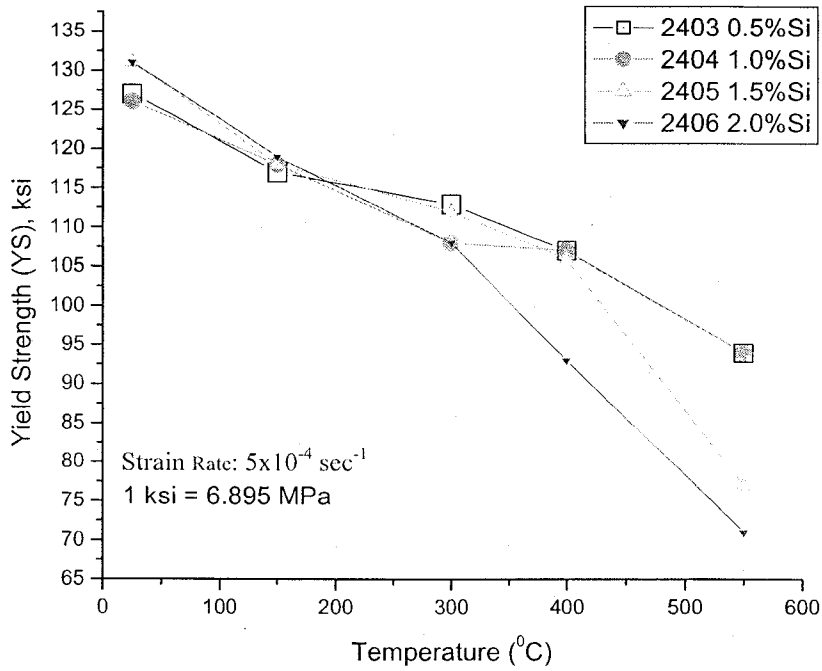

Figure 4-9 YS vs. Temperature

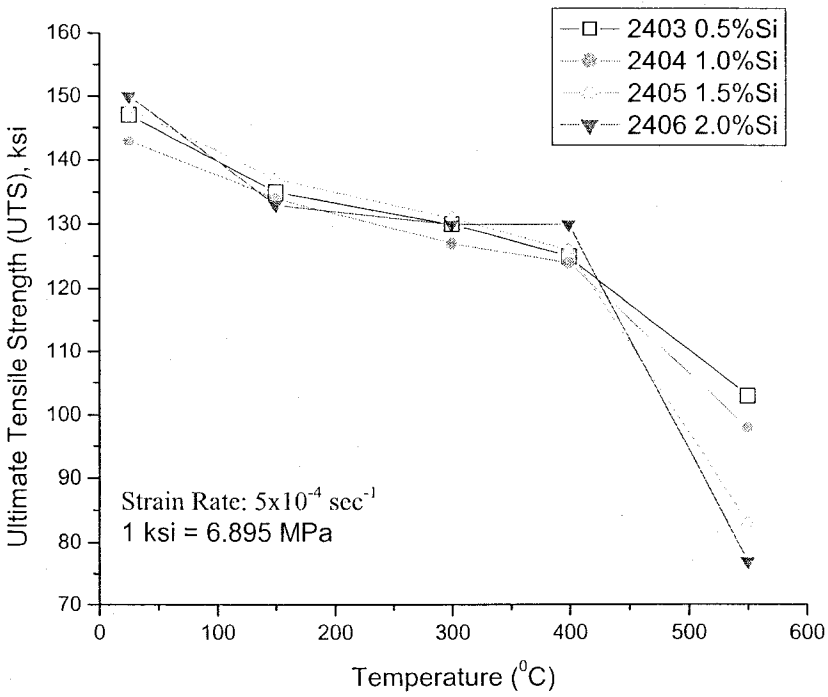

Figure 4-10 UTS vs. Temperature

With respect to the ductility parameters, in general, the magnitudes of %El and %RA were gradually reduced with increasing temperature up to 400°C, followed by their enhancement at 550°C. These data are consistent with the observations made from the superimposed s-e diagrams that exhibited the lowest e_f values at 400°C, irrespective of the Si content, due to the occurrence of DSA phenomenon. The enhanced ductility in terms of %El and %RA at 550°C observed in Figures 4-11 and 4-12, respectively can simply be attributed to increased plastic flow at this temperature, which is also associated with a greater dislocation mobility.

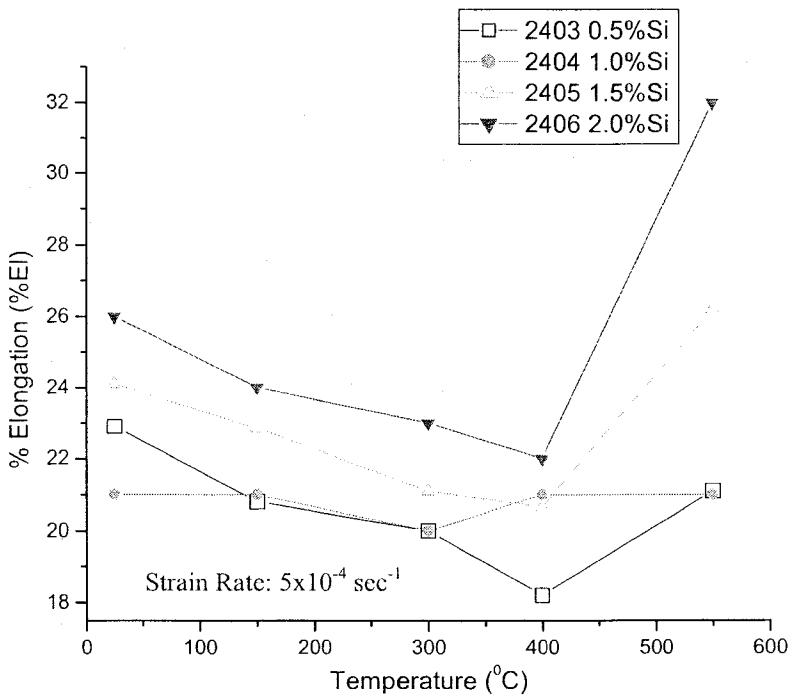

Figure 4-11 %El vs. Temperature

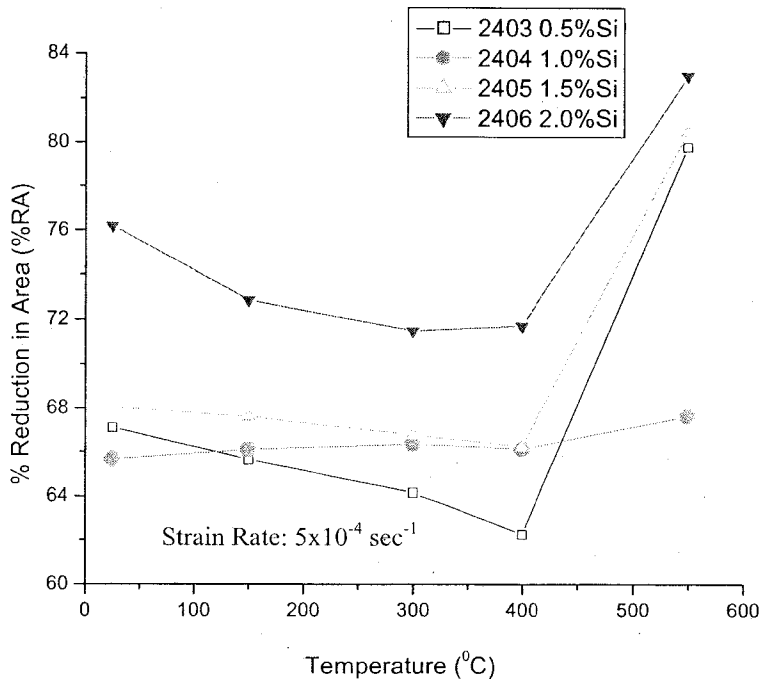

Figure 4-12 %RA vs. Temperature

4.3 Dislocation Density Calculation

Irrespective of the Si content, the magnitude of e_f in the tested tensile specimens of T91 grade steels was minimum at 400°C, as illustrated in Figures 4-5 through 4-8. As explained earlier, the reduced e_f value is the result of impaired dislocation mobility in and around the grain boundaries of these alloys. Thus, it was essential to calculate the dislocation density (ρ) in all tested specimens as a function of temperature at a specific strain rate of $5x10^{-4}$ sec^{-1}. The average value of ρ corresponding to each testing temperature, calculated through placement of grids at multiple locations of the respective TEM micrographs, as described in Chapter 3, are given in Table 4-2. An evaluation of these data clearly reveals that the value of ρ was higher at 400°C by an order of magnitude, compared to those at other temperatures.

Table 4-2 Dislocation Density at Different Temperatures

Temperature (°C)	Dislocation Density ($x10^{14}$ m^{-2})			
	0.5% Si	1.0% Si	1.5% Si	2.0% Si
25	2.5	4.2	5.3	3.6
300	5.3	7.5	8.2	8.4
400	27	36	52	58
550	4.8	8.9	3.6	4.2

It should be noted that the concentration of dislocations in the vicinity of grain boundaries was gradually enhanced with an increase in temperature from ambient to 400°C, as illustrated in Figure 4-13, once again, justifying the lowest values of e_f at 400°C. Such minimum values of e_f can be attributed to the enhanced precipitation of solute particles, thus, blocking the dislocation movement. Beyond 400°C, the values of ρ were once again reduced by an order of magnitude irrespective of the Si content. The lower value of ρ at 550°C could be attributed to the coarsening of precipitates, causing smoother dislocation motion beyond the grain boundaries. The variations of ρ with temperature are also illustrated in Figure 4-14, showing a similar pattern.

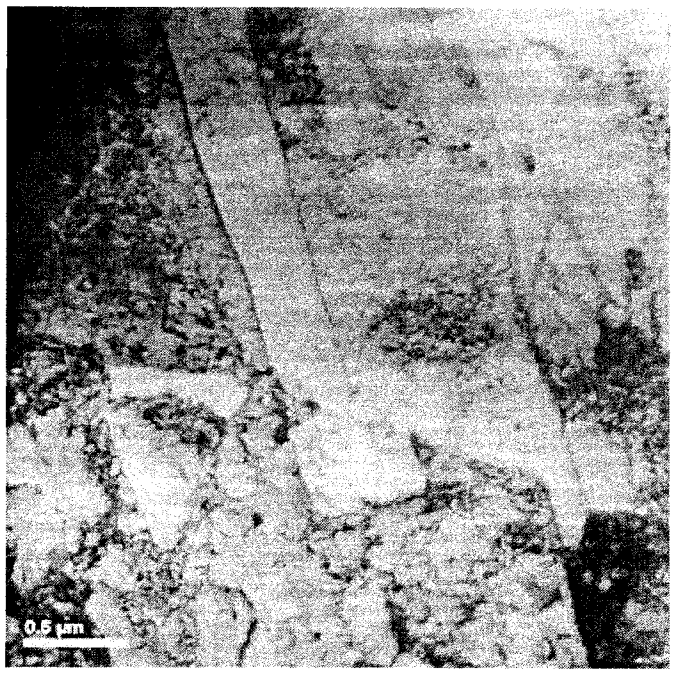

(a) Room Temperature

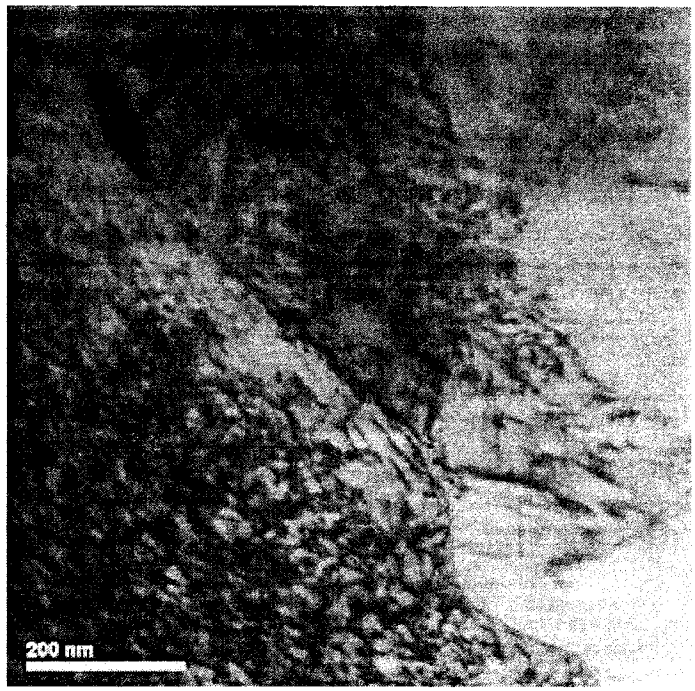

(b) 400°C

Figure 4-13 TEM Micrographs of Steel with 1.5 wt% Si

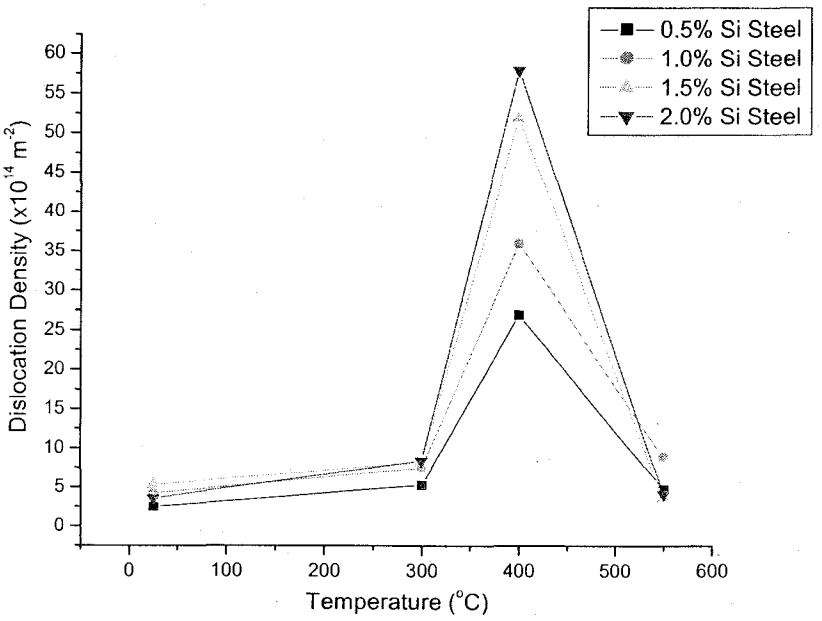

Figure 4-14 Dislocation Density versus Temperature

4.4 Activation Energy Calculation

Smooth cylindrical specimens of T91 grade steels with varied Si content were subjected to tensile loading at temperatures of 200, 300 and 400°C under strain rates of 10^{-2}, 10^{-3} and 10^{-4} sec^{-1}. A combination of different temperature and strain rate was used to develop a basic understanding of the DSA phenomenon based on the activation energy (Q) needed for the onset of serrations in the tested materials. The superimposed s-e diagrams for each heat of T91 grade material at a specific testing temperature corresponding to different strain rates are illustrated in Figures 4-15 through 4-18.

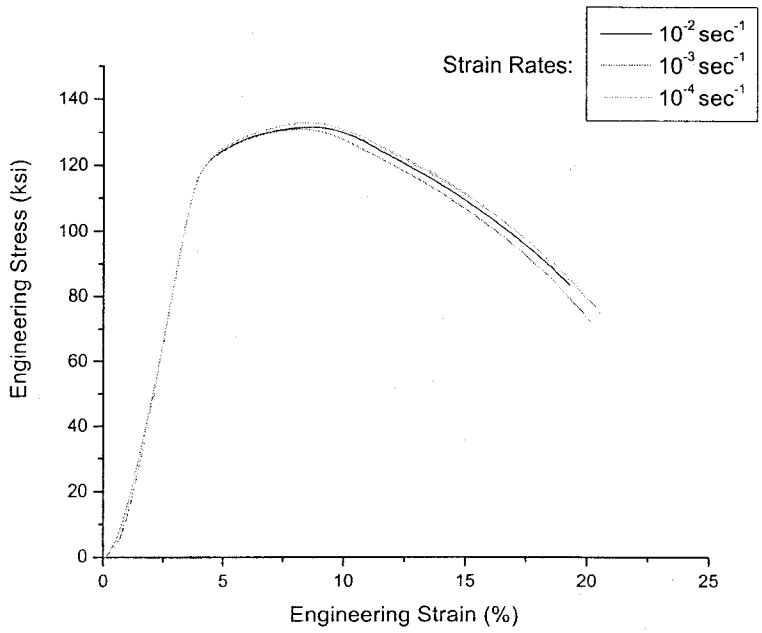

(a) 200°C

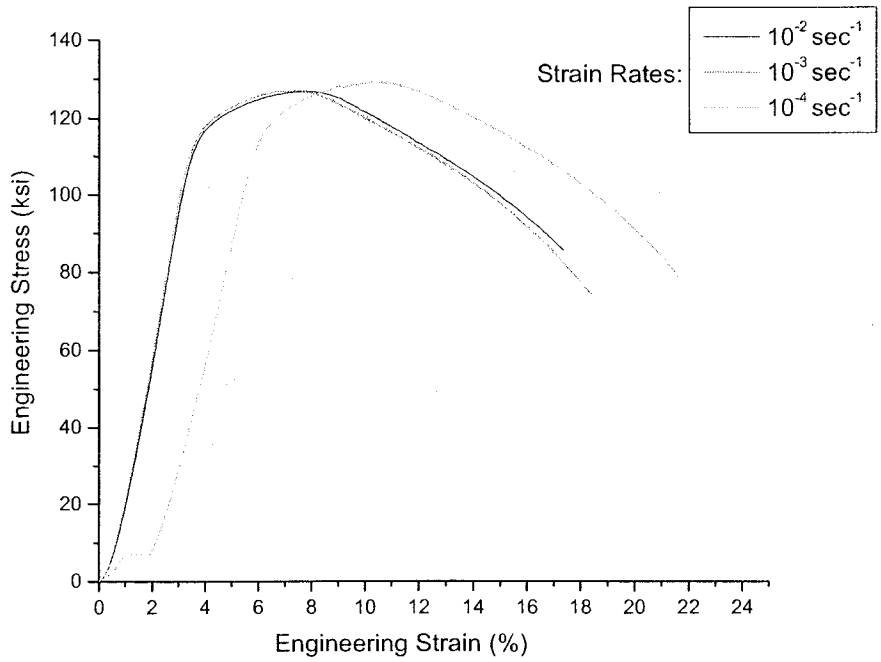

(b) 300°C

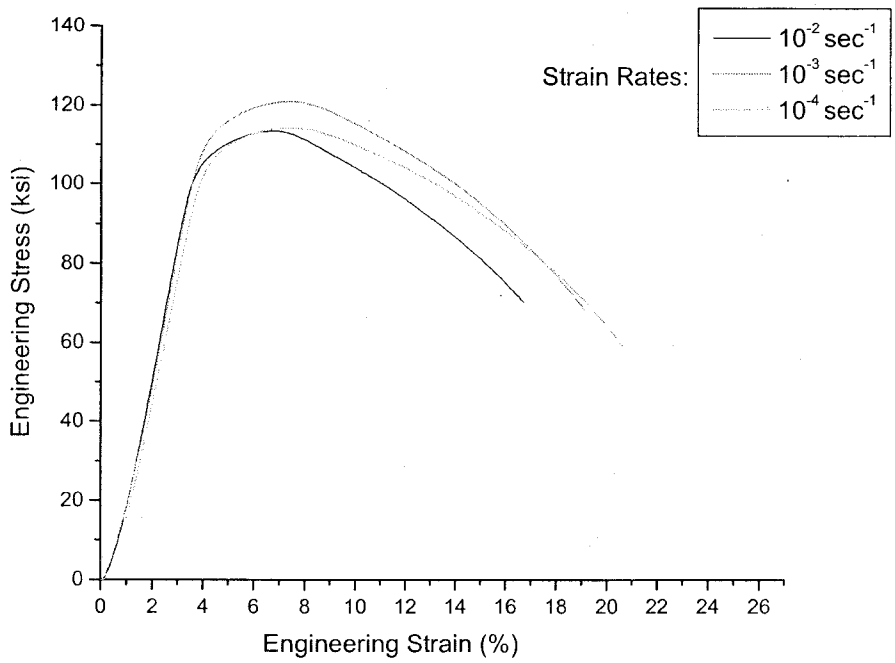

(c) 400°C

Figure 4-15 s-e Diagram vs. Temperature and Strain Rate for Steel with 0.5 wt.% Si

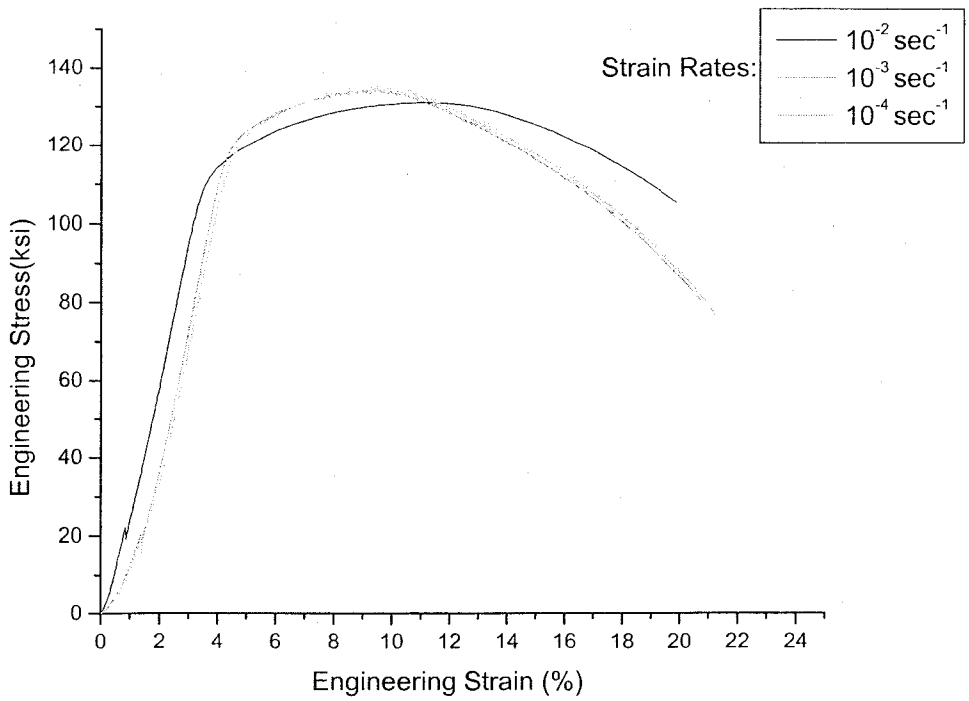

(a) 200°C

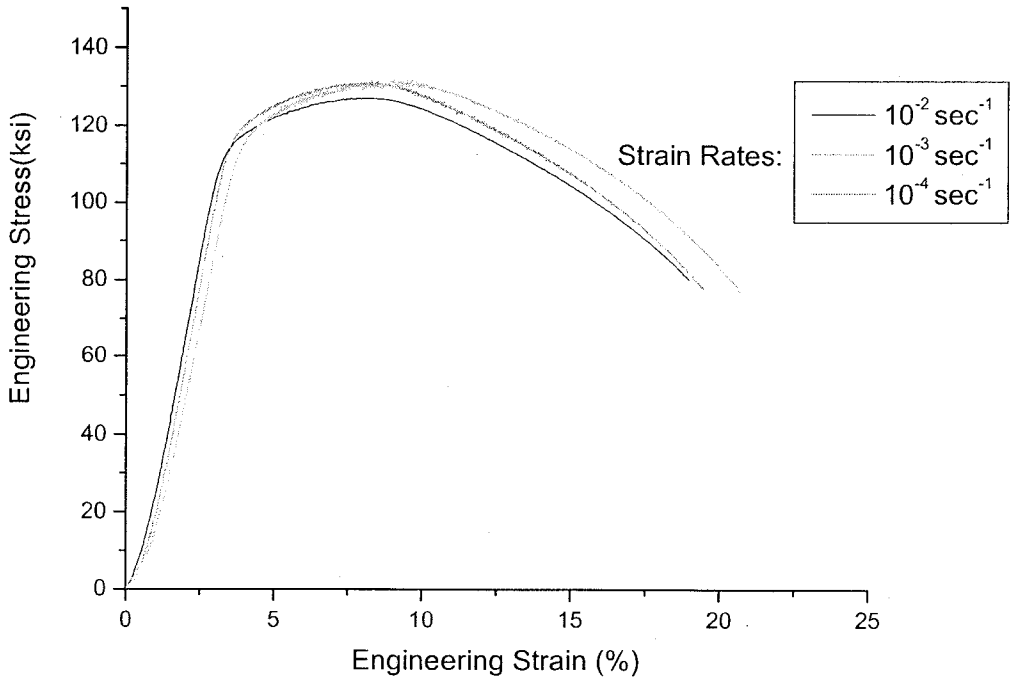

(b) 300°C

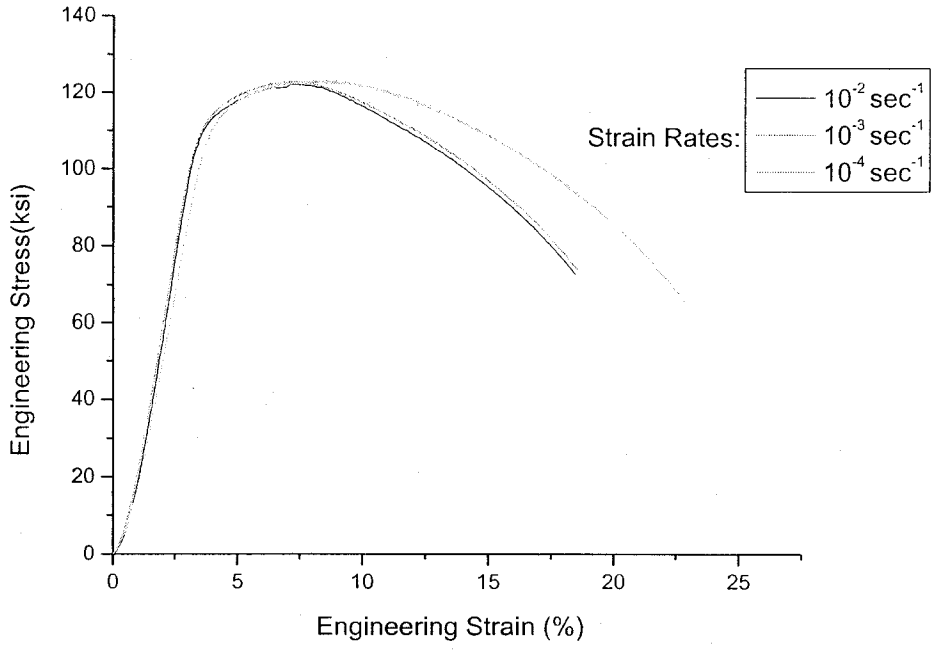

(c) 400°C

Figure 4-16 s-e Diagram vs. Temperature and Strain Rate for Steel with 1 wt.% Si

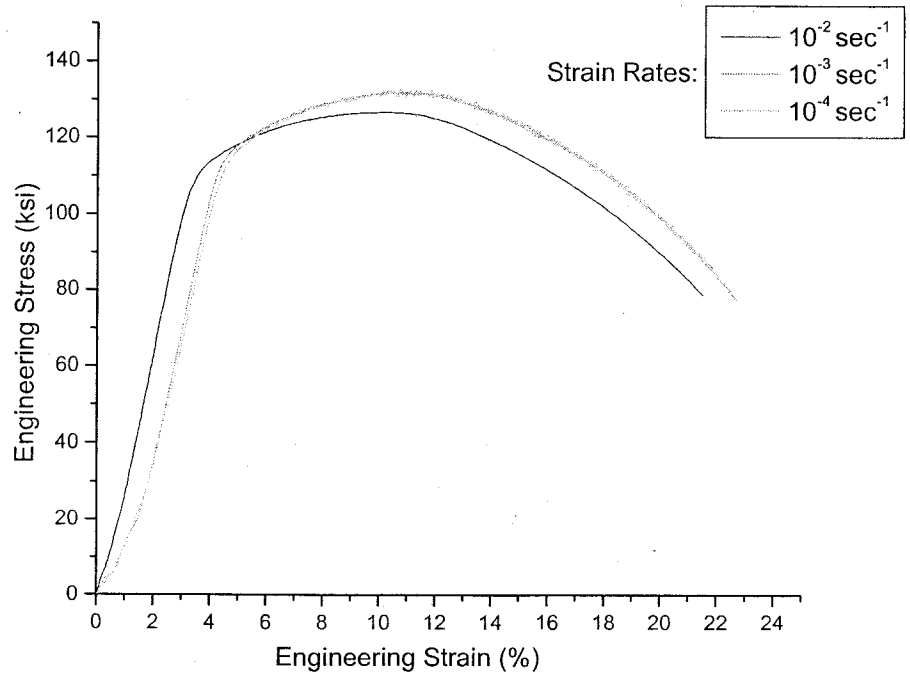

(a) 200°C

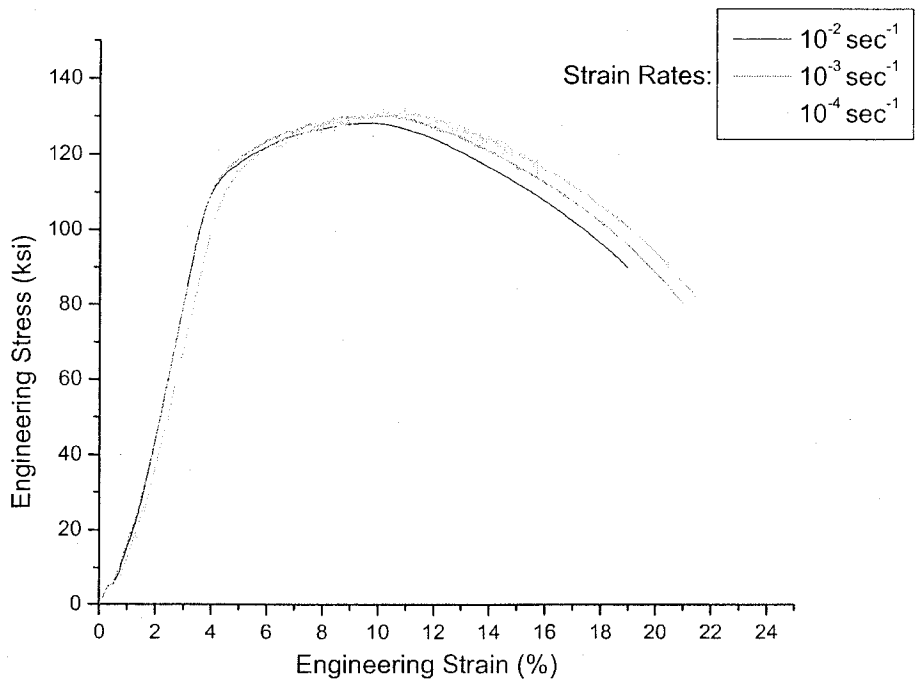

(b) 300°C

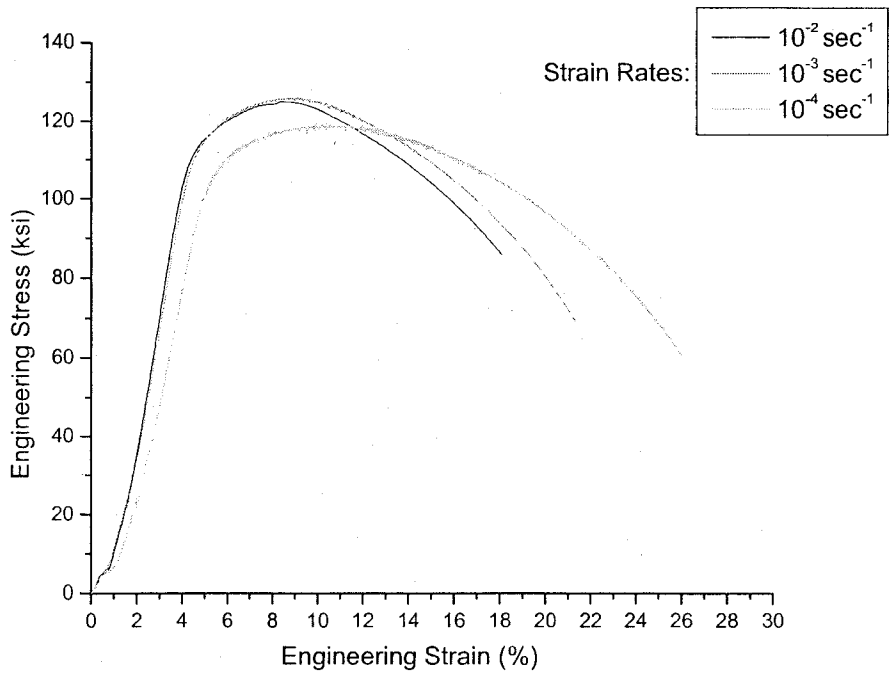

(c) 400°C

Figure 4-17 s-e Diagram vs. Temperature and Strain Rate for Steel with 1.5 wt.% Si

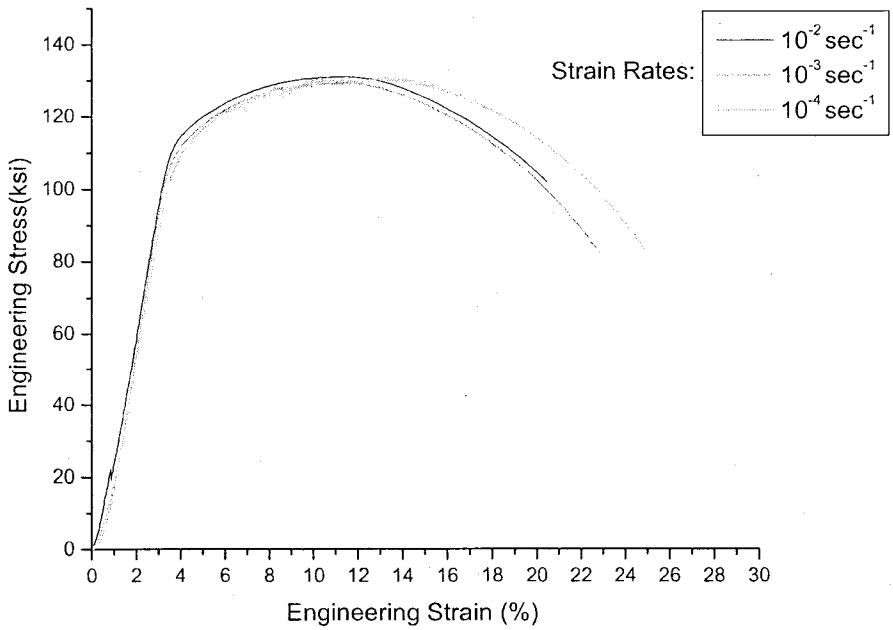

(a) 200°C

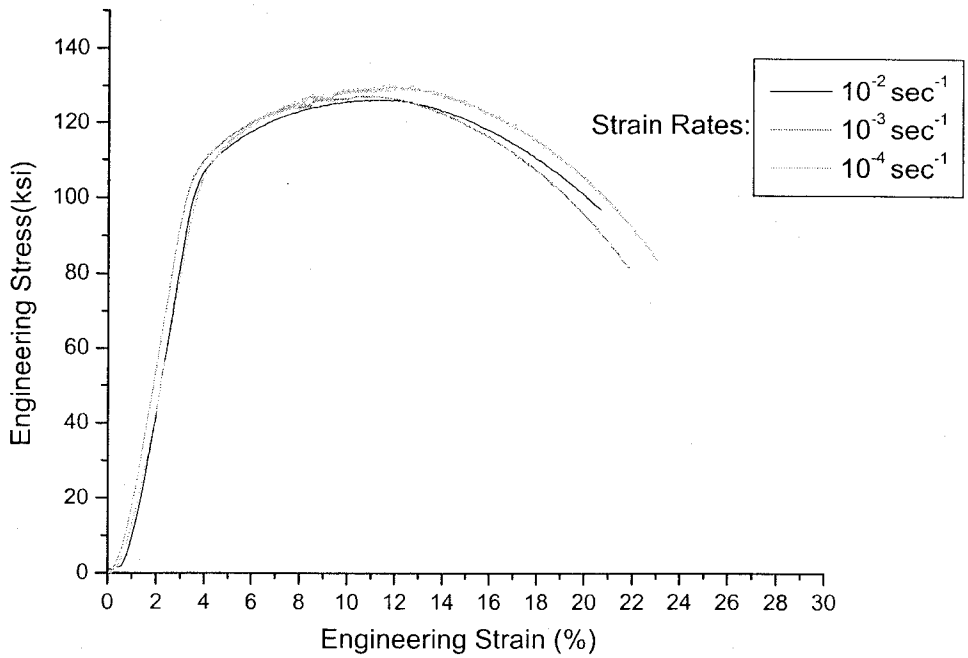

(b) 300°C

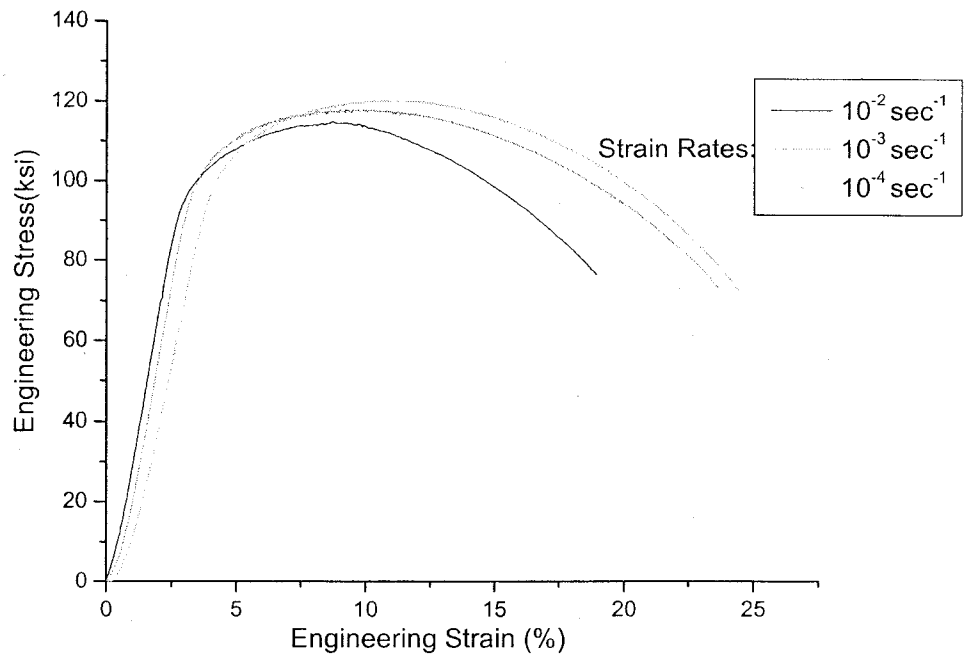

(c) 400°C

Figure 4-18 s-e Diagram vs. Temperature and Strain Rate for Steel with 2 wt.% Si

As indicated in the previous chapter, Equation 3-7 was used to determine the magnitude of Q. $(m+\beta)$ contained in this equation was determined from the plot of $\ln \dot{\varepsilon}$ versus $\ln \varepsilon_c$ corresponding to three tested temperatures and strain rates. $\dot{\varepsilon}$ and ε_c are the strain rate and critical plastic strain, respectively. The variation of $\ln \dot{\varepsilon}$ with $\ln \varepsilon_c$ for all four heats of T91 grade steels are shown in Figures 4-19 through 4-22 as a function of three tested temperatures. The magnitudes of $(m+\beta)$, which represents the slope of the linear portion of these plots for each heat corresponding to different testing temperatures were, thus, determined. Similarly, $\ln \varepsilon_c$ was plotted as a function of the reciprocal of the testing temperature (T) corresponding to each strain rate ($\dot{\varepsilon}$), as shown in Figures 4-23 through 4-26. Once again, a linear relationship was established from these plots, from which the magnitude of the slope $[Q/R(m+\beta)]$ of each line was calculated. By knowing the average value of $(m+\beta)$ from the logarithmic plots of $\ln \dot{\varepsilon}$ vs. $\ln \varepsilon_c$ (Figures 4-19 through 4-22), the magnitude of Q was computed.

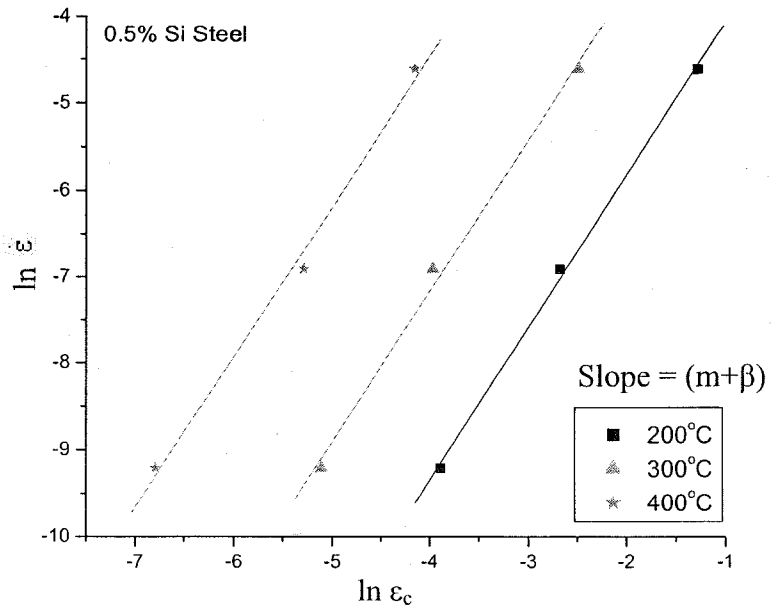

Figure 4-19 $\ln \dot{\varepsilon}$ vs. $\ln \varepsilon_c$ for Steel with 0.5 wt.% Si

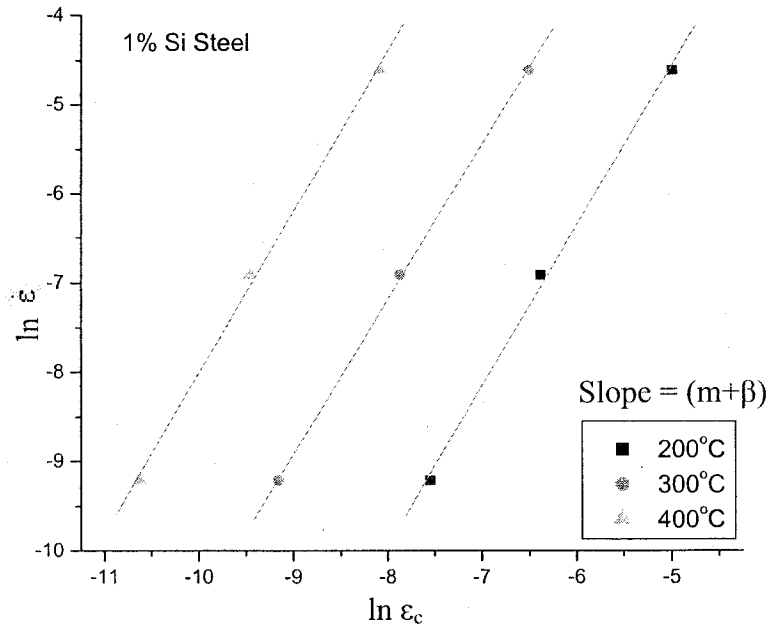

Figure 4-20 $\ln \dot{\varepsilon}$ vs. $\ln \varepsilon_c$ for Steel with 1 wt.% Si

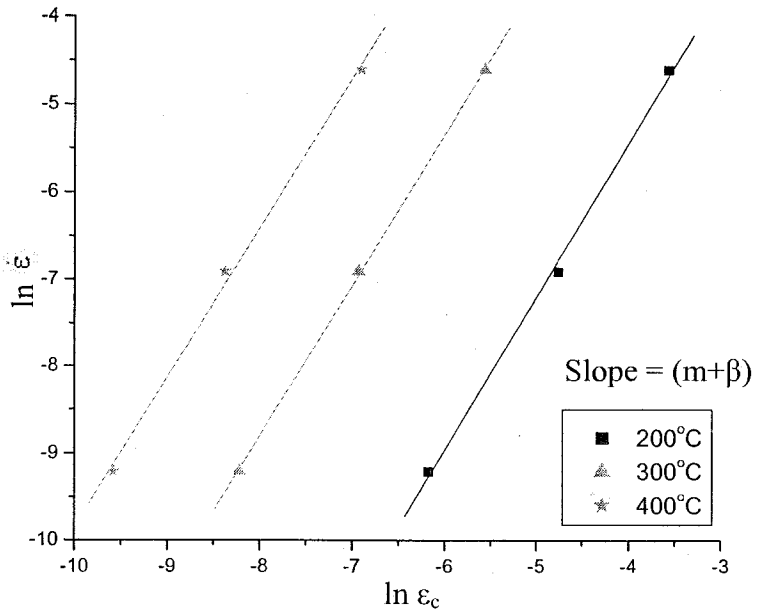

Figure 4-21 $\ln \dot{\varepsilon}$ vs. $\ln \varepsilon_c$ for Steel with 1.5 wt.% Si

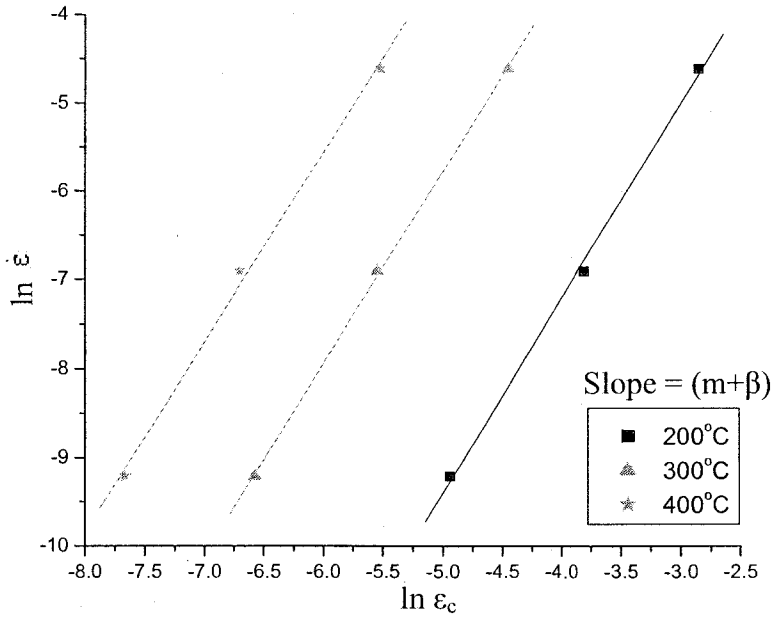

Figure 4-22 $\ln \dot{\varepsilon}$ vs. $\ln \varepsilon_c$ for Steel with 2 wt.% Si

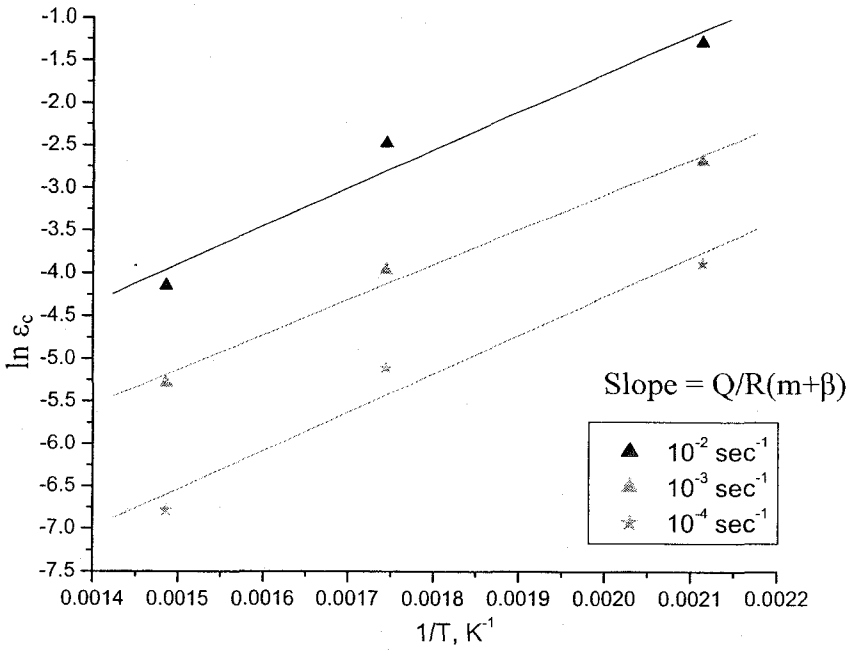

Figure 4-23 ln ε_c vs. 1/T for Steel with 0.5 wt.% Si

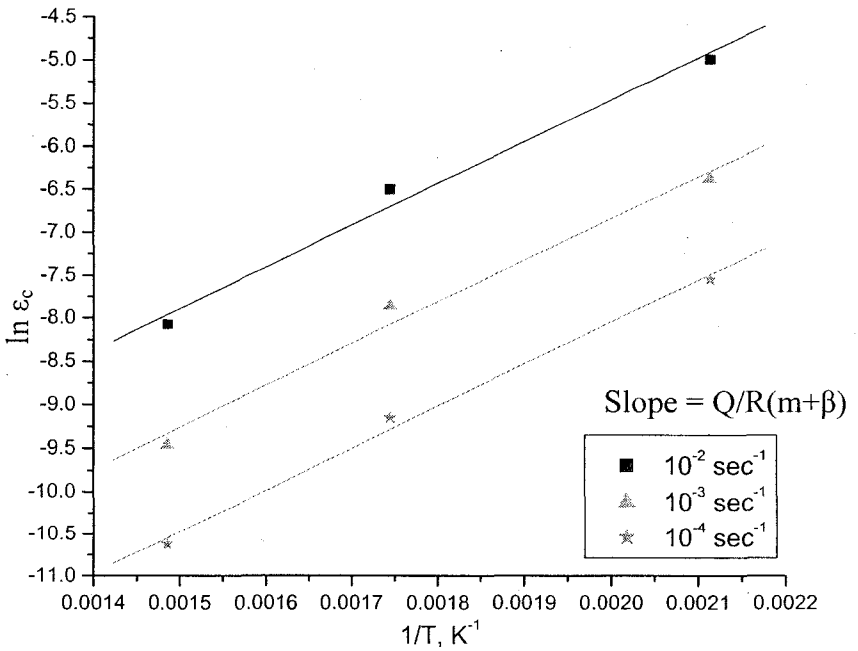

Figure 4-24 ln ε_c vs. 1/T for Steel with 1 wt.% Si

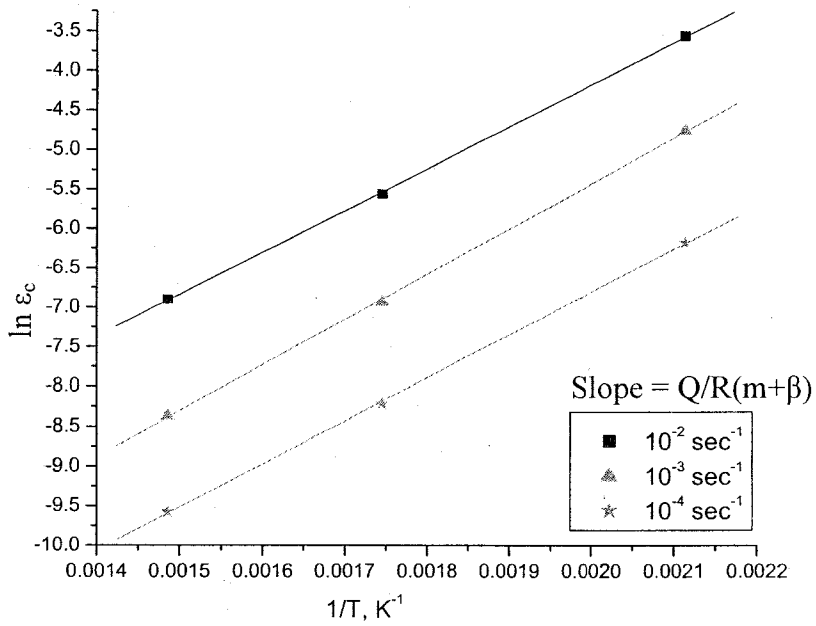

Figure 4-25 ln ε_c vs. 1/T for Steel with 1.5 wt.% Si

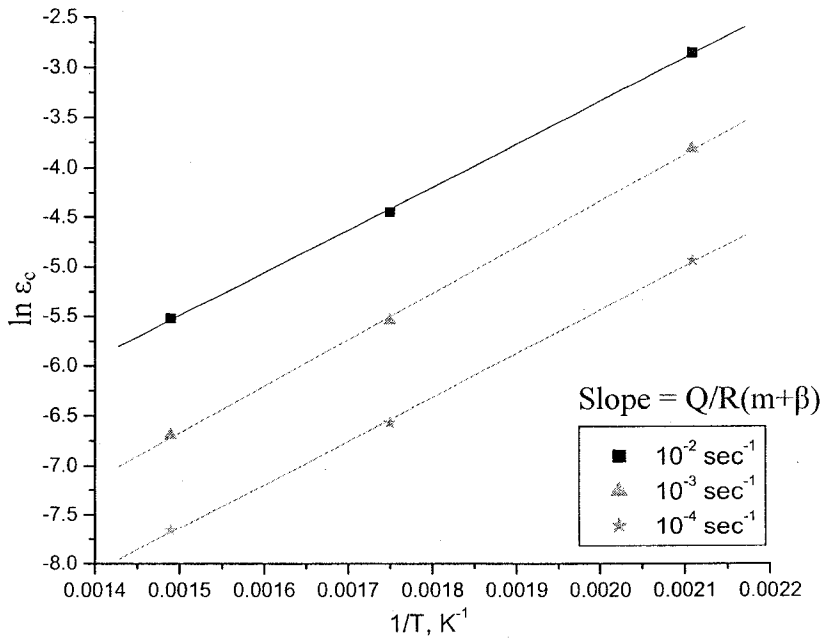

Figure 4-26 ln ε_c vs. 1/T for Steel with 2 wt.% Si

The average values of (m+β) and Q corresponding to three temperatures of 200, 300 and 400°C are given in Tables 4-3 through 4-6 for all four heats of the tested materials. An evaluation of the data, shown in these tables, reveals that the average value of (m+β) was not influenced by the variation of Si content from 0.5 to 1.5 wt.% Si. In essence, the magnitude of (m+β) ranged between 1.73 and 1.78 for these three steels. However, a relatively higher average value of (m+β) was determined for T91 grade steel containing 2 wt.% Si. It is interesting to note that the average activation energy based on these (m+β) values for the T91 grade steel was gradually increased with increasing Si content from 0.5 to 2.0 wt.%. No systematic correlationship of Q with (m+β) can be established based on the resultant data. The effect of Si content on Q has not yet been investigated by any other researchers. Thus, the Q values calculated in this investigation could not be compared to any literature data.

Table 4-3 (m+β) and Q values for Steel with 0.5 wt.% Si

Strain Rate, sec^{-1}		Temperature (°C)			Average Q, KJ/mol	Net (m+β)	Net Q, KJ/mol
		200	300	400			
10^{-2}	Average* (m+β)	1.76	1.74	1.73	N/A	1.74	N/A
10^{-3}							
10^{-4}							
10^{-2}	Average* Q, kJ/mole	65.6	64.9	64.5	66	N/A	64.4
10^{-3}		60.1	59.5	59.13	60.4		
10^{-4}		66.4	65.6	65.3	66.7		

* Average of duplicate testing

Table 4-4 (m+β) and Q values for Steel with 1.0 wt.% Si

Strain Rate, sec^{-1}		Temperature (°C)			Average Q, KJ/mol	Net (m+β)	Net Q, KJ/mol
		200	300	400			
10^{-2}	Average* (m+β)	1.79	1.73	1.80	N/A	1.78	N/A
10^{-3}							
10^{-4}							
10^{-2}	Average* Q, kJ/mole	72.6	70.3	73	72	N/A	71.8
10^{-3}		72.2	70	72.6	71.7		
10^{-4}		72.5	70.26	72.9	71.9		

* Average of duplicate testing

Table 4-5 (m+β) and Q values for Steel with 1.5 wt.% Si

Strain Rate, sec^{-1}		Temperature (°C)			Average Q, KJ/mol	Net (m+β)	Net Q, KJ/mol
		200	300	400			
10^{-2}	Average* (m+β)	1.75	1.73	1.71	N/A	1.73	N/A
10^{-3}							
10^{-4}							
10^{-2}	Average* Q, kJ/mole	77.8	76.68	75.8	76.6	N/A	79.2
10^{-3}		84.2	82	82	82.9		
10^{-4}		79.4	78.2	77.3	78.1		

* Average of duplicate testing

Table 4-6 (m+β) and Q values for Steel with 2.0 wt.% Si

Strain Rate, sec^{-1}		Temperature (°C)			Average Q, KJ/mol	Net (m+β)	Net Q, KJ/mol
		200	300	400			
10^{-2}	Average* (m+β)	2.19	2.16	2.14	N/A	2.16	N/A
10^{-3}							
10^{-4}							
10^{-2}	Average* Q, kJ/mole	78.9	77.8	76.7	77.5	N/A	80.2
10^{-3}		85.3	84.1	83.2	84		
10^{-4}		80.5	79.3	78.4	79.1		

* Average of duplicate testing

4.5 Strain Hardening Exponent Calculation

The magnitudes of strain hardening exponent (n), as a function of the testing temperature, were calculated by converting engineering stress and engineering strain into true stress and true strain, and plotting them on a log-log scale, as shown by Equation 3-13 given in Chapter 3. n in this equation simply represents the slope of the resultant straight line. From a fundamental point of view, n signifies the ease of plastic deformation beyond elasticity at a specific strain rate. The average values of n, calculated by this method, are given in Table 4-7 as functions of temperature and Si content. Several observations can be made from the calculated values of n, given in this table.

Table 4-7 n versus Temperature

Si Content, wt.%	n				
	Temperature (°C)				
	RT	150	300	400	550
0.5	0.16	0.17	0.18	0.1984	0.14
1.0	0.17	0.18	0.19	0.2143	0.16
1.5	0.16	0.17	0.18	0.1802	0.16
2.0	0.17	0.17	0.18	0.1997	0.10

A major observation was that the magnitude of n was gradually enhanced with an increase in temperature from ambient to 400°C, irrespective of the Si content. Secondly, at a specific temperature, the magnitude of n was not significantly influenced by the variation in Si content. As to the first observation, a gradual enhancement in n value can be attributed to the greater diffusivity of solute elements at higher temperatures, thus, causing enhanced precipitation in the vicinity of the grain boundaries. Obviously, larger driving forces have to be applied to cause movement of dislocations that were surrounded by these precipitates. Interestingly, a similar rationalization has been given earlier to explain the minimum e_f values observed in the superimposed s-e diagrams at 400°C. Thus, it can be construed that the greater driving forces needed to enhance dislocation motion are synonymous with the resultant increase in work-hardening of the tested materials at temperatures ranging from ambient to 400°C. Accordingly, a gradual increase in n value was observed with increasing temperature (up to 400°C) irrespective of the Si content.

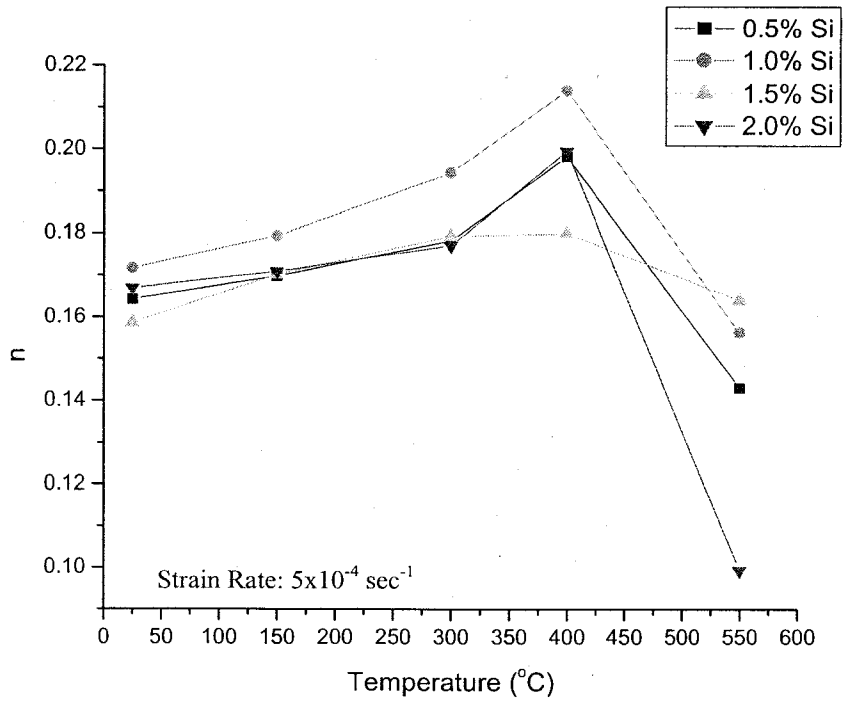

Figure 4-27 n vs. Temperature

The variation of n with temperature is illustrated in Figure 4-27, showing a drastic drop in n value at 550°C. These results are consistent in that a greater ductility in terms of %El and %RA was also observed at this temperature due to enhanced plastic flow, as shown in Figures 4-11 and 4-12. As indicated earlier, the phenomenon of DSA can be significantly influenced by both temperature and strain rate. Therefore, in order to better understand the concept of DSA associated with the martensitic T91 grade steels of varied Si content, extensive efforts were made to correlate plasticity in terms of %El at three selected temperatures of 200, 300 and 400°C using strain rates that were either faster or slower relative to the initial strain rate of $5x10^{-4}$ sec^{-1} used in tensile testing. The variations of %El with strain rate at 200, 300 and 400°C are illustrated in Figures 4-28, 4-29 and 4-30, respectively on a semi-logarithmic plot for all four tested materials.

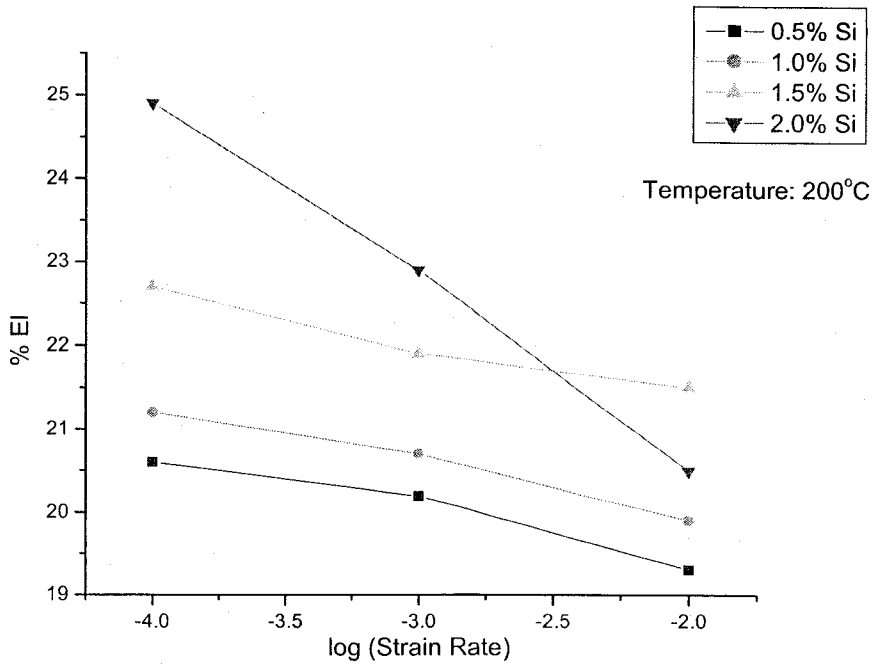

Figure 4-28 %El vs. Strain Rate at 200°C

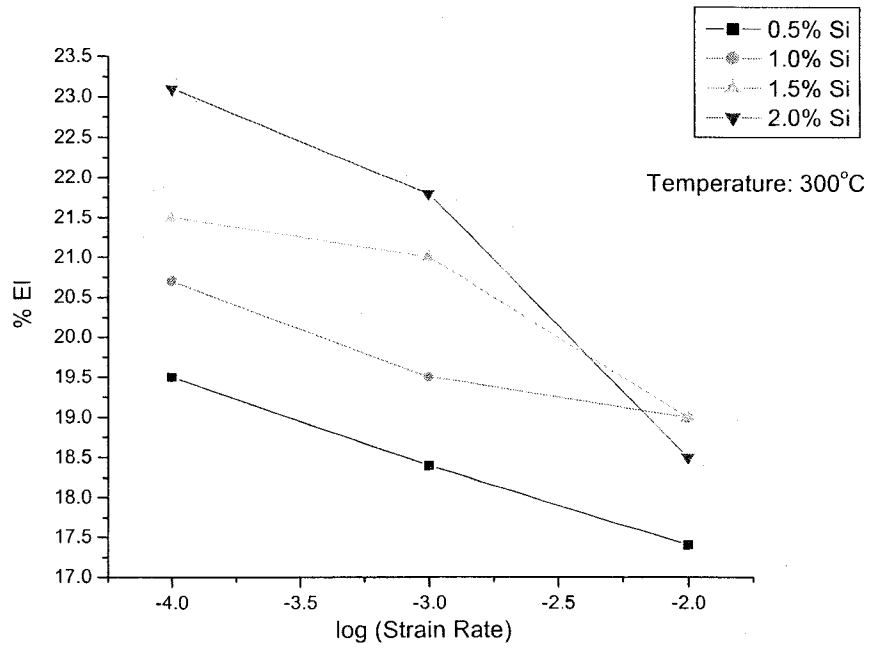

Figure 4-29 %El vs. Strain Rate

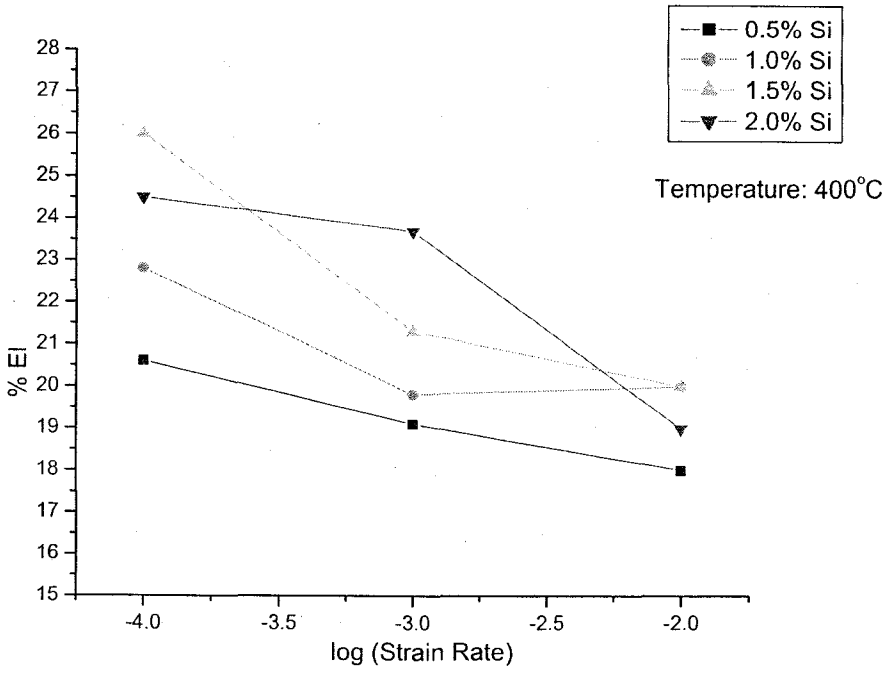

Figure 4-30 %El vs. Strain Rate

Several interesting observations can be made from Figures 4-28 through 4-30, elucidating the effect of Si content on the resultant ductility as a function of strain rate at a specific testing temperature. First of all, the ductility in terms of %El was gradually reduced with faster strain rate with faster strain rate, irrespective of the Si content in the tested materials. At 200 and 300°C, steels containing gradually increased Si content exhibited higher ductility at strain rates of 10^{-4} and 10^{-3} sec^{-1}. However, at the fastest strain rate (10^{-2} sec^{-1}), steel containing 2 wt.% Si showed relatively lower %El values compared to those with steel containing 1.5 wt.% Si at both temperatures. Thus, it appears that at this strain rate, the presence of 2 wt.% Si may be detrimental from the ductility point of view at these two temperatures. At a strain rate of 10^{-2} sec^{-1}, T91 grade steels of varied Si content experienced the least failure times, leading to reduced plastic

deformation independent of these two testing temperatures. At 400°C, the variation of %El with strain rate was erratic in nature, as illustrated in Figure 4-30, showing an inconsistent pattern on the effect of Si content on this ductility parameter. It should, however, be noted that the occurrence of DSA was most pronounced at 400°C, showing the least ductility in terms of e_f. Thus the erratic behavior on the variation of %El with strain rate at this temperature could be the result of multiple interactions among variables including plasticity, deformation time, and Si content.

4.6 Results of Charpy Testing

T91 grade steels are known to possess superior tensile strength even at elevated temperatures primarily due to the presence of niobium and vanadium, and development of fine tempered martensitic microstructure. This investigation was focused on the determination of the role of Si content on the resultant metallurgical properties. As discussed in the previous section, one way of evaluating the effect of Si content on the metallurgical behavior of the tested materials is to determine their susceptibility to rupture under impact loading that can simulate an unusually high strain rate during plastic deformation. The two important metallurgical parameters that can be evaluated by impact testing are the energy absorbed (ft-lb) and the ductile-brittle-transition-temperature (DBTT) of T91 steels as a function of Si content.

The variations of impact energy as a function of the testing temperature are given in Table 4-8. Conventionally, impact testing is performed over a range of temperature varying from cryogenic to elevated temperatures. Therefore, T91 grade steels of varied Si content were subjected to impact loading at temperatures of -40, 25, 75, 125, 230, 340

and 440°C. Plots of impact energy versus temperature are illustrated in Figure 4-31 as a function of the Si content. The resultant data reveal that the energy absorbed in fracturing the V-notched Charpy (CVN) specimens were substantially lower at temperatures of -40, 25 and 75°C, as expected due to reduced ductility at relatively lower temperatures. On the contrary, the impact energy was gradually enhanced with an increase in temperature up to 340°C, followed by the formation of a plateau at 440°C. Such type of S-shaped impact energy versus temperature curve is a general consequence for a majority of engineering metals and alloys indicating the presence of brittle and ductile regions. The portions of these curves showing lower and upper plateau are commonly termed as the brittle versus ductile impact energy curve. The portion of this curve lying in between these two plateaus signifies a transition from brittle-to-ductile mode of failure. The temperature at which such transition occurs is commonly termed as DBTT. The magnitude of DBTT was determined by taking an average value of the impact energy lying between the upper and lower shelf energies, and extrapolating this energy to the temperature axis.

Table 4-8 Results of Charpy Testing

Si Content, wt.%	Temperature, °C Impact Energy, ft-lb							DBTT,° C
	-40	25	75	125	230	340	440	
0.5	15	19	27	48	59	62	63	90
1.0	8.5	13	18	38	47.5	49	49	95
1.5	4.5	8	12.5	19	31	38	39	140
2.0	3	6	8	13	23	28	30.5	150

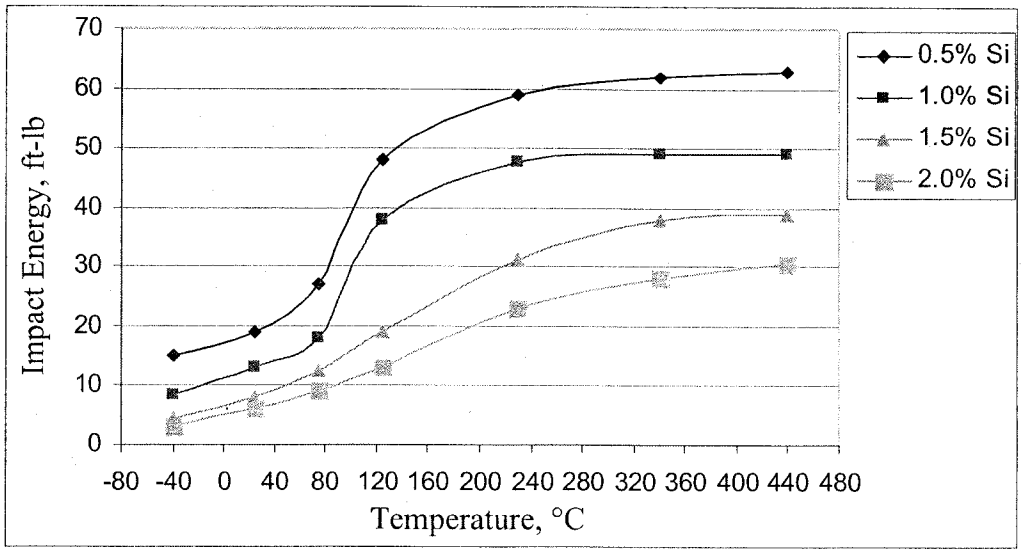

Figure 4-31 Impact Energy vs. Temperature

The magnitudes of DBTT corresponding to different levels of Si content in T91 grade steels are also given in Table 4.8. The variation of DBTT with Si content is illustrated in Figure 4-32, showing a gradual increase in DBTT with increasing Si content. A higher DBTT value signifies a relatively reduced impact resistance showing greater impact energy. Thus, it is obvious that the tested materials with a higher Si content would undergo brittle failure more readily than those with lower Si content. From a design point of view, it is preferable for a structural material to possess a DBTT as low as possible. Therefore, these results clearly indicate that the presence of higher Si content in T91 grade steels would be detrimental from the metallurgical performance point of view. Nevertheless, the overall Charpy data conform to the conventional metallurgical understanding of plastic deformation of structural materials at a high strain rate in terms of impact energy DBTT.

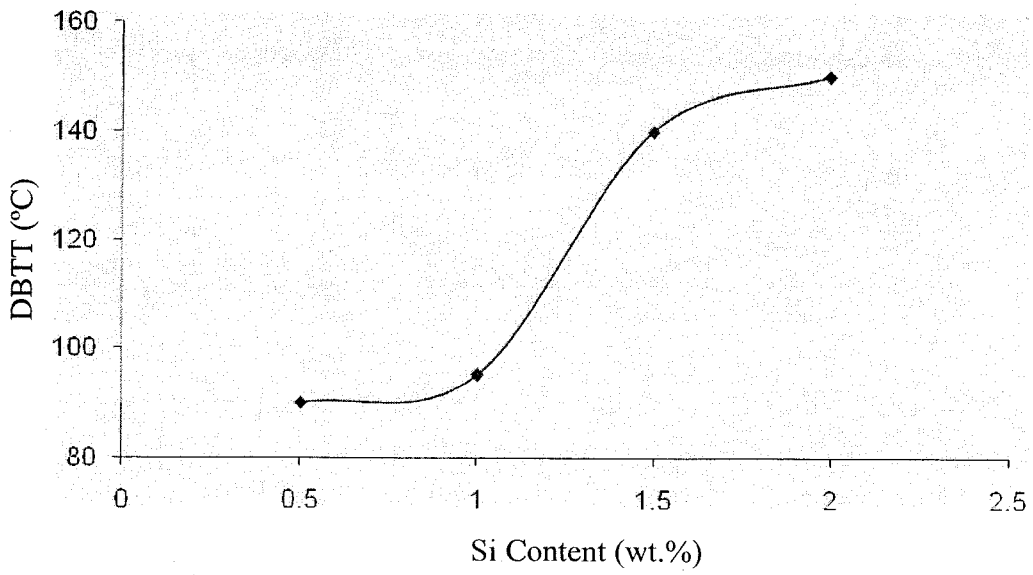

Figure 4-32 DBTT vs. Si Content

4.7 Fracture Toughness Evaluation

The measurements of plane strain fracture toughness (K_{IC}) values were initially performed at room temperature involving compact tension (CT) specimens of T91 grade steels having 0.5, 1.5, and 2 weight percent Si. Later, K_{IC} measurements were also performed at 300°C using CT specimens of similar grades. The load versus displacement (P-υ) curves generated at ambient temperature and 300°C are illustrated are illustrated in Figures 4-33 and 4-34. An examination of these data reveals that for the steels containing 0.5 and 1.5 weight percent Si, P-υ curves generated at ambient temperature were very similar to type III plot shown in Figure 3-4 in the previous chapter. Type III represents a brittle material with limited plasticity. On the contrary, the steel containing 2 weight percent Si showed appreciable plastic region beyond elasticity. At 300°C, P-υ curves resembled that of type I plot, also shown in Figure 3-4. In essence the type I plot

correspond to a ductile material. Thus, it appears that the P-υ curves at 300°C may be the result of enhanced plasticity at an elevated temperature, irrespective of the Si content.

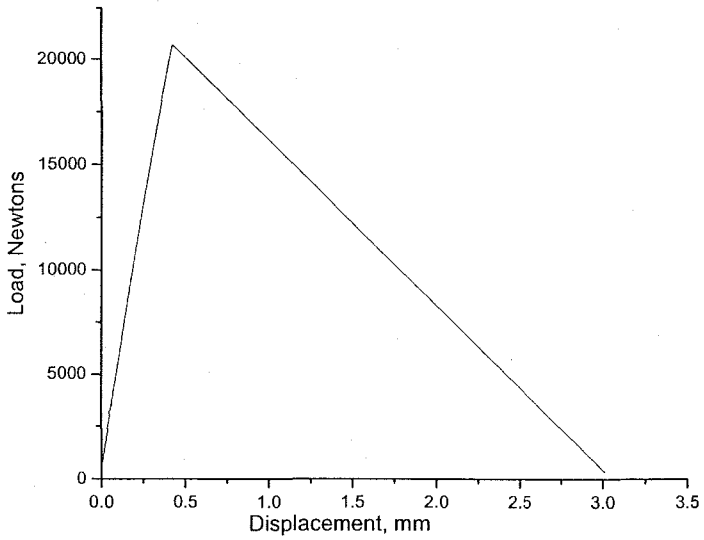

(a) 0.5 wt.% Si

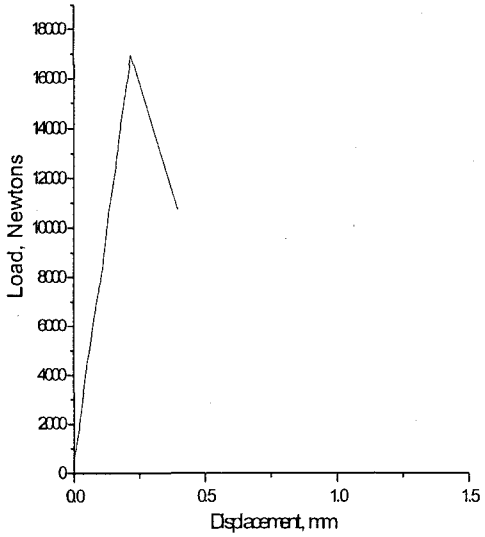

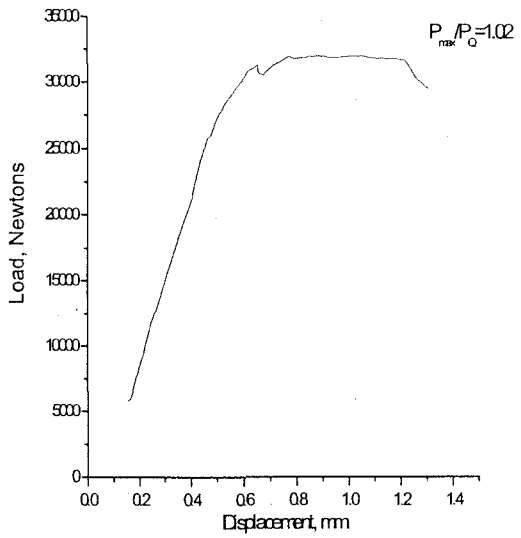

(b) 1.5 wt.% Si

(c) 2.0 wt.% Si

Figure 4-33 P-υ curves of T91 Grade Steels at Ambient Temperature

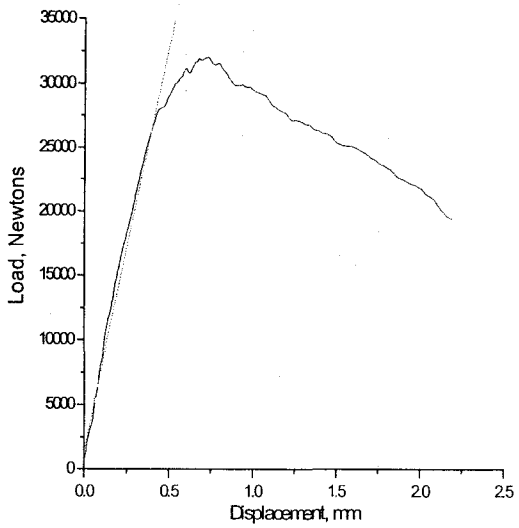

(a) 0.5 wt.% Si

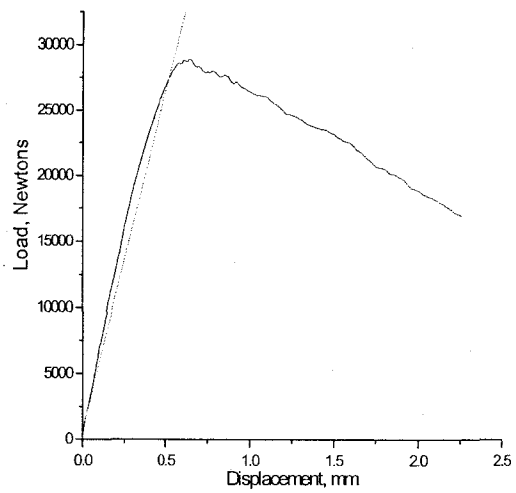

(b) 1.5 wt.% Si

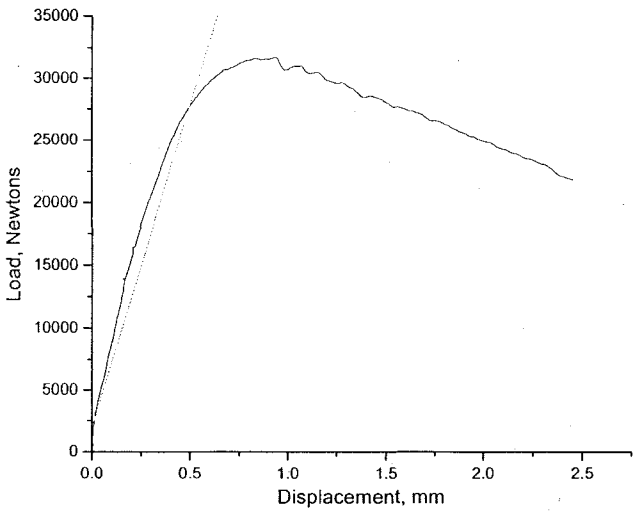

(c) 2.0 wt.% Si

Figure 4-34 P-υ curves of T91 Grade Steels at 300°C

The average values of conditional fracture toughness (K_Q) determined from these experiments are given in Table 4-9 for Si content of 0.5, 1.5 and 2.0 weight percent. It should be noted that the ratio of maximum load to the conditional load (P_{max}/P_Q) was equivalent to 1 for all three grades of steels. Based on the fracture mechanics criteria, K_Q is considered to be identical to K_{1C} from the design point of view. Thus, the resultant data suggest that the magnitude of K_{1C} was substantially higher for the steel containing 0.5 weight percent Si, compared to those of steels with greater Si content (68 versus 51 ksi. $in^{1/2}$). K_{1C} values for martensitic stainless steels of similar chemical composition have been cited [53] to range between 60 and 90 ksi.$in^{1/2}$. Thus, the resultant K_{1C} value for the steel containing 0.5 weight percent falls within this acceptable range. As to the K_{1C} values for the similar grades of steels at 300°C, no valid K_{1C} could be determined since the magnitudes of P_{max}/P_Q ratios were greater than 1.1, which deviates from the acceptable criteria for valid K_{1C}. It should also be noted that a similar detrimental effect of higher Si content was observed in Charpy testing, where gradually reduced impact resistance occurred in terms of both absorbed energy and DBTT with increasing temperature.

Table 4-9 Average K_Q Values for Different Si Containing Steel

Si Content, wt.%	Specimen ID	a_i, mm	f(a/w)	P_{max}, kN	P_{max}/P_Q	Average K_Q	
						MPam$^{1/2}$	ksi.in$^{1/2}$
0.5	1	12.72	9.66	20.7	1	74.7	68
	2	10.88	7.84	21.9	1		
1.5	1	10.96	7.91	16.96	1	56.4	51.3
	2	11.50	8.40	15.2	1		
2.0	1	10.8	7.77	25.78	1.02	56.30	51.2
	2	11.22	8.14	N/A	N/A		

4.8 Fractographic Evaluations

The morphologies of failure at the primary fracture surface of the tested cylindrical specimens under tensile loading, analyzed by SEM, are illustrated in Figures 4-35 through 4-38. An examination of these micrographs clearly reveals that steels containing 0.5, 1.0, and 1.5 wt.% Si suffered from brittle failures at temperatures ranging from ambient to 300°C. A combination of intergranular and cleavage failure was observed at room temperature for all three alloys. However, at 150 and 300°C, the failures were characterized by intergranular cracking and dimples. As to the fracture morphologies at 550°C, all three alloys exhibited dimpled microstructures indicating ductile failures, the size of dimples gradually becoming larger with the higher Si content. Except at room temperature and 150°C, the steel containing 2 wt.% Si exhibited predominantly dimpled microstructures with a greater concentration of micro-voids at higher temperatures. This observation is consistent with the tensile data of 2 wt.% Si- containing steels, presented in the previous section.

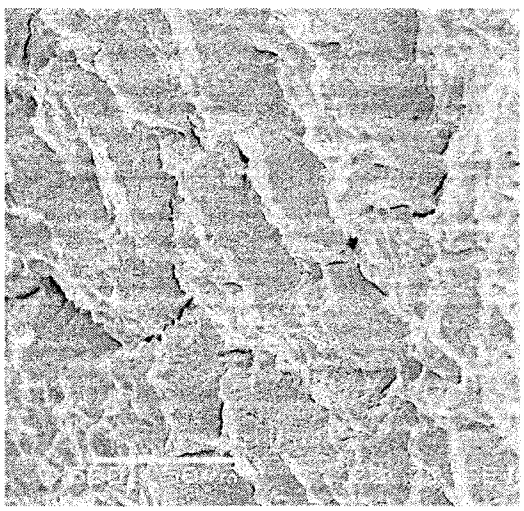

(a) RT

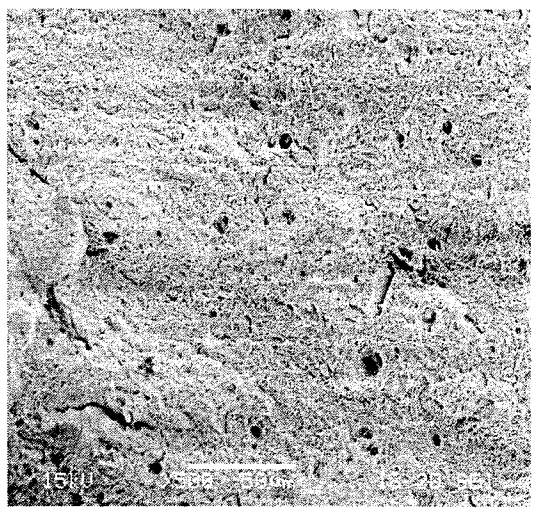

(b) 150°C

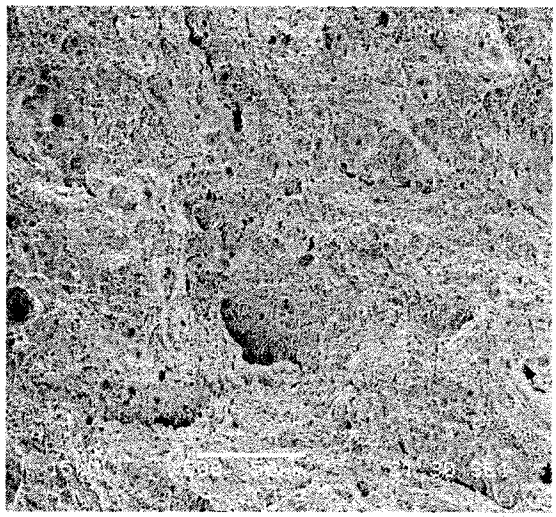

(c) 300°C

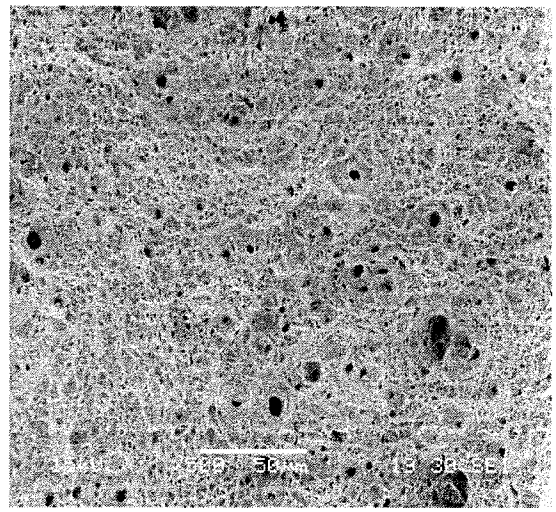

(d) 550°C

Figure 4-35 SEM Micrographs of Steel with 0.5 wt.% Si (Tensile Specimens)

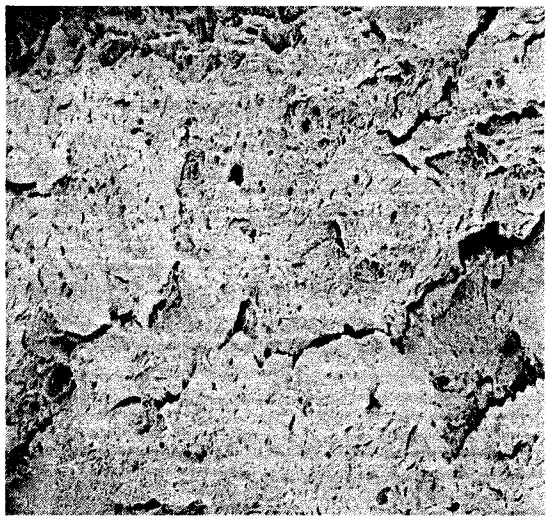

(a) RT

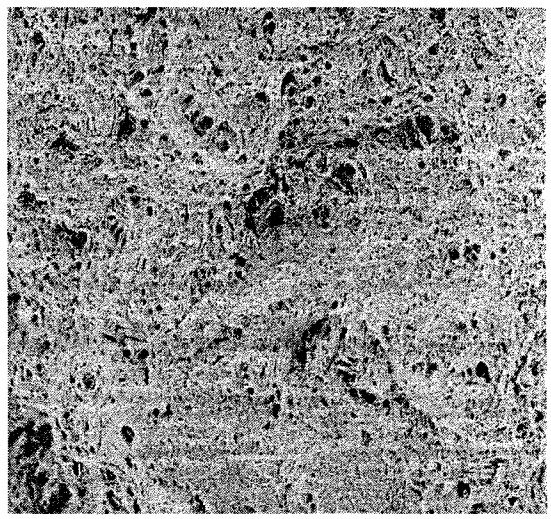

(b) 150°C

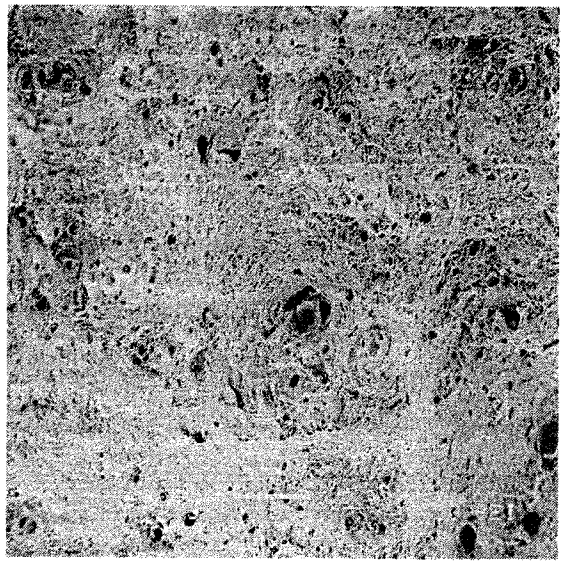

(c) 300°C

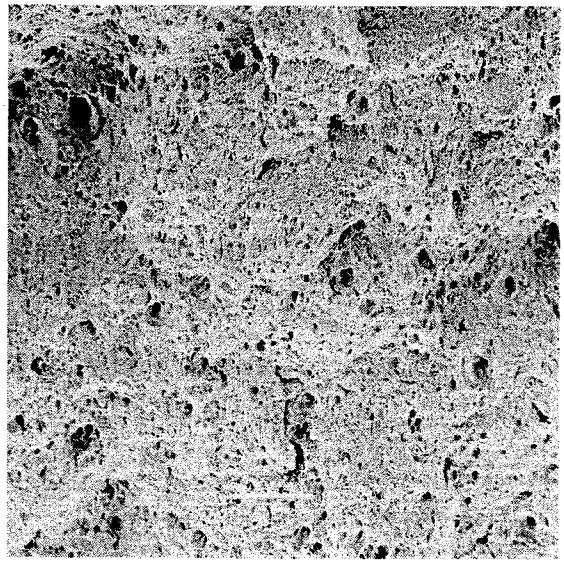

(d) 550°C

Figure 4-36 SEM Micrographs of Steel with 1 wt.% Si (Tensile Specimens)

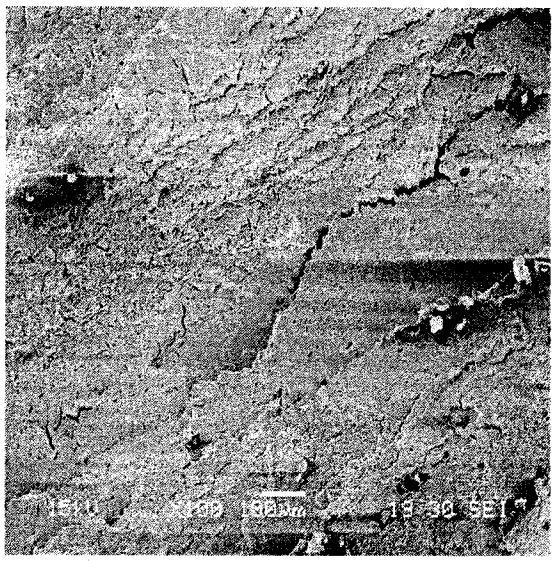

(a) RT

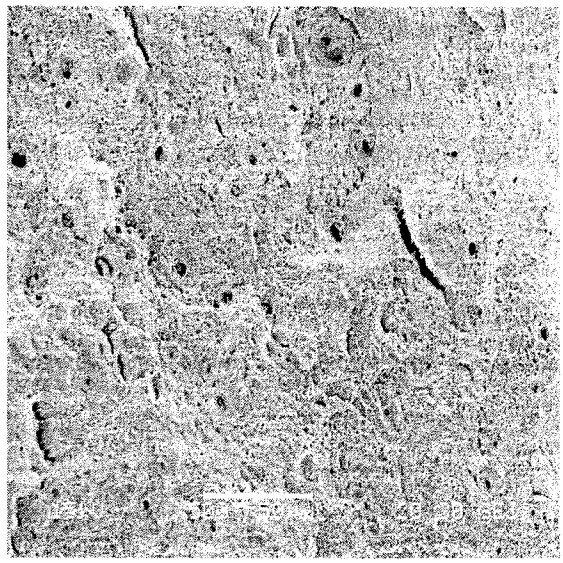

(b) 150°C

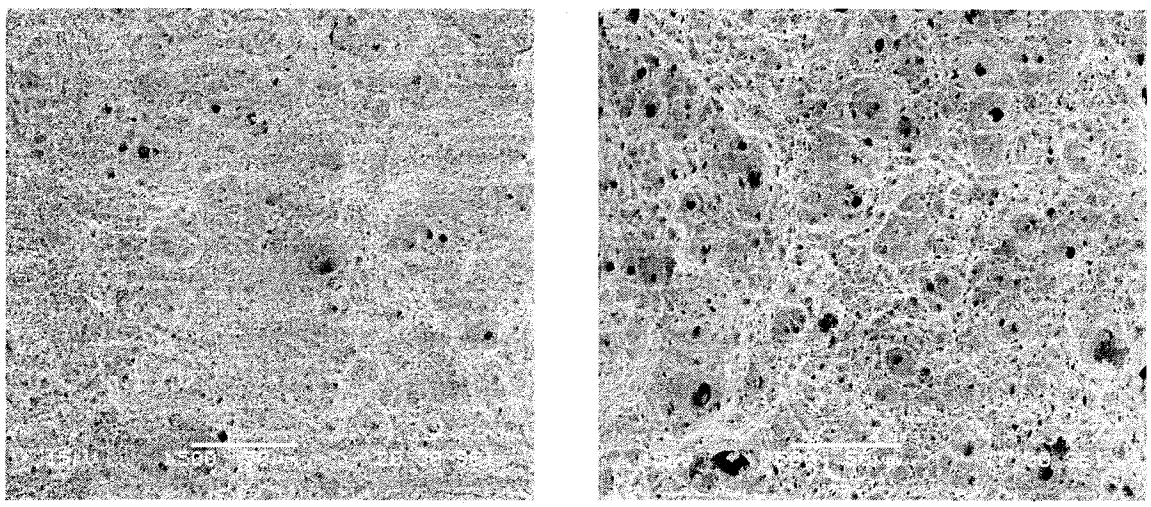

(c) 300°C (d) 550°C

Figure 4-37 SEM Micrographs of Steel with 1.5 wt.% Si (Tensile Specimens)

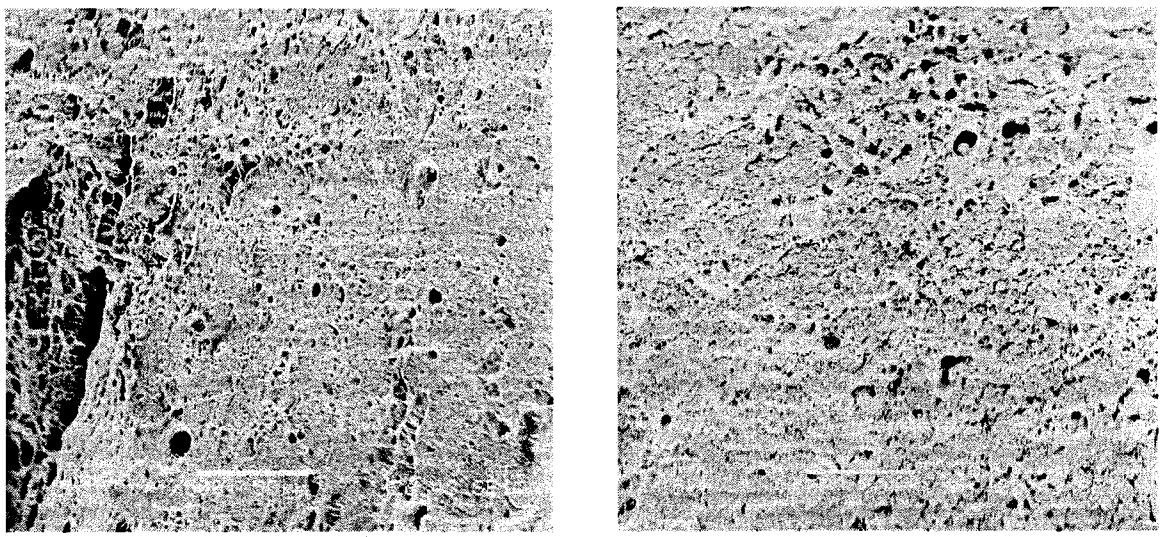

(a) RT (b) 150°C

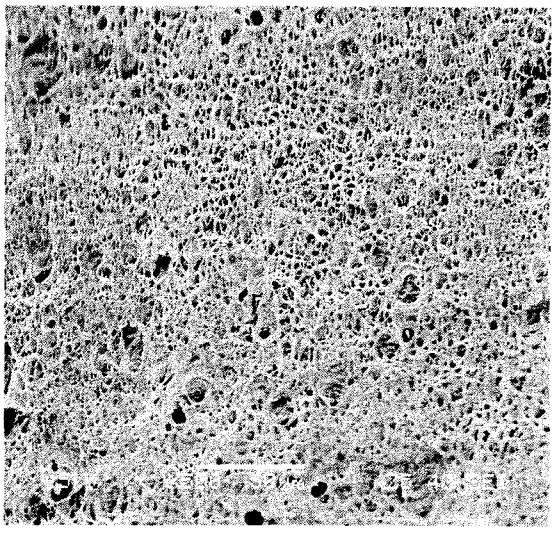

(c) 300°C

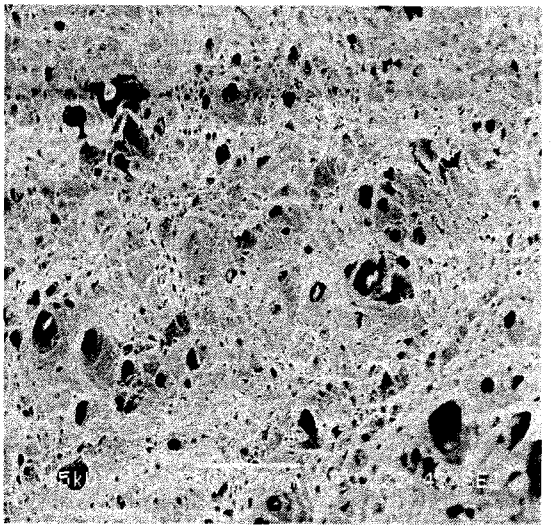

(d) 550°C

Figure 4-38 SEM Micrographs of Steel with 2 wt.% Si (Tensile Specimens)

The SEM micrographs of the fractured surfaces of CVN specimens of steel with varied Si content are illustrated in Figures 4-39 through 4-42. An evaluation of these micrographs reveals that all four alloys exhibited brittle failures characterized by cleavage and intergranular cracking . Simultaneously the presence of dimples was also noted in all micrographs. However, in general, larger dimples were seen in the steel containing 2 wt.% Si, especially at 340°C, as shown in Figure 4-42(c).

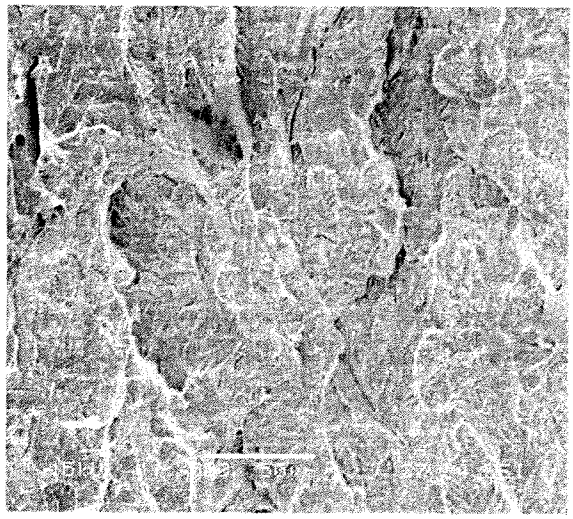

(a) -40° C

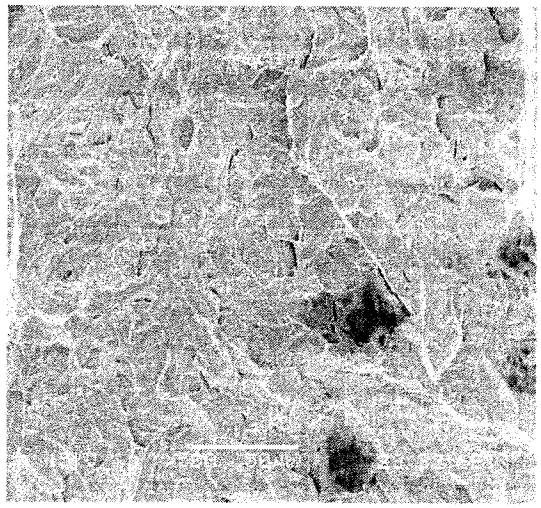

(b) 125°C

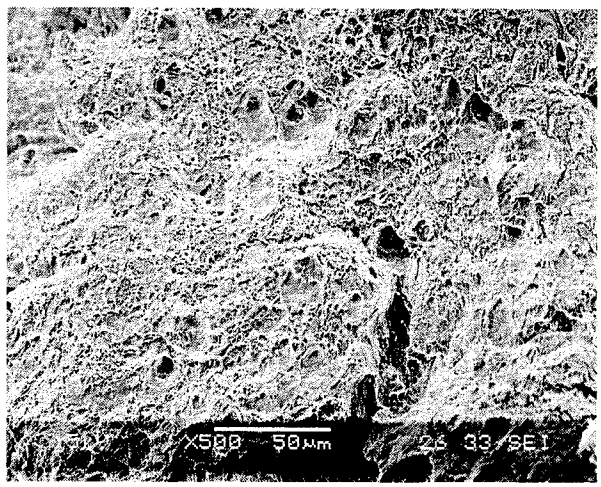

(c) 340°C

Figure 4-39 SEM Micrographs of Steel with 0.5 wt.% Si (CVN Specimens)

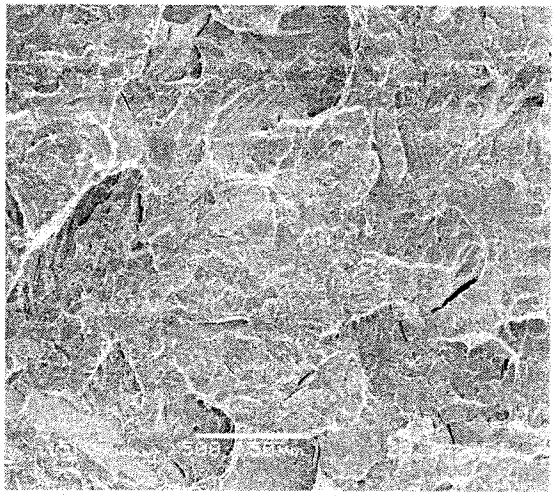

(a) -40° C

(b) 125°C

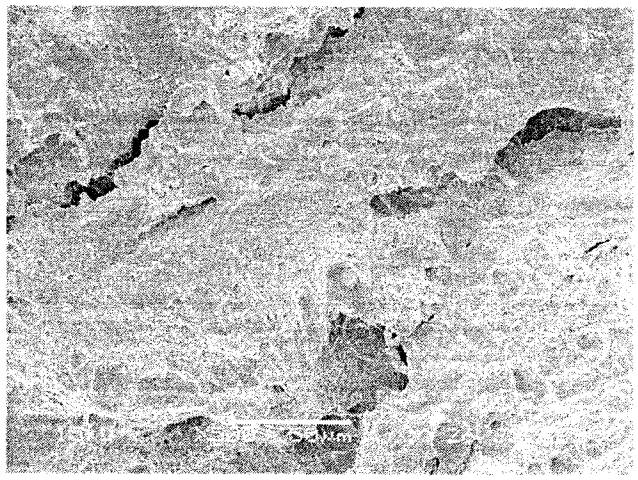

(c) 340°C

Figure 4-40 SEM Micrographs of Steel with 1 wt.% Si (CVN Specimens)

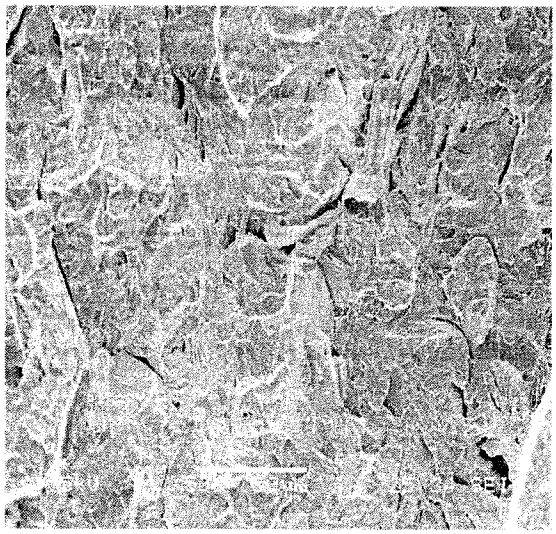

(a) -40° C

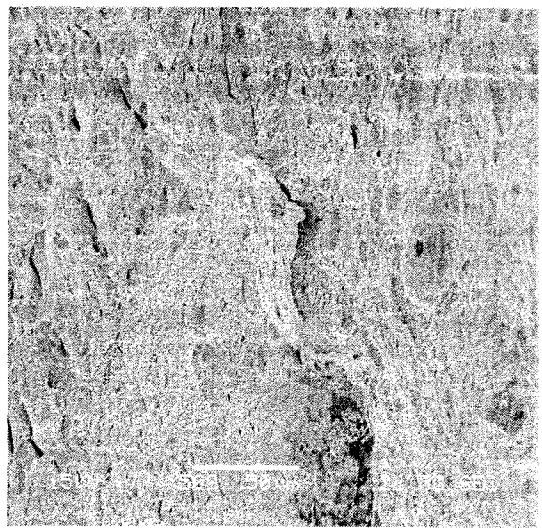

(b) 125°C

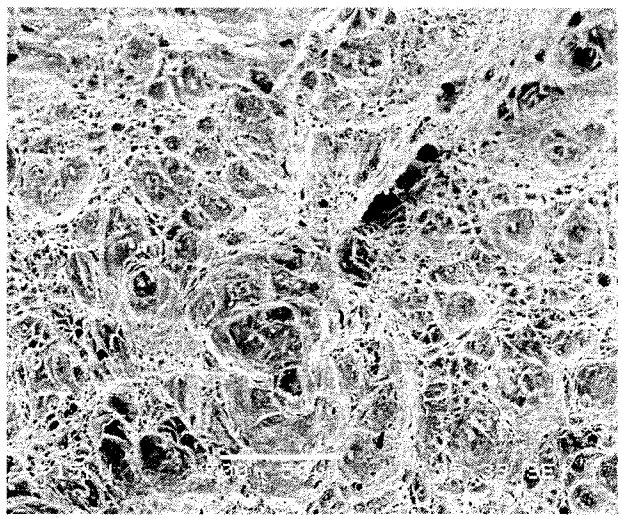

(c) 340°C

Figure 4-41 SEM Micrographs of Steel with 1.5 wt.% Si (CVN Specimens)

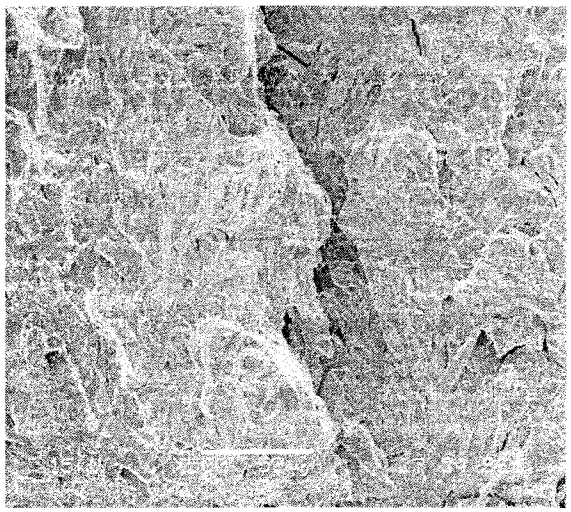

(a) -40° C

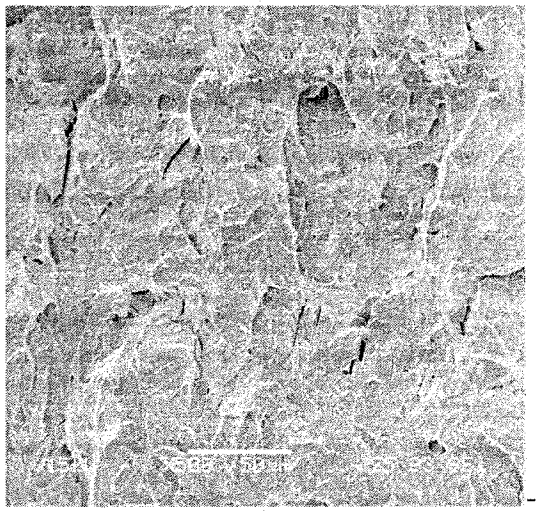

(b) 125°C

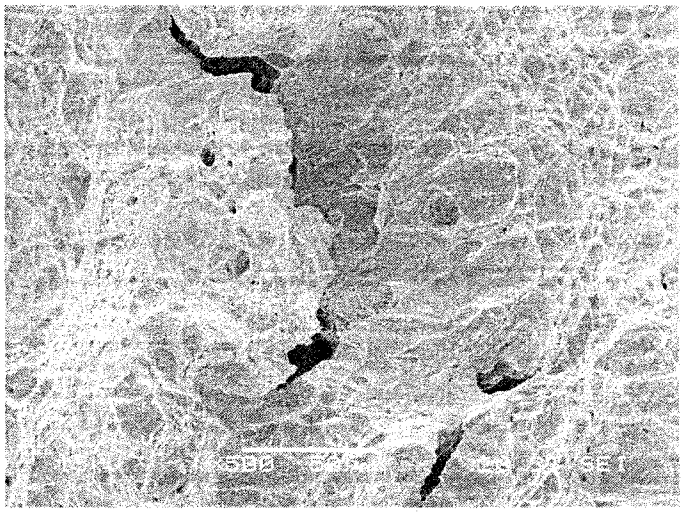

(c) 340°C

Figure 4-42 SEM Micrographs of Steel with 2 wt.% Si (CVN Specimens)

CHAPTER 5

DISCUSSION

The beneficial effect of higher Si content (approximately 1 wt.%) on both the metallurgical properties and corrosion resistance of martensitic Cr-Mo steels had been demonstrated in several investigations performed by researchers at MPL. In view of this finding, an extensive investigation was subsequently pursued to evaluate the role of Si content on both the metallurgical and corrosion performance of martensitic T91 grade steels for application as target structural materials related to the transmutation process. The results of corrosion studies involving T91 grade steels containing 0.5, 1.0, 1.5 and 2.0 wt.% Si have already been presented in a dissertation prepared by Maitra [5]. The current investigation was primarily focused on the evaluation of the metallurgical behavior of similar grades of steels under conditions relevant to the transmutation process. The metallurgical properties studied in this investigation include the tensile properties at ambient and elevated temperatures, impact resistance at cryogenic and elevated temperatures, and fracture toughness at ambient temperature and 300°C. The characterization of the fracture morphology of the tested specimens has also been performed using conventional analytical techniques.

The optical micrographs of all four heats of steels exhibited prior austenitic grains containing finely dispersed tempered-martensite, and ferrites, as anticipated in Cr-Mo steels. The tensile data obtained at a strain rate of 5×10^{-4} sec^{-1} revealed that the magnitude

of failure strain (e_f) was gradually reduced at temperatures ranging between ambient and 400°C, irrespective of the Si content. Further, the formation of serrations was noted at these temperatures, the extent of formation being more pronounced at 300°C. A combination of reduced e_f and formation of serrations within specific temperature regimes was attributed to the development of a metallurgical phenomenon, known as dynamic strain ageing (DSA). The concept of DSA is known to be associated with the diffusion of either interstitial or substitutional solute elements into the matrix of metals and alloys at susceptible temperature regimes under the influence of tensile loading. During such plastic deformation, the tested materials can experience work-hardening due to the precipitation of solute elements in the vicinity of imperfections such as dislocations that are generated during the deformation process. Thus, the mobility of dislocations will be significantly impaired, causing hardening of the matrix that can eventually lead to reduced plasticity within a susceptible temperature regime, as seen in this investigation. Beyond this critical temperature range, the diffusivity of the solute elements can be enhanced, thus, leading to increased ductility, as observed at 550°C.

The occurrence of DSA during tensile deformation can be significantly influenced by both temperature and strain rate. Thus, in order to develop a mechanistic understanding of this phenomenon, tensile testing involving all four heats of alloys was performed at several temperatures under three additional strain rates. Since diffusion is a thermally-activated process, an average activation energy (Q) based on these testing was computed for each heat of steel. The results indicate that the magnitude of Q (64-80 KJ/mol) was gradually enhanced with increasing Si content. A comparative analysis of the resultant Q values to literature data could not be performed due to the lack of such information. As to

the concentration of dislocations as a function of the testing temperature, the magnitude of dislocation density (ρ) was one order higher at 400°C compared to those at other temperatures, once again rationalizing the lowest e_f value obtained at this temperature during tensile testing.

The work hardening index (n) provides a measure of resistance to plastic deformation under tensile loading based on a relationship between true stress and true strain. The results indicate that the magnitude of n was gradually enhanced at temperatures ranging from ambient to 400°C, followed by a significant drop at 550°C. As indicated earlier, the susceptibility to DSA of all four heats was more pronounced at temperatures of 300°C and 400°C, where lowest e_f values and formation of serrations were observed. At these temperatures, the tested materials experienced the maximum resistance to plastic deformation due to the precipitation of solute elements, thus, minimizing the dislocation mobility within the matrix and past the grain boundaries. Beyond 400°C, the dislocations were able to move faster due to enhanced plasticity at a higher temperature. It should be noted that a consistent pattern on the effect of temperature on the measured n values was observed, irrespective of the Si content.

Classical impact energy versus temperature plots were developed based on impact testing using CVN specimens. A minimum impact resistance was observed with T91 grade steels containing 1.5 and 2.0 wt.% Si in terms of both absorbed energy and DBTT. Obviously, the presence of higher Si content proved to be detrimental from the impact resistance point of view. The fracture toughness in terms of K_Q was also relatively lower for steels containing 1.5 and 2.0 wt.% Si, suggesting an adverse effect of higher Si content on the resistance of T91 grade steels to failure in the presence of a sharp crack.

As to the fracture morphology of the tested specimens, a combination of ductile and brittle failures were observed. The brittle failures were characterized by intergranular cracking and cleavage facets. Limited ductility on the broken surfaces of the tested tensile specimens was characterized by dimpled microstructures. However, the steel containing 2 wt.% Si exhibited larger sized dimples at 550°C, indicating a relatively higher ductility.

CHAPTER 6

SUMMARY AND CONCLUSIONS

The role of silicon (Si) content on the metallurgical behavior of martensitic T91 grade steels has been studied in this investigation as function of different metallurgical variables. The metallurgical properties investigated include tensile strength and ductility, impact resistance, and fracture toughness of these steels containing Si ranging from 0.5 to 2.0 wt.%. The characterization of the failure morphology of the tested specimens has also been performed. The resultant data and the key conclusions derived from this investigation are presented below.

- As expected, the optical micrographs revealed the formation of fine tempered martensites within prior austenitic grains. Ferrites were also seen in these micrographs due to the presence of high chromium content.
- Irrespective of the Si content, all four heats of T91 grade steels exhibited gradually reduced failure strain and formation of serrations within a temperature range of ambient to 400°C. Such behavior can be attributed to the occurrence of dynamic strain ageing (DSA), which is influenced by both temperature and strain rate used in plastic deformation under tensile loading.
- The activation energy associated with the diffusion of solute elements at different temperatures ranged between 64 and 80 KJ/mol, as the Si content was increased from 0.5 to 2.0 wt.%.

- The dislocation density (ρ) of the tested tensile specimen was maximum at 400°C, showing an order of magnitude higher value due to enhanced precipitation of solute elements in the vicinity of dislocations and grain boundaries.
- The magnitude of work-hardening index (n) was gradually enhanced with increasing temperature up to 400°C, independent of the Si content. A maximum n value at this temperature is consistent with the lowest e_f value associated with greater resistance to plastic deformation due to reduced dislocation mobility.
- Classical impact energy versus temperature curves resulted, showing upper and lower shelf energies. Lower impact energies and higher DBTT values were observed with steels containing 1.5 and 2.0 wt.% Si, suggesting a detrimental effect of higher Si content on the impact resistance of T91 grade steels.
- The fracture toughness (K_{IC}) at ambient temperature was also impaired due to the presence of higher Si content in the tested materials. The crack tip of the compact-tension specimens became blunt at 300°C, leading to invalid K_{IC} measurements.
- Steels containing 0.5, 1.0 and 1.5 wt.% Si showed brittle failures characterized by intergranular cracking and cleavage facets, when tested under tensile loading, at temperatures ranging from ambient to 300°C. However, dimpled microstructures indicating ductile failures were seen with the steel containing 2.0 wt.% Si at all tested temperatures.

- The Charpy v-notch specimens exhibited a combination of intergranular cracking, cleavage failure and dimpled microstructures. The extent of brittle failure was more pronounced in the steel containing 2.0 wt.% Si.
- The overall data suggest that the presence of Si above 1 wt.% in T91 grade steels may be detrimental from the mechanical performance point of view.

CHAPTER 7

SUGGESTED FUTURE WORK

In view of the invalid K_{IC} values obtained at 300°C, it is suggested that additional fracture toughness testing be performed involving pre-cracked CT specimens at temperatures lower than 300°C. Further, an in-depth microstructural study needs to be performed to characterize the ferritic phase in the T91 grade steels.

APPENDIX A

TENSILE TESTING AT DIFFERENT STRAIN RATES

A1. Stress-Strain Diagrams using Cylindrical Specimens Tested at Different Strain Rates

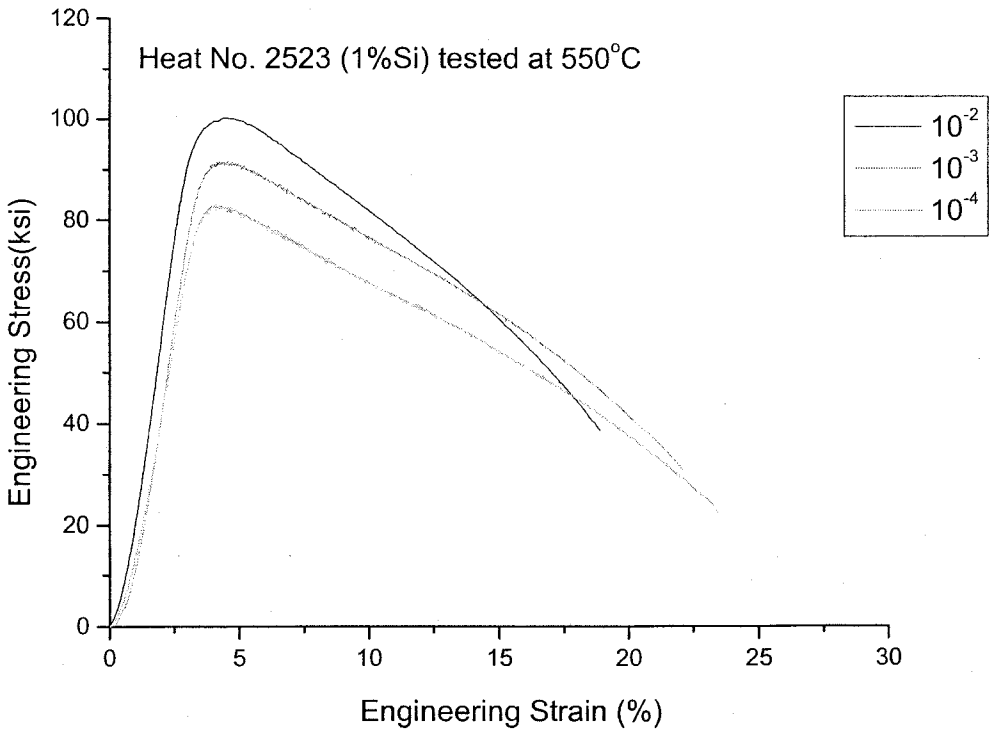

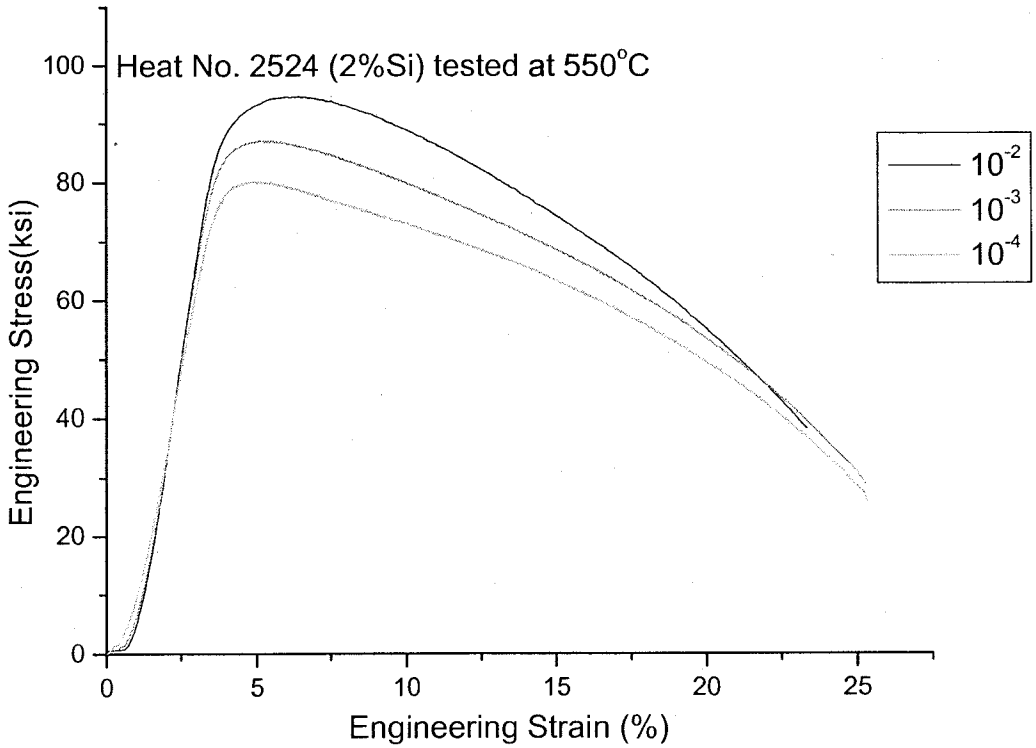

APPENDIX B

TEM MICROGRAPHS

B1. TEM Micrographs for Heat No. 2403 (0.5 wt% Si) tensile tested at 300°C

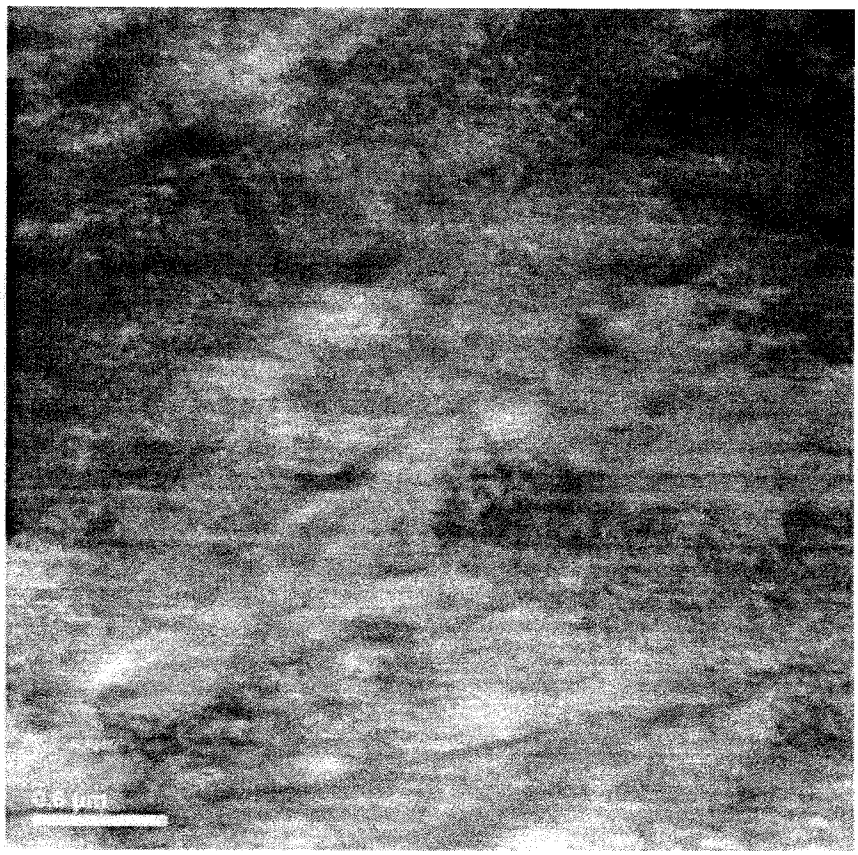

B2. TEM Micrographs for Heat No. 2403 (0.5 wt% Si) tensile tested at 550°C

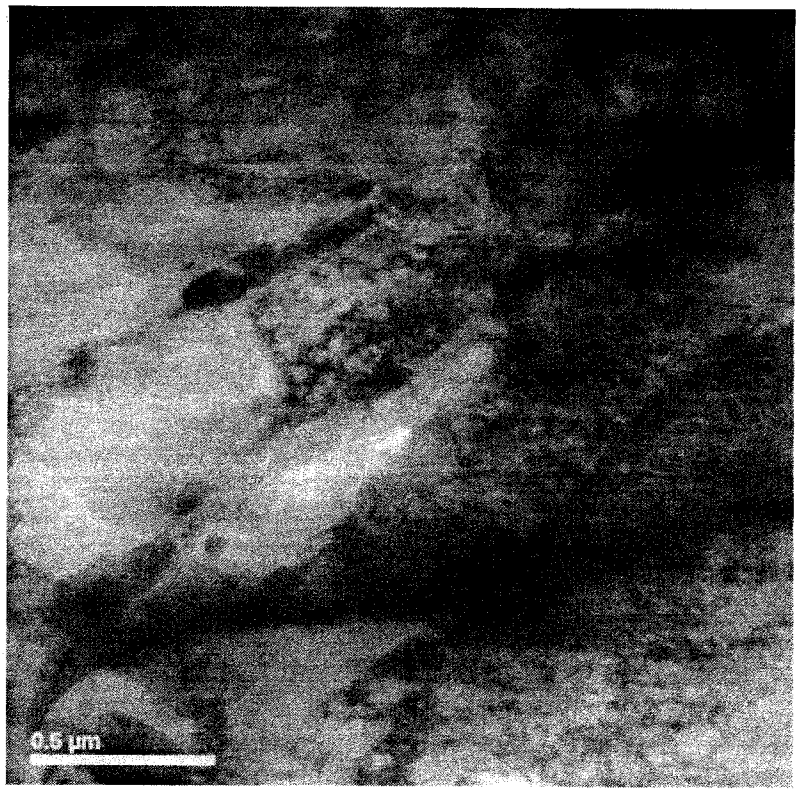

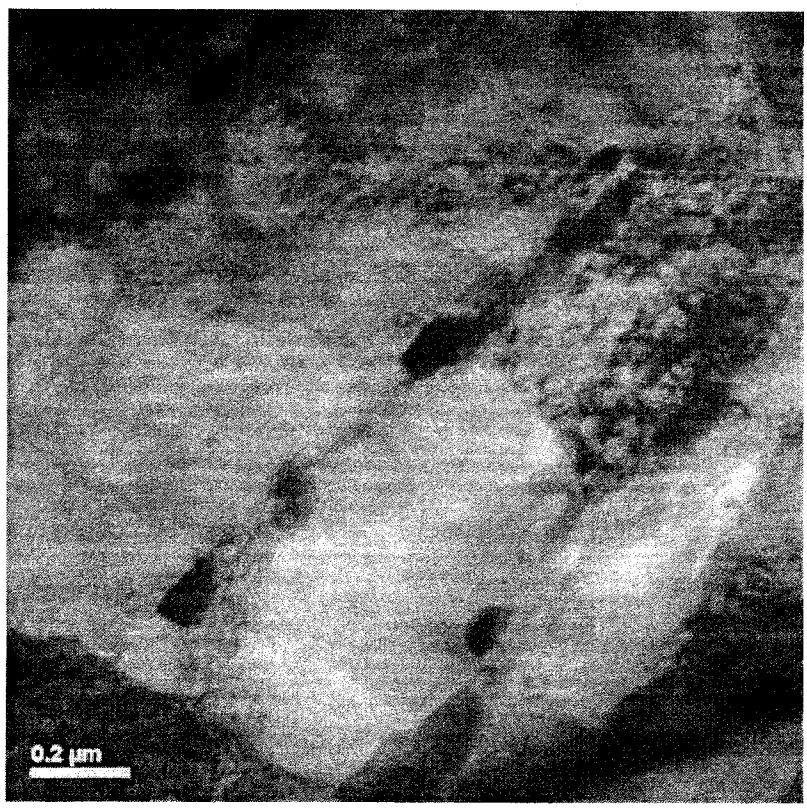

B3. TEM Micrographs for Heat No. 2404 (1.0 wt% Si) tensile tested at RT

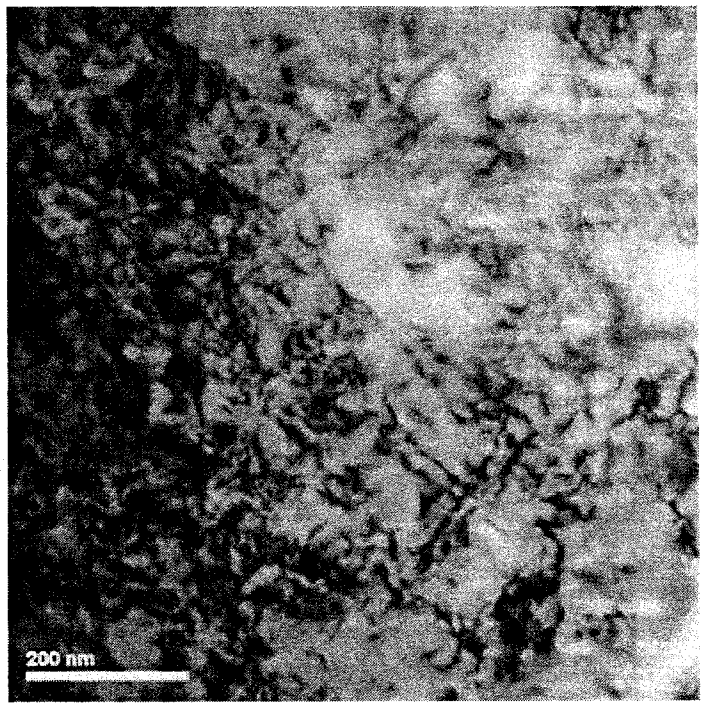

B4. TEM Micrographs for Heat No. 2404 (1.0 wt% Si) tensile tested at 300°C

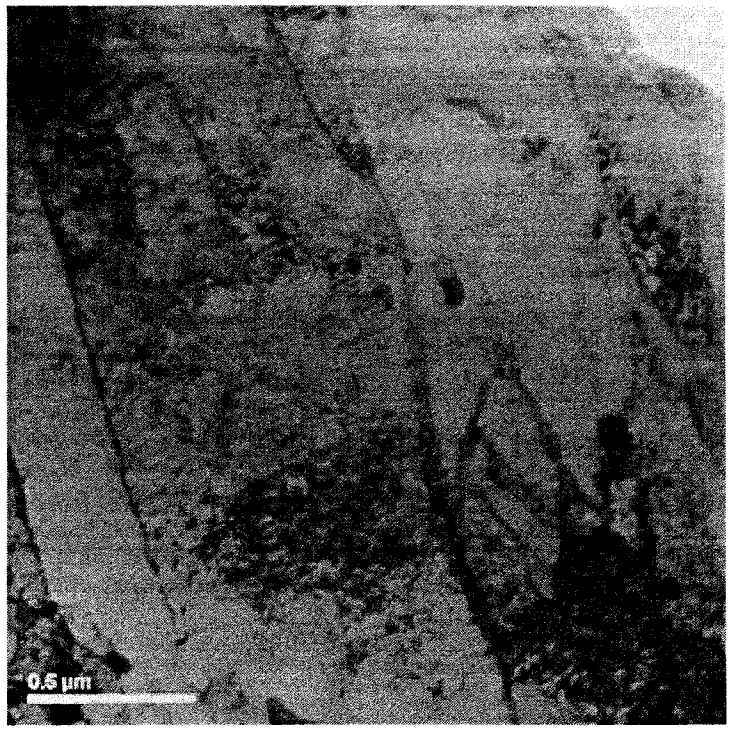

B5. TEM Micrographs for Heat No. 2405 (1.5 wt% Si) tensile tested at 300°C

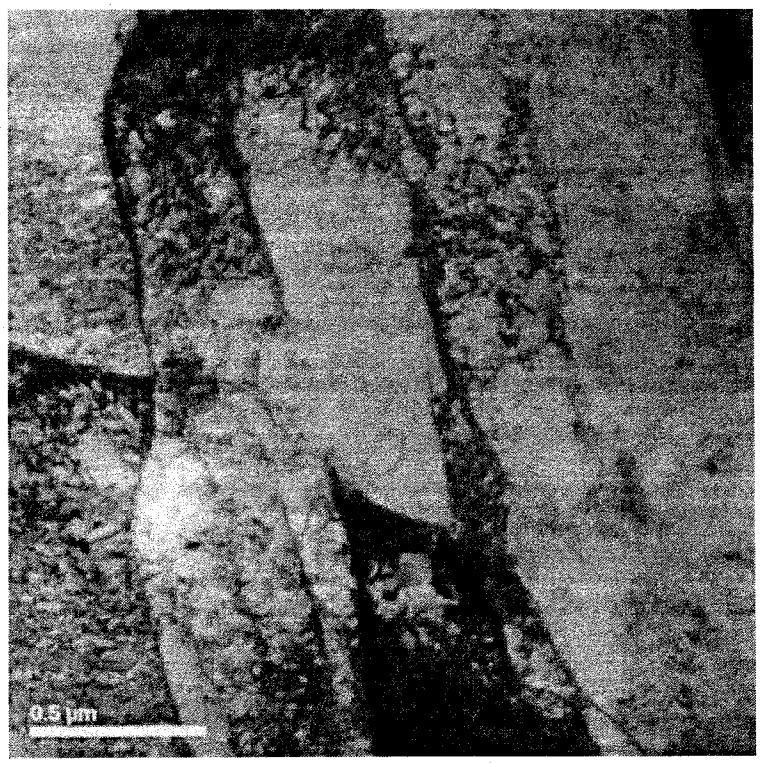

B6. TEM Micrographs for Heat No. 2406 (2 wt% Si) tensile tested at RT

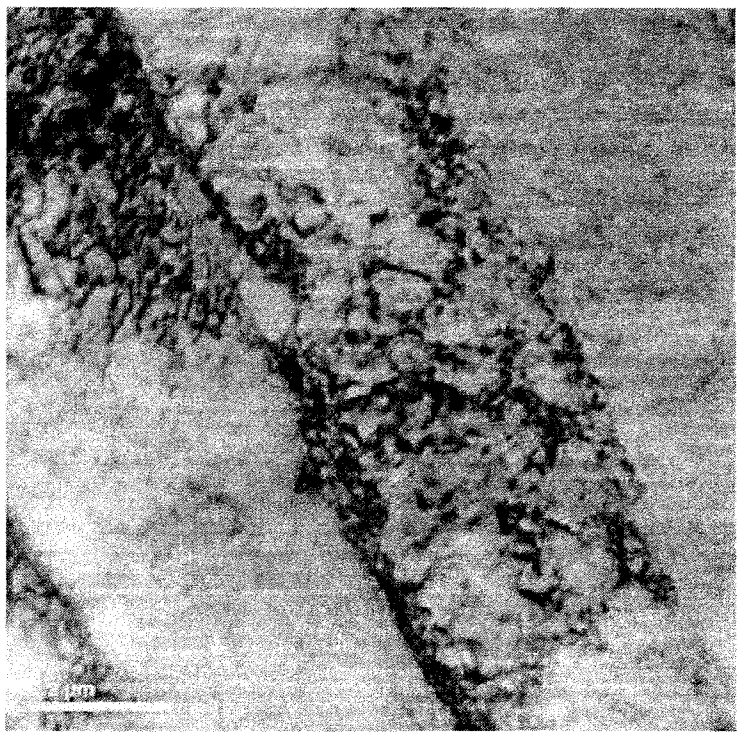

B7. TEM Micrographs for Heat No. 2406 (2 wt% Si) tensile tested at 300°C

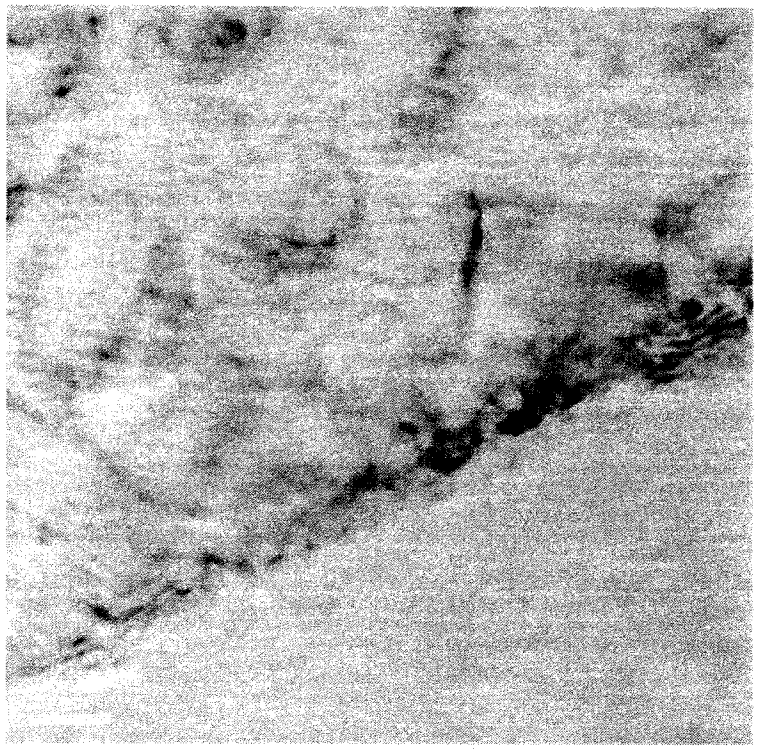

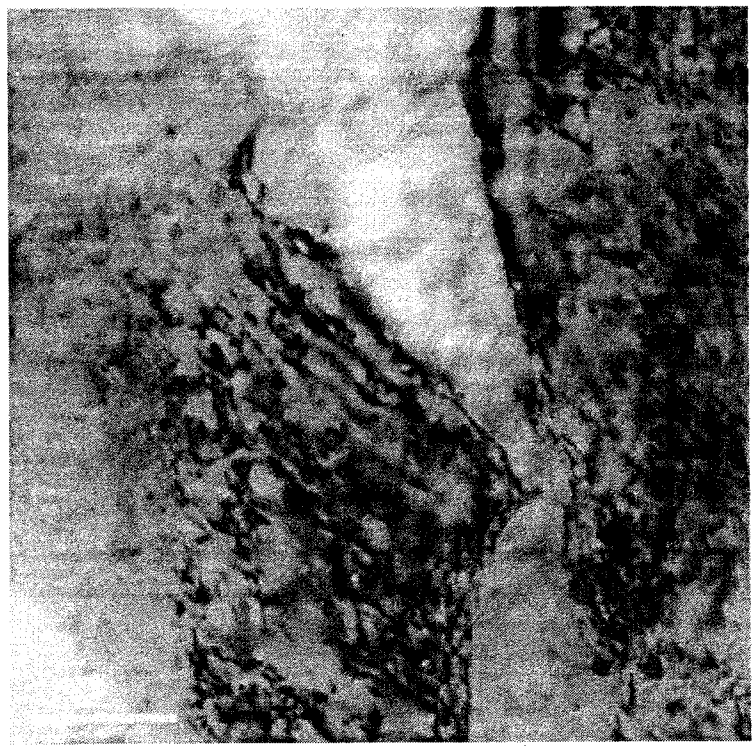

B8. TEM Micrographs for Heat No. 2406 (2 wt% Si) tensile tested at 400°C

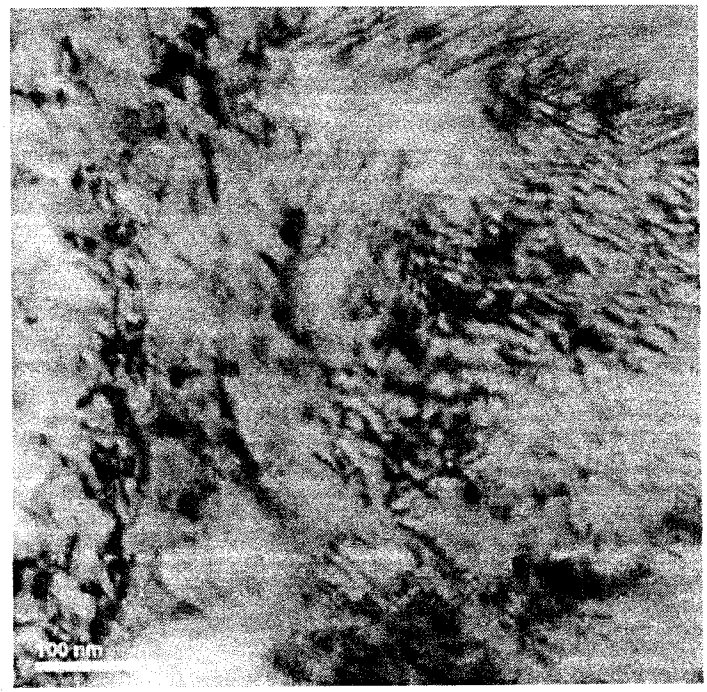

B9. TEM Micrographs for Heat No. 2406 (2 wt% Si) tensile tested at 550°C

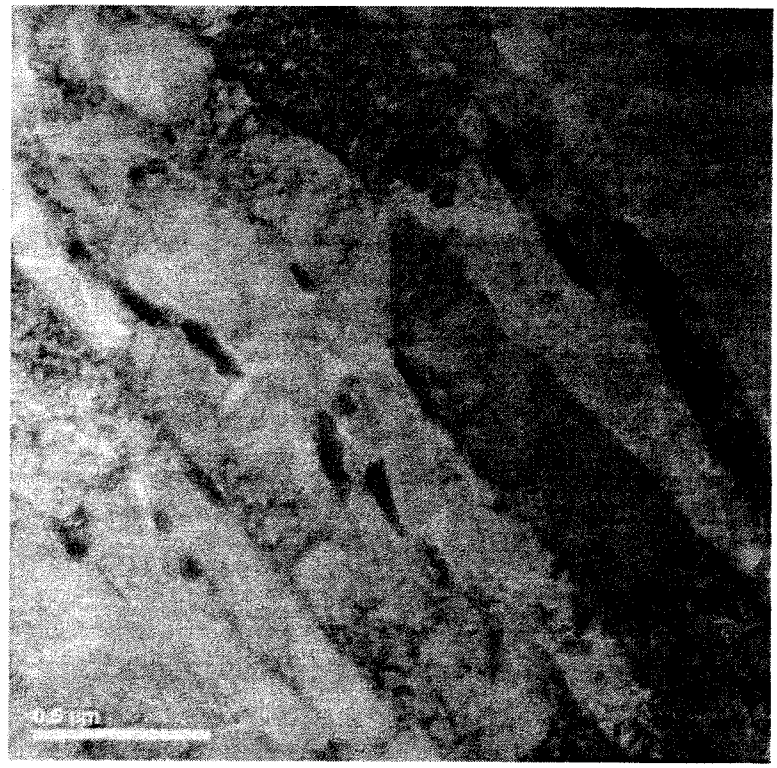

APPENDIX C

FRACTOGRAPHY

Fractography of Tensile Tested Specimens

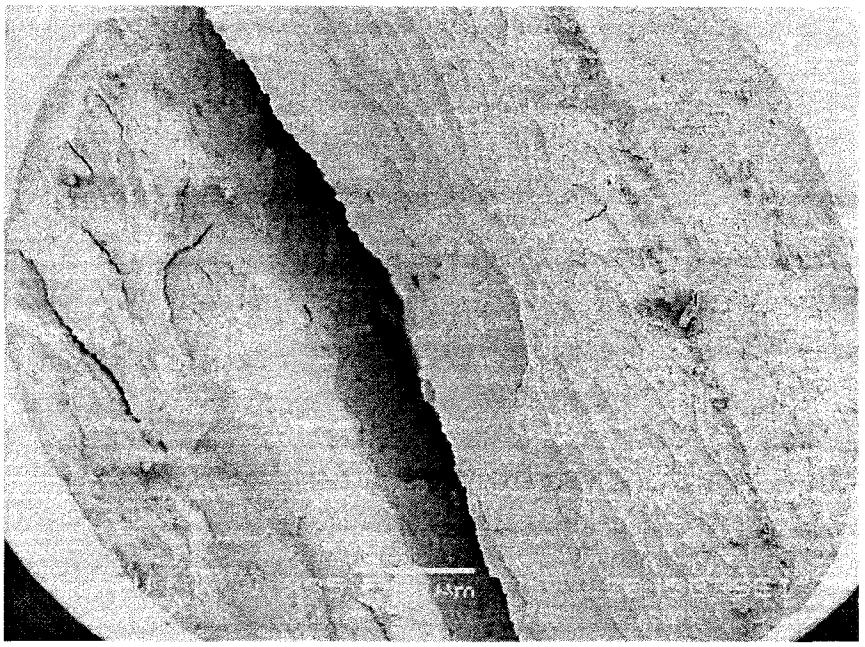

Heat No. 2403 (0.5% Si) Tensile Tested at RT

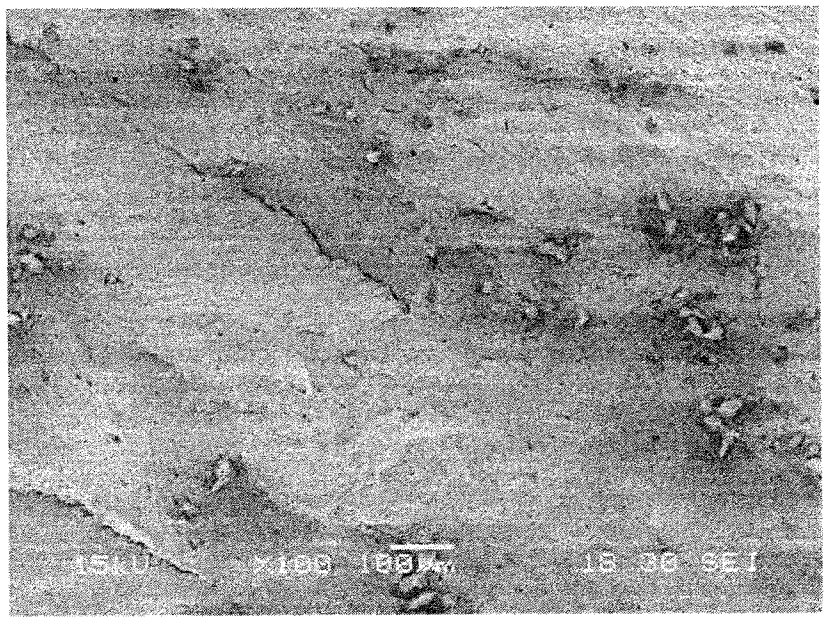

Heat No. 2403 (0.5% Si) Tensile Tested at 150°C

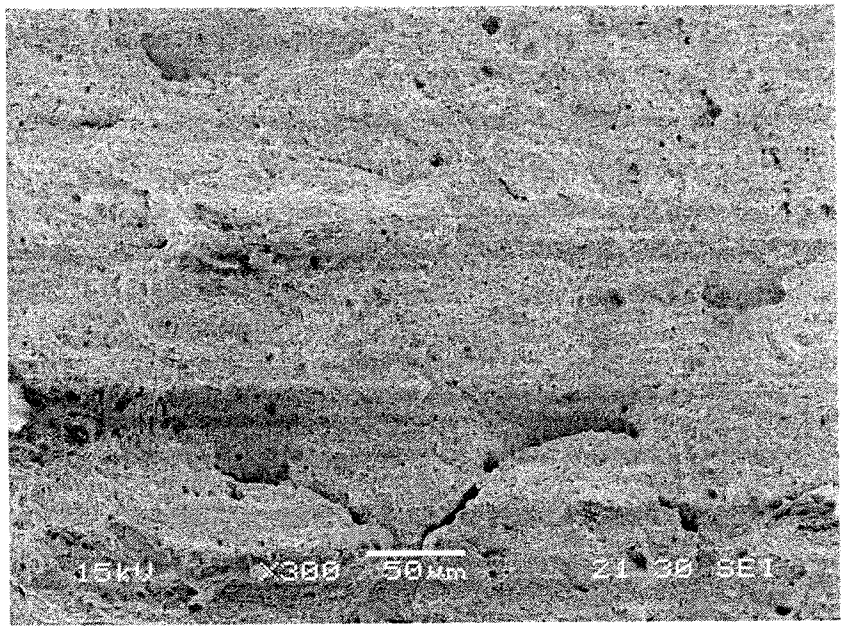

Heat No. 2403 (0.5% Si) Tensile Tested at 300°C

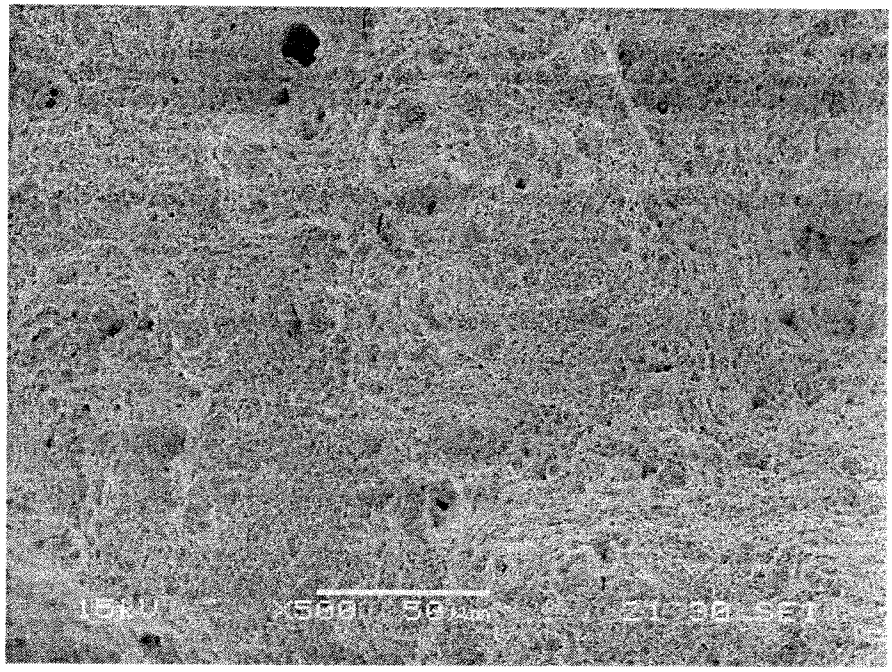

Heat No. 2403 (0.5% Si) Tensile Tested at 400°C

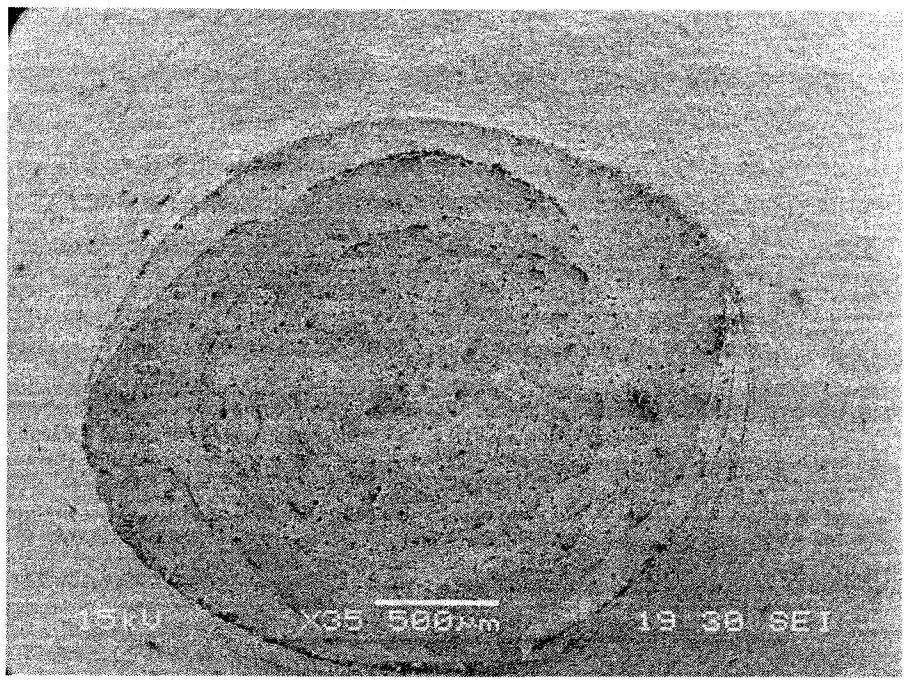

Heat No. 2403 (0.5% Si) Tensile Tested at 550°C

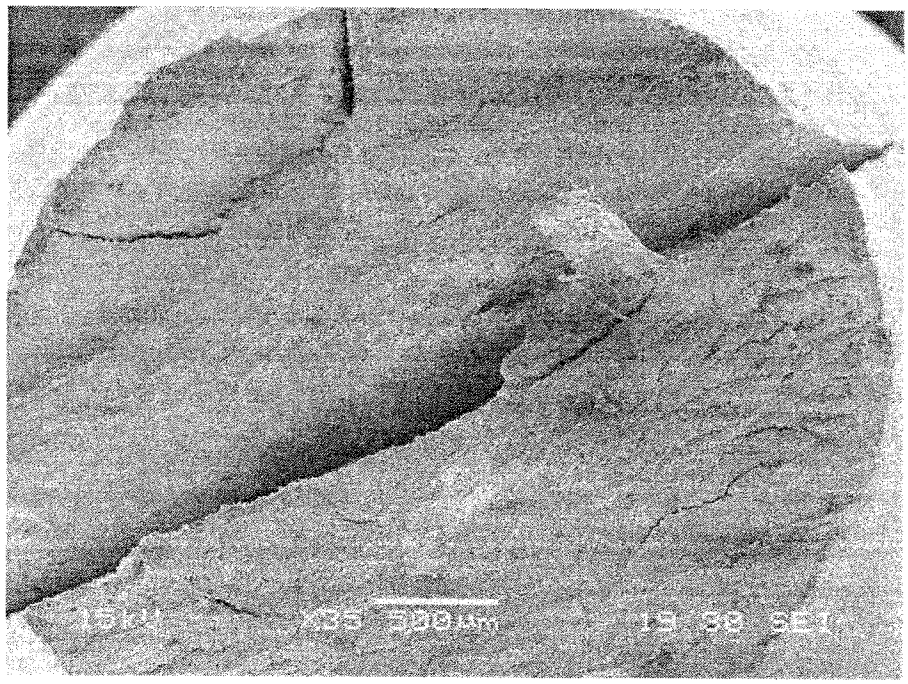

Heat No. 2405 (1.5% Si) Tensile Tested at RT

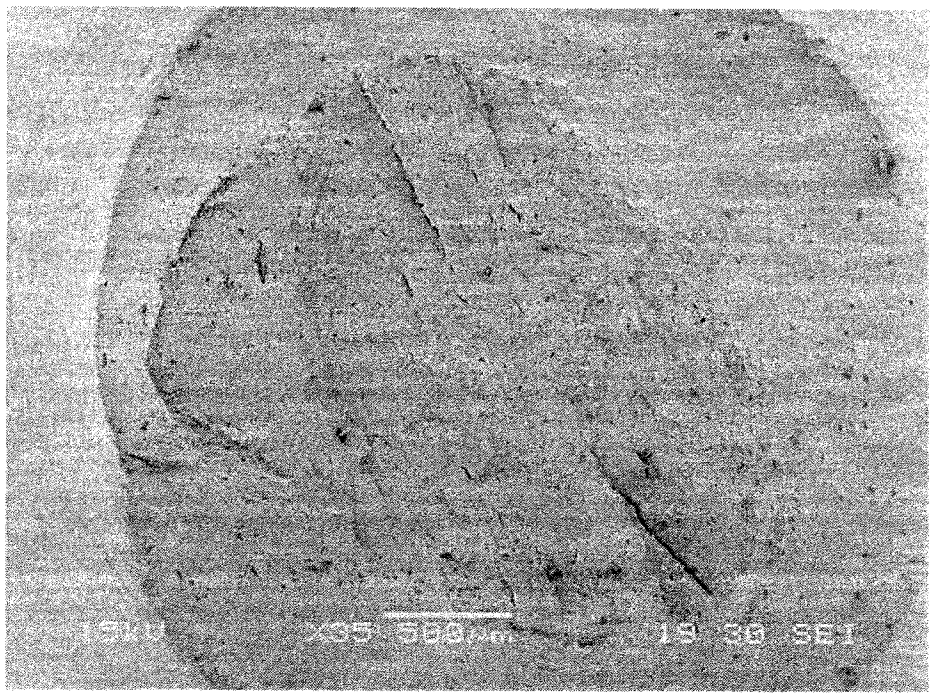

Heat No. 2405 (1.5% Si) Tensile Tested at 150°C

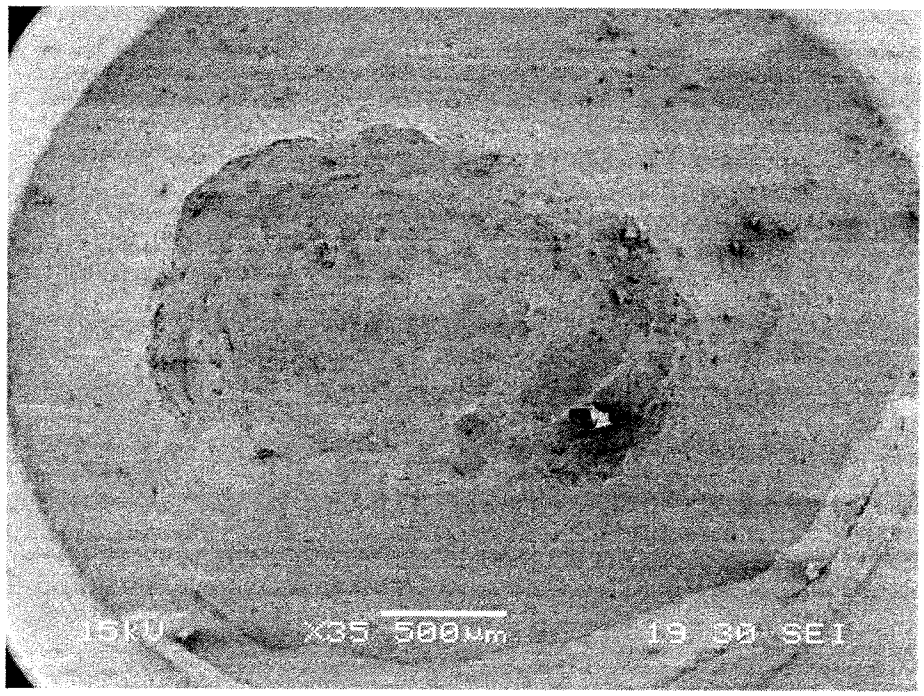

Heat No. 2405 (1.5% Si) Tensile Tested at 300°C

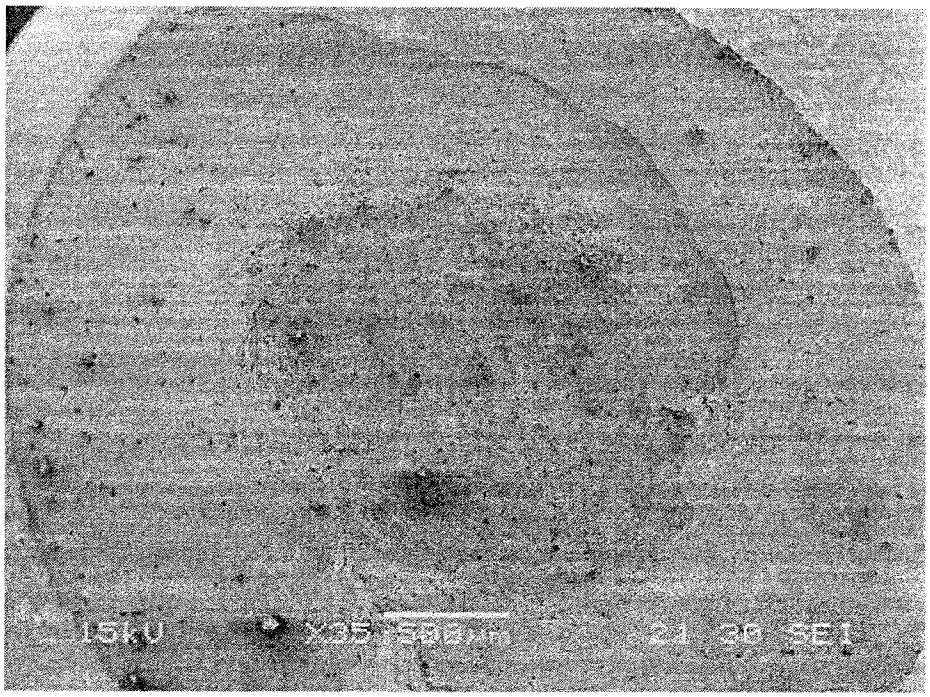

Heat No. 2405 (1.5% Si) Tensile Tested at 400°C

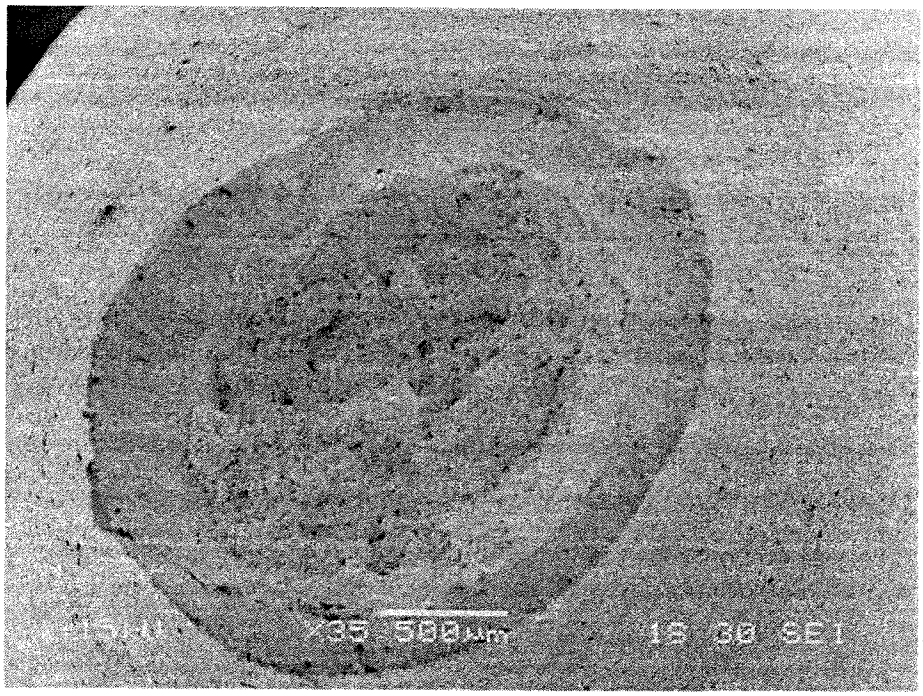

Heat No. 2405 (1.5% Si) Tensile Tested at 550°C

APPENDIX D

UNCERTAINTY ANALYSES OF EXPERIMENTAL RESULTS

The parameters like lengths, times etc. are directly measured in any experiment. The instruments used to determine these measurements may vary in quality every time they are being used. Also, the parameters that are out of control of the researcher might cause undesired variations in these measurements. Efforts were taken to repeat all the experiments in order to determine an average value. However, the undesired variations might have caused variations in the derived results. These variations if caused by the machines used in the experiments can be reduced by calibrating them on a timely basis. However the variations caused due to human errors and environmental factors cannot be avoided. Uncertainty analysis of these derived results determines the variations/errors in them.

A precise method of estimating uncertainty in experimental results has been presented by Kline and McClintock. The method is based on a careful specification of the uncertainties in the various primary experimental measurements. When the plus or minus notation is used to designate the uncertainty, the person making this designation is stating the degree of accuracy with which he or she believes the measurement has been made. It is notable that this specification is in itself uncertain because the experiment is naturally uncertain about the accuracy of these measurements. If a very careful

calibration of an instrument has been performed recently, with standards of very high precision, then the experimentalist will be justified in assigning a much lower uncertainty to measurements than if they were performed with a gage or instrument of unknown calibration history.

Most of the instruments in the Materials Performance Laboratory (MPL) were calibrated on a regular basis by Bechtel Nevada using standards with very high precision. Thus, it is expected that the resultant data presented in this thesis would have very insignificant uncertainty. The uncertainties in the results of this investigation are calculated by using the Kline and McClintock Method. The equation used for this method is given below.

$$W_R = \left[\left(\frac{\partial R}{\partial x_1} w_1 \right)^2 + \left(\frac{\partial R}{\partial x_2} w_2 \right)^2 + \cdots + \left(\frac{\partial R}{\partial x_n} w_n \right)^2 \right]^{\frac{1}{2}} \qquad \text{Equation A1}$$

Where, W_R = the uncertainty in the results

R = the given function of the independent variables $x_1, x_2, \ldots\ldots x_n$)

$R = R(x_1, x_2, \ldots\ldots x_n)$

$w_1, w_2, \ldots\ldots w_n$ = the uncertainty in the independent variables

D.1 Uncertainty Calculation in Instron Results

The results generated from the Instron testing equipment are stress (σ), percentage elongation (%El), and percentage reduction in area (%RA). The stress is based on the load (P) and the initial cross-sectional area (A_i) of the tested specimen. The %El is based

on the change in length (Δl) during the testing and the %RA is based on the initial and final cross-sectional areas (A_i and A_f). The magnitude of P was obtained from the load-cell of the Instron unit. The values for Δl, A_i, and A_f were calculated based on measurements by a caliper. The uncertainties in load-cell and caliper were ± 0.03% lbs and ± 0.001 inch, respectively, obtained from the calibration. The uncertainty in the initial notched diameter was ± 0.001, which was provided by the manufacturer and the uncertainty in the final notched diameter was ± 0.001 obtained by using the caliper.

$$\sigma = P/A_i \qquad \text{Equation A2}$$

D.1.1 Calculation of Uncertainty in Stress (U_σ)

$U_\sigma = U_{(P, Ai)}$

$U_{Ai} = (U_{Di})^2$

Uncertainty in load-cell = ± 0.03% lb

Uncertainty in caliper = ± 0.001 inch.

Sample calculation:

For yield stress (YS) = 129 ksi

The measured load (P) = 6321 lbf

Uncertainty in load (U_P) = 6321 × 0.0003

= ± 1.8963

Uncertainty in cross-sectional area (U_{Ai}) for the smooth tensile specimen:

Initial Diameter (D_i) = 0.2505 inch.

Uncertainty in diameter (U_{Di}) = ± 0.001 inch.

$$\text{Area } (A_i) = \frac{\pi D_i^{\,2}}{4}$$

$$= 0.0493 \text{ inch}^2$$

$$\frac{dA_i}{dD_i} = \frac{\pi D_i}{2}$$

$$= 0.393$$

$$\text{Uncertainty in area, } U_{Ai} = \left[\left(\frac{dA_i}{dD_i} \cdot U_{Di}\right)^2\right]^{\frac{1}{2}}$$

$$= 0.393 \times 0.001$$

$$= \pm 0.000393$$

$$\text{Uncertainty in stress, } U_\sigma = \left[\left(\frac{\partial \sigma}{\partial P} \cdot U_P\right)^2 + \left(\frac{\partial \sigma}{\partial A_i} \cdot U_{A_i}\right)^2\right]^{\frac{1}{2}} \qquad \text{Equation A3}$$

$$\sigma = \frac{P}{A_i}$$

$$\frac{\partial \sigma}{\partial P} = \frac{1}{A_i}$$

$$= 20.284$$

$$\frac{\partial \sigma}{\partial A_i} = -\frac{P}{A_i^{\,2}}$$

$$= -2600716.3866$$

Now providing all the numerical values in Equation A3 obtained from the calculation, it is found that,

$$U_\sigma = \left[(20.284 * 1.8963)^2 + (2600716.3866 * 0.000393)^2\right]^{\frac{1}{2}}$$

$$= 1022.81 \text{ psi} = \pm 1.023 \text{ ksi}$$

One example of the use of the uncertainty analysis is shown in this section. This can be implemented to all experimental results discussed in this dissertation.

D.1.2 Calculation of Uncertainty in Percentage Elongation ($U_{\%El}$)

Sample calculation:

Change in length (Δl) = 0.233 inch.

Gage length (l) = 1 inch.

$$\%El = \frac{\Delta l}{l} \cdot 100$$

Uncertainty in Δl ($U_{\Delta l}$) = $\pm$ 0.001

Uncertainty in %El ($U_{\%El}$),

$$U_{\%El} = \left[\left(\frac{d\%El}{d\Delta l} \cdot U_{\Delta l} \right)^2 \right]^{\frac{1}{2}} \qquad \text{Equation A4}$$

$$\frac{d\%El}{d\Delta l} = \frac{100}{l}$$

$$= 100$$

Providing all the calculated values in Equation A4, it is found that,

$$U_{\%El} = \left[(100 * 0.001)^2 \right]^{\frac{1}{2}}$$

$$U_{\%El} = \pm 0.1$$

One example of the use of the uncertainty analysis is shown in this section. This can be implemented to all experimental results discussed in this dissertation.

D.1.3 Calculation of Uncertainty in Percentage Reduction in Area ($U_{\%RA}$)

Sample calculation:

For %RA = 60.0%

Uncertainty in initial cross-sectional area (U_{Ai}) for the smooth specimen:

Initial Diameter (D_i) = 0.2505 inch.

Uncertainty in initial diameter,

$(U_{Di}) = \pm 0.001$ in

$$\text{Area } (A_i) = \frac{\pi D_i^{\,2}}{4}$$

$$= 0.0493 \text{ inch}^2$$

$$\frac{dA_i}{dD_i} = \frac{\pi D_i}{2}$$

$$= 0.393$$

Uncertainty in initial cross-sectional area,

$$U_{A_i} = \left[\left(\frac{dA_i}{dD_i} \cdot U_{D_i} \right)^2 \right]^{\frac{1}{2}}$$

$$= 0.393 \times 0.001$$

$$= \pm 0.000393$$

Uncertainty in final cross-sectional area (U_{Af}) for the smooth specimen:

Final Diameter (D_f) = 0.1584 inch.

Uncertainty in final diameter (U_{Df}),

$= \pm 0.001$ inch.

$$\text{Area } (A_f) = \frac{\pi D_f^{\,2}}{4}$$

$$= 0.01972 \text{ inch}^2$$

$$\frac{dA_f}{dD_f} = \frac{\pi D_f}{2}$$

$$= 0.2488$$

Uncertainty in final cross-sectional area,

$$U_{A_f} = \left[\left(\frac{dA_f}{dD_f} \cdot U_{D_f}\right)^2\right]^{\frac{1}{2}}$$

$$= 0.2488 \times 0.001$$

$$= 0.0002488$$

Uncertainty in %RA,

$$U_{\%RA} = \left[\left(\frac{\partial \%RA}{\partial A_i} \cdot U_{A_i}\right)^2 + \left(\frac{\partial \%RA}{\partial A_f} \cdot U_{A_f}\right)^2\right]^{\frac{1}{2}} \qquad \text{Equation A5}$$

$$\%\text{RA} = \left(\frac{A_i - A_f}{A_i}\right) \times 100$$

$$= \left(1 - \frac{A_f}{A_i}\right) \times 100$$

$$\frac{\partial \%RA}{\partial A_i} = \frac{100 A_f}{A_i^{\,2}}$$

$$= 811.36$$

$$\frac{\partial \%RA}{\partial A_f} = -\frac{100}{A_i}$$

$$= -2028.40$$

Now assigning all the calculated values in Equation A5, it is found that,

$$U_{\%RA} = \left[(811.36 * 0.000393)^2 + (-2028.40 * 0.0002488)^2\right]^{\frac{1}{2}}$$

$$= 0.597$$

One example of the use of the uncertainty analysis is shown in this section. This can be implemented to all experimental results discussed in this dissertation.

BIBLIOGRAPHY

[1] Addressing the Nuclear Waste Issue, Advanced Fuel Cycle Initiative (AFCI) Website http://afci.lanl.gov/pdf/AAApamphlet.pdf

[2] A. V. Locating, V. V. Olav, A. I. Filin, "Transmutation of Long-Lived Nuclides in the Fuel Cycle of Brest-Type Reactors", (RDIPE, Moscow, Russia)

[3] Yucca Mountain Project, Office of Civilian Radioactive Waste Management

[4] Addressing the Website www.lanl.gov/lead-bismuthEutectic

[5] Debajyoti Maitra, "Tensile Deformation and Environmental Degradation of T91 Grade Steels with Different Si Content", Ph.D. Dissertation, June 2006

[6] X. Zia, et al., "Microstructure in Martensitic Steels T91 and F82H After Irradiation in SINQ Target-3", Journal of Nuclear Materials, Vol. 318, pp. 207-214, 2003

[7] Y. Dai, et al., "Mechanical Properties of Modified 9Cr-1Mo (T91) Irradiated at 6300C in SINQ Target-3", Journal of Nuclear Materials, Vol. 318, pp. 192-199, 2003

[8] Y. Dai, "Proceedings of ICANS-XIII and ESS-PM4", pp. 604, PSI, Oct. 1995

[9] R.L. Klueh, " Proceedings of 1st International Workshop on Spallation Materials Technology", pp. 3.3–19, April 1996, Oak Ridge

[10] T. Hayashi, K. Ito, et al., "The Effect of Nb and W Alloying Additions to the Thermal Expansion Anisotropy and Elastic Properties of Mo_5Si_3" Met. And Mat. Tran. A, Vol. 36A, pp. 533-535, March 2005

[11] A.M. Huntz, V Bague, et al., "Effect of Silicon on the Oxidation Resistance of 9% Cr Steels", Applied Surface Science, Vol. 207, No. 1-4, pp. 255-275, Feb 28, 2003

[12] R.Nishimura, K. Yamakawa, J. Ishiga et al, "Highly Corrosion Resistant Stainless Steel with Si Implanted/Deposited Phase, Materials Chemistry and Physics, Vol. 54, No. 1-3, pp. 289-292, July 1998

[13] Allen Johnson, Eric P. Loewen, et al., "Spectroscopic and Microscopic Study of the Corrosion of Iron-Silicon Steel by Lead-Bismuth Eutectic (LBE) at Elevated Temperatures", Journal of Nuclear Materials, Vol. 350 pp. 221-231, 2006

[14] Ajit K. Roy, Ramprashad Prabhakaran, et al., "Stress Corrosion Cracking of Nuclear Transmutation Structural Materials," Materials Performance, NACE International, September 2004, Vol. 43, No. 9, pp. 52-56

[15] Ramprashad Prabhakaran, Ajit K. Roy, Mohammad K. Hossain, Sudheer Sama, "The Effect of Environmental and Mechanical Variables on Stress Corrosion Cracking of Martensitic Stainless Steels for Transmutation Applications," Proceedings of The 12th International Conference on Nuclear Engineering (ICONE12), Paper No. 49399, April 25-29, 2004.

[16] Ramprashad Prabhakaran,"Environmental Effects on a Candidate Structural Material for Transmutation Application," ANS Student Conference 2004, April 1-3, 2004, Madison, WI

[17] "Valve Magazine", Vol. 13, No. 1, pp. 3, winter 2001

[18] R. K. Williams, R. S. Graves, and D. L. McElroy, "Thermal and Electrical Conductivities of an Improved 9 Cr-1 Mo Steel from 360 to 1000 K", International Journal of Thermophysics, Vol. 5, No. 3, 1984

[19] ASTM Designation E8-2004, "Standard test methods for tensile testing of metallic materials", American Society for Testing and Materials (ASTM) International.

[20] ASTM Designation E 399-1999, "Standard Test Method for Linear-Elastic Plane Strain Fracture Toughness K_{IC} of Metallic Materials," American Society for Testing and Materials (ASTM) International.

[21]ASTM Designation E 1820-2001, "Standard Test Method for Measurement of Fracture Toughness," American Society for Testing and Materials (ASTM) International.

[22] ASTM Designation: E 23-05, "Standard Test Methods for Notched Bar Impact Testing of Metallic Materials", American Society for Testing and Materials,

[23] Fast Track 8800, "Bluehill 2 Software," Instron Material Testing Systems.

[24] Instron Testing Systems, "Specifications – Model 8862," Dynamic and Fatigue Test Systems – High Precision Electric Actuator Systems.

[25] Subhra Bandyopadhyay, "Residual Stress Characterization and Defects Analyses by Microscopy," M.S. Thesis, Department of Mechanical Engineering, University of Nevada, Las Vegas, Fall 2005.

[26] Hirsch P., Howie A., Nicholson R., Pashley D.W., Whelan M.J., "Electron Microscopy of Thin Crystals," Malabar, Krieger Publishing Company, 1977.

[27] Loretto M.H., "Electron Beam Analysis of Materials," London, Chapman and Hall, 1994.

[28] J. Pesicka, R. Kuzel, A. Dronhofer and G. Eggeler, "The Evolution of Dislocation Density During Heat Treatment and Creep of Tempered Martensitic Ferritic Steels," Acta Materialia, vol. 51, issue 16, 2003, pp. 4847-4862.

[29] R.F. Egerton, "Electron Energy Loss Spectroscopy in Electron Microscope," Plenum Press, 1986, pp. 291-352.

[30] Mean Free Path Calculation, "The Inelastic Mean Free Path of Electrons in Solids," Surface and Interface Science.

[31] R. Kishore, R.N. Singh, T.K. Sinha and B.P. Kashyap, "Effect of Dynamic Strain Ageing on the Tensile Properties of a modified 9Cr-1Mo Steel," Journal of Materials Science, vol. 32, 1997, pp. 437-442.

[32] Y. Ilino and M. Nakahara, "Effect of High Temperature Plastic Strain with Dynamic Strain Ageing on Sensitization of Type 304 Stainless Steel," Journal of Materials Science, vol. 26, no. 21, 1991, pp. 5904-5910.

[33] K.G. Samuel, S.L. Mannan and P. Rodriguez, "Serrated Yielding in AISI 316 Stainless Steel," Acta Metallurgica, vol. 36, no. 8, 1988, pp. 2323-2327.

[34] S.L. Mannan, K.G. Samuel and P. Rodriguez, "Dynamic Strain Ageing in Type 316 Stainless Steel," Trans. Indian Inst. Met., vol. 36, no. 4, 1983, pp. 313-320.

[35] Vani Shankar, M. Valsan, K. Bhanu Shanakara Rao and S.L. Mannan, "Effects of Temperature and Strain Rate on Tensile Properties and Activation Energy for Dynamic Strain Aging in Alloy 625," Metallurgical and Materials Transactions A, vol. 35A, no. 9, 2004, pp. 3129-3139.

[36] Soon H. Hong, Hee Y. Kim, Jin. S. Jang and Il H. Kuk, "Dynamic Strain Aging Behavior of Inconel 600 Alloy," Superalloys, 1996, The Minerals, Metals and Materials Society.

[37] A. Girones, L. Llanes, M. Anglada and A. Mateo, "Dynamic Strain Aging Effects on Super duplex Stainless Steels at Intermediated Temperatures," Materials Science and Engineering A, 2004, pp. 322-328.

[38] Kaiping Peng, Kuangwu Qian and Wenzhe Chen, "Effect of Dynamic Strain Aging on High Temperature Properties of Austenitic Stainless Steel," Materials Science and Engineering A, 2004, pp. 372-377.

[39] L.H. de Almeida and P.R.O. Emygdio, "Activation Energy Calculation and Dynamic Strain Aging in Austenitic Stainless Steel," Scripta Metallurgica et Materialia, vol. 31, no. 5, 1994, pp. 505-510.

[40] P. Rodriguez, "Serrated Plastic Flow," Bulletin of Materials Science, vol. 6, 1984, pp. 653-664.

[41] V. Raghavan, "Mechanical Properties," Physical Metallurgy, Chapter 5, pp. 141-146.

[42] Key To Steel, "True Stress – True Strain Curve," Article, The Steel Database.

[43] K.G. Samuel, "Limitations of Hollomon and Ludwigson Stress-Strain Relations in Assessing the Strain Hardening Parameters," Journal of Physics D, vol. 39, 2006, pp. 203-212.

[44] Hollomon H., Trans. AIME, vol. 162, 1945, pg. 268.

[45] George E. Dieter, "Mechanical Metallurgy – SI Metric Edition", pp. 476-478.

[46] Metallography and Microstructures, "Microetchants for Wrought Heat-resistant Alloys," ASM Handbook, vol. 9

[47] V. Raghavan, "Mechanical Properties," Chapter 5, Physical Metallurgy, pp. 164-165

[48] Longzhou Ma, "Comparison of Different Sample Preparation Techniques in TEM Observation of Microstructure of Inconel Alloy 783 Subjected to Prolonged Isothermal Exposure," Micron, vol. 30, 2004, pp. 273-279.

[49] Paul E. Fischione, "Materials Specimen Preparation for Transmission Electron Microscopy," E.A.Fischione Instruments, Inc. Export, PA, USA.

[50] Metallography and Microstructures, ASM Handbook, vol. 9, pg. 308, table 5.

[51] Kozue Yabusaki and Hirokazu Sasaki, "Specimen Preparation Technique for a Microstructure Analysis Using the Focused Ion Beam Process," Furukawa Review, no. 22, 2002.

[52] X. Zia, Y. Dai, "Micro-hardness Measurement and Microstructure Characterization of T91 Weld Metal Irradiated in SINQ Target-3", J. Nuc. Mat., Vol. 343, pp. 212-218, 2005

[53] Addressing the Website http://en.wikipedia.org/wiki/Fracture_toughness

VITA

Graduate College
University of Nevada, Las Vegas

Pankaj Kumar

Local Address:
1173 Maryland Circle, Apt # 3
Las Vegas, NV 89119

Degrees:

Master of Technology in Materials and Metallurgical Engineering, 2004
Indian Institute of Technology (IIT) Kanpur
Kanpur, India

Bachelor of Technology in Metallurgy and Materials Engineering, 2002
National Institute of Foundry and Forge Technology
Ranchi, India

Special Honors and Awards:

- Awarded Membership by the Honor Society of Phi Kappa Phi (ΦκΦ)
- Awarded GREAT (Graduate Research Training) Assistantship by the Graduate College of UNLV.

Publications:

- The Role of Silicon Content on Environmental Degradations of T91 Steels, Journal of Materials Engineering and Performance, paper accepted.
- Defects Characterization of Welded Specimens by Transmission Electron Microscopy, Materials Science and Engineering A, Elsevier Science, Vol. 464, August 2007, pp. 274-280
- Temperature and Silicon Content Effects on Tensile Deformation of T91 Grade Steel, SAMPE Fall meeting, Dallas, TX, November 2006
- The Role of Silicon Content on Tensile and Corrosion Properties of T91 Grade Steels, MS & T Fall meeting, Cincinnati, OH, October 2006
- Tensile Properties of T91 Grade Steel as a Function of Silicon Content, AMPT 2006, Las Vegas, July 2006
- Metallurgical and Corrosion Studies of Modified T91 Grade Steel, Materials Research Symposium Proceedings, v 929, p 149-154, 2006
- Metallurgical and Corrosion Characterization of T91 Grade Steel vs. Silicon Content, 2006 ANS Student Conference, RPI, NY, April 2006
- Relationship of Residual Stress to Dislocation Density in Cold-Worked Martensitic Alloy, Materials Science and Engineering A, Elsevier Science, Vol. 416, January 2006, pp. 134-138

- Microscopic Characterization of Discontinuous Precipitation in a Nickel Aluminide Intermetallic Material, AIChE Annual Meeting, Conference Proceedings, pp. 7958-7965October 2005
- Effect of Silicon Content on Modified T91 Grade Steel for Nuclear Application, ASM Heat Treat, Pittsburgh, PA, September 2005

Dissertation Title: "Effects of Temperature, Strain Rate and Si Content on Dynamic Strain Ageing of Modified 9Cr-1Mo Steel"

Dissertation Examination Committee:

Chairperson, Dr. Ajit K. Roy, Ph. D.
Committee Member, Dr. Anthony E. Hechanova, Ph.D.
Committee Member, Dr. Daniel Cook, Ph. D.
Committee Member, Dr. Brendan O'Toole, Ph. D.
Graduate Faculty Representative, Dr. Edward S. Neumann, Ph.D.